Tailoring the Electronic and Optical Properties
of Molecular Thin Films
by Reducing and Oxidising Agents

von der Fakultät für Naturwissenschaften der Technischen Universität Chemnitz

genehmigte Dissertation zur Erlangung des akademischen Grades

doctor rerum naturalium

(Dr. rer. nat.)

vorgelegt von M. Sc. Francisc Haidu

geboren am 1. Jan. 1986 in Baia Mare

eingereicht am 19. Feb. 2014

Gutachter: Prof. Dr. Dr. h. c. Dietrich R. T. Zahn

               Hon.-Prof. Dr. Martin Knupfer

Tag der Verteidigung: 19. Dez. 2014

Bibliografische Beschreibung

M. Sc. Francisc Haidu

Tailoring the Electronic and Optical Properties of Molecular Thin Films by Reducing and Oxidising Agents

Technische Universität Chemnitz

Dissertation (in englischer Sprache), 2014

Heutzutage wächst die Nachfrage nach neuartigen Geräten, die teilweise (hybrid) oder völlig aus organischen halbleitenden Materialien hergestellt sind. Der Grund dafür sind die geringen Herstellungskosten sowie die hohe Flexibilität im Moleküldesign und damit einstellbare optische, elektronische und Spintronik-Eigenschaften. Bisher sind mit großem Erfolg organische Leuchtdioden (OLED), organische Solarzellen und gedruckte organische Elektronik-Bauelemente hergestellt worden. Auf Grund ihrer langen Spin-Lebensdauer sind Moleküle auch für Spintronik-Anwendungen sehr geeignet.

In dieser Arbeit wurden die elektronischen und optischen Eigenschaften von vier ausgewählten Molekülen analysiert. Davon wurden Kupfer- und Mangan-Phthalocyanin (CuPc und MnPc) für die Untersuchung der Anordnung des Energieniveaus an der Metall-Organischen Halbleitern (M-O) Grenzfläche verwendet. Außerdem werden die andere zwei Moleküle tris(8-hydroxy-quinolinato) Aluminium(III) (Alq_3) und N,N'-diphenyl-N,N'-bis(1-naphthyl)-1,1'-biphenyl-4,4'-diamine (α-NPD) häufig in OLED-Strukturen als Elektron- beziehungsweise Loch-Leiter verwendet. Die Proben sind mittels organischer Molekularstrahl-Abscheidung (OMBD) auf Co (oder Au) Folien beziehungsweise auf einseitig poliertem Si(111) Einkristall hergestellt worden.

Im ersten Teil der Arbeit wurde die Entwicklung der Grenzfläche zwischen CuPc und Co (oder Au) Substrat mittels Valenzband- und Inverser Photoelektronenspektroskopie (VB-PES und IPES) analysiert und herausgefunden, dass ein „Öffnung" der Bandlücke mit dem Wachstum der Molekularschicht erfolgt. Ähnliches findet bei die MnPc/Co-Grenzfläche statt. Diese Erkenntnisse sind sehr wichtig für die Entwicklung von zukünftigen leistungsfähigen Spintronik Geräten.

Der zweite Teil fokussiert auf die Änderungen der elektronischen Eigenschaften von MnPc und Alq_3 während der Oxidation (O_2-Aussetzung) beziehungsweise Reduktion (Kalium-Abscheidung). Abgesehen von den VB-PES und IPES Messungen, bieten die Röntgenphotoelektronenspektroskopie (XPS) und die Röntgen-Nahkante-Absorptions-Spektroskopie (NEXAFS) wichtige Informationen w. z. B. die Menge von K in der Molekülschicht und den Spin-Zustand im undotierten und im dotierten MnPc.

Der dritte Teil beschäftigt sich mit den optischen Eigenschaften von MnPc, Alq_3 und α-NPD als Reinmaterialien sowie mit K-dotierten Molekülen, *in situ* verfolgt mittels spektroskopischer Ellipsometrie (SE). Vom SE-Spektrum wurde der Imaginärteil der dielektrischen Funktion abgeleitet. Während α-NPD fast keine Änderung im Absorptionsspektrum nach der Dotierung zeigt, zeigt Alq_3 dagegen ein Wandel zu einer dotierten Phase mit kleine Änderungen im Spektrum. Dabei hat MnPc drei stabile dotierte Phasen mit großen spektralen Änderungen. Außerdem zeigt die Oxidation von MnPc umgekehrt Eigenschaften zur dotierten Phase. Alle diese Messungen sind einzigartig und sehr wichtig für die Entwicklung von OLED-Geräten.

Schlagwörter

Organische Moleküle, Organische Molekularstrahl-Abscheidung (OMBD), Elektronische und optische Eigenschaften, Grenzfläche, Kalium-Dotierung, Oxidierung, Valenzband-Photoelektronenspektroskopie (VB-PES), Inverse Photoelektronenspektroskopie (IPES), Röntgenphotoelektronenspektroskopie (XPS), Röntgen-Nahkanten-Absorptions-Spektroskopie (NEXAFS), *in situ* spektroskopische Ellipsometrie.

Table of Contents

List of Abbreviations

α-NPD	N,N'-diphenyl-N,N'-bis(1-naphthyl)-1,1'-biphenyl-4,4'-diamine
AFM	Atomic Force Microscopy
Alq_3	tris(8-hydroxy-quinolinato) aluminium(III)
Ar	argon
Au	gold
BE	binding energy
BESSY II	Berliner Elektronenspeicherring Gesellschaft für Synchrotronstrahlung GmbH
BR	branching ratio
C	carbon
CL-PES	Core Level Photoemission Spectroscopy
Co	cobalt
CoPc	cobalt phthalocyanine
CuPc	copper phthalocyanine
DFT	density functional theory
DOS	density of states
EA	electron affinity
EELS	Electron Energy Loss Spectroscopy
F_4-TCNQ	tetrafluoro-tetracyanoquinodimethane
FePc	iron phthalocyanine
FWHM	full width at half maximum
GM	Geiger-Müller
H-F INDO	Hartree-Fock intermediate neglect of differential overlap
H-Si	hydrogen passivated silicon
H_2Pc	metal free phthalocyanine
HOMO	highest occupied molecular orbital
IE	ionisation energy
IPES	Inverse Photoemission Spectroscopy
K	potassium
LUMO	lowest unoccupied molecular orbital
M-O	metal-organic semiconductor
MFP	mean free path

MnPc	manganese phthalocyanine
Mo(tfd)$_3$	Molybdenum tris-[1,2-bis(trifluoromethyl)ethane-1,2-dithiolene]
MPc	metal phthalocyanine
MR	magnetoresistance
MSE	mean square error
N	nitrogen
NEXAFS	Near Edge X-ray Absorption Fine Structure
O	oxygen
OLED	organic light emission diode
OMAR	organic magnetoresistance
OMBD	organic molecular beam deposition
Pc	phthalocyanine
PES	Photoemission Spectroscopy
PTCDA	3,4,9,10-perylene-tetracarboxylic dianhydride
QCM	quartz crystal microbalance
RMS	root mean square
I-O	inorganic semiconductor-organic semiconductor
SE	Spectroscopic Ellipsometry
Si	silicon
SOMO	singly occupied highest molecular orbital
TD-DFT	time dependent density functional theory
TEY	total electron yield
TMPc	transition metal phthalocyanine
UHV	ultra-high vacuum
UPS	Ultraviolet Photoemission Spectroscopy
UV	ultraviolet
VB	valence band
VB-PES	Valence Band Photoemission Spectroscopy
VL	vacuum level
XAS	X-ray Absorption Spectroscopy
XPS	X-ray Photoemission Spectroscopy
ZnPc	zinc phthalocyanine

1. Introduction

The emerging field of *organic spintronics* combines the potentials of spintronics [Zuti04] and organic electronics [Forr04]. Besides low production costs, high flexibility, and never ending opportunities in molecular design, organic molecules have long spin-coherence lifetimes which makes them promising candidates for future spintronic applications [Barr10, Shen10B, Kato12, Krul13].

This work was carried out within the *Towards Molecular Spintronics* (TMS) research project, which aims the integration of spintronic functionality of single molecules into nanostructured devices. The fundamental properties of the molecules were investigated starting at the interface with the magnetic metallic contacts (*e.g.* cobalt) as the energy level alignment is critical for efficient spin injection into organic materials [Caru05, Barr10, Lach12, Schm11, Stei11, Aris09A, Cinc09]. Besides the electronic and optical properties, the spin state is highly tuneable by adjusting peripheral ligands or by exchanging components of the molecular body, *e.g.* the central metal ion of phthalocyanine (Pc) molecules [Grob10].

First, the attention was focused at the metal-organic semiconductor (M-O) interface, which plays a major role for the newly growing field of organic spintronics. Copper phthalocyanine (CuPc) and manganese phthalocyanine (MnPc) were employed as model organic layers. The interface formation between the molecular thin films and the Co and Au substrates was studied by combined Valence Band Photoemission Spectroscopy (VB-PES) and Inverse Photoemission Spectroscopy (IPES) measurements. By varying the thickness of the organic thin film the evolution of the energy level alignment was determined. Due to the influence of image charge potential on the transport band gap [Knup05, Flor09, Tsip02] the parallel band evolution of the occupied and unoccupied electronic states does not hold and the use of both techniques (VB-PES and IPES) is a necessity. Moreover, excitonic effects [Zahn06] play a major role in organic semiconductors with the main consequence of reducing the optical band gap as much as 1 eV [Hill00A].

The second part of the study deals with the changes of the molecular electronic properties upon oxidation (O_2 exposure) and reduction (potassium intercalation) for MnPc and tris(8-hydroxy-quinolinato) aluminium(III) (Alq_3) thin films. It is known for a long time that MnPc molecules coordinate molecular oxygen [Elvi59] and other small gas molecules [Mori97]. Thus, MnPc molecules were implemented in devices as gas

sensors [vFaa03]. Recently MnPc was considered as a very good candidate for spintronic devices due to its intermediate-spin S = 3/2 ground state [Barr70, Tagu06] and nearly perfect spin filtering properties [Shen10A]. Moreover, by doping with alkali metals a high-spin state of S = 5/2 could be obtained [Tagu06] and the electrical conductivity was highly increased [Crac05, Crac06]. Another recent discovery was the $MnPc^{\delta+}$ / $F_{16}CoPc^{\delta-}$ charge transfer dimer [Lind12, Lind13] with a total spin state of S = 2. In this study MnPc was investigated by VB-PES and IPES, Core Level Photoemission Spectroscopy (CL-PES), as well as Near Edge X-ray Absorption Fine Structure (NEXAFS) spectroscopy.

The second molecule studied in this part by VB-PES and IPES was Alq_3 which is considered as well a very good candidate for spintronics devices since it reveals huge magnetoresistance (MR) at low temperatures (300 % at 2 K) [Barr10] and can sustain a small percent of it even at room temperature [Dedi08, Sant07]. The organic MR (also referred to as OMAR) can be positive or negative and is highly dependent on temperature, current, and magnetic field [Bloo07]. Upon doping the MR at room temperature can be significantly increased [Prig06].

It should be noted that Photoemission Spectroscopy studies on alkali metal intercalated molecules are fairly common: mostly Pcs such as H_2Pc [Nils12], CuPc [Schw02, Gao03B, Ding08, Molo08A, Ding10], FePc [Aris10, Ange11], CoPc [Aris11], ZnPc [Schw03, Giov07], but also Alq_3 [Joha99, Fung04, Ding05, Kim12] and N,N'-diphenyl-N,N'-bis(1-naphthyl)-1,1'-biphenyl-4,4'-diamine (α-NPD) [Schw03] were considered.

In the third part of the work the optical properties of MnPc, Alq_3, and α-NPD in their pristine and K intercalated phases were monitored by *in situ* Spectroscopic Ellipsometry (SE). The study of MnPc was complemented by the impact of oxidation on its absorption spectrum. Although information on the changes in the absorption spectrum of specific molecules upon doping or oxidation is highly important for the performance of opto-electronic devices, there is few literature in this direction. One of the studies was performed on K intercalated 3,4,9,10-perylene-tetracarboxylic dianhydride (PTCDA) by the so called differential reflectance spectroscopy [Dien10]. Alq_3 and α-NPD are most commonly utilised electron- and hole-transporting materials, respectively, in organic light emission diode (OLED) devices [Tang87, Feng01, Tagu10]. SE measurements on their pristine phase were previously performed [Himc05], however the doping process was not yet studied optically.

In summary, employing complementary techniques, the electronic and optical properties of four different molecules were investigated: CuPc, MnPc, Alq$_3$, and α-NPD. The work is divided into four chapters the first one presenting the introduction. The second chapter is the experimental part of the work and contains information about the molecules and the employed experimental techniques together with theoretical considerations for each. Moreover, the sample preparation, measurement conditions, and data interpretation are presented in detail. The third chapter is the more substantial part of the work and contains all the results and their detailed interpretation. It is divided in four sections each presenting one of the studied molecules. Finally, the fourth chapter summarises all the findings and their significance.

2. Experimental

This chapter is devoted to the experimental techniques utilised in the study. For each measurement method the physical phenomena is introduced together with the theory beneath it. The equipment is presented with all the relevant parameters used for the experiment. Some selected examples for data evaluation are specified. The first subchapter introduces the molecules and their relevant properties for the experiments. A more detailed description together with a comprehensive literature study will be given in chapter 3.

2.1. Investigated Molecules

Four organic molecules were investigated in this study: CuPc, MnPc, Alq$_3$ and α-NPD. Their molecular structures are presented in Figure 2.1.1. CuPc and MnPc are planar molecules and tend to form anisotropic films. Alq$_3$ and α-NPD on the other hand produce isotropic films due to their distorted structure.

CuPc with a dye content of 99 % was purchased from Sigma-Aldrich® and used without any supplementary purification. MnPc purchased from STREM Chemicals, Inc., had 97 % specified purity and was sublimed as received. Alq$_3$ and α-NPD were bought from Sensient Imaging Technologies GmbH and were extra purified by sublimation.

The molecules were deposited by organic molecular beam deposition (OMBD) from Knudsen cells, as presented for each setups beneath. The sublimation temperature varies for each molecule. CuPc sublimes with a rate of 0.2 nm/min at around (315 ± 10) °C. However, MnPc starts to sublime at 340 °C and for a higher rate (0.2 nm/min) the temperature has to be increased up to 380 °C. Alq$_3$ and α-NPD sublime at precise and lower temperatures of (230 ± 5) °C and (220 ± 5) °C, respectively. The temperatures were measured with a *type S* thermocouple mounted in contact with the sublimation crucible.
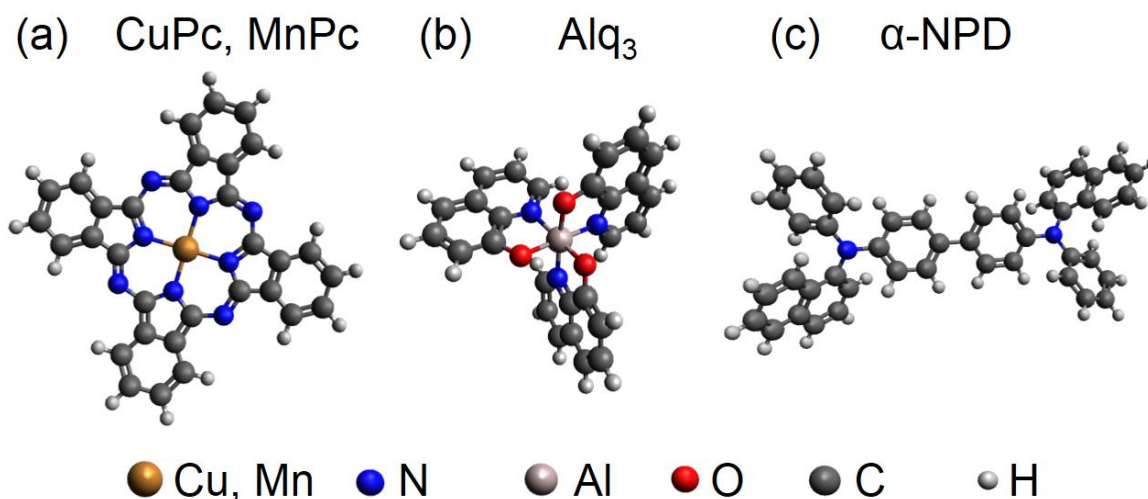
Figure 2.1.1. Molecular structures of CuPc and MnPc (depending on the central metal ion) (a), Alq₃ (b), and α-NPD (c). The constituent atoms are listed below the molecules according to the colour codes. The molecules were plotted using the open-source molecular builder and visualisation tool Avogadro Version 1.0.3 [AVOG]. The geometry was calculated using the molecular mechanics optimisation (Universal Force Field) [Rapp92].

2.2. Photoemission Spectroscopy Methods

This subchapter presents the techniques used to study the electronic properties of the molecules. The techniques are all related to the photoelectric effect. Before the individual description of each technique in separate sections an overview on the relations between them and some theoretical particularities are presented.

The phenomenon of photoemission was discovered by Herz in 1887 [Bonz95] and gave rise up to this days to many experimental techniques for material characterisation. The names Photoelectron or Photoemission Spectroscopy (both PES) are used whether the emitted particles or the processes leading to the emission are investigated, respectively [Hüfn03]. In principle, the technique consists of a light source which impinges photons on the sample surface and the emitted photoelectrons are analysed with respect to their kinetic energy (E_{kin}) and their momentum. The formula between E_{kin} and the binding energy (E_B) is:

$$E_{kin} = h\nu - \Phi - |E_B|, \qquad (1)$$

where $h\nu = \hbar\omega$ is the energy of light and Φ represents the work function of the sample.

Function of the excitation light energy the techniques are called Ultraviolet Photoemission Spectroscopy (UPS) or X-ray Photoemission Spectroscopy (XPS) for ultraviolet (UV) or X-ray, respectively. In principle, UPS is used to scan the occupied density of states (DOS) of the valence band (VB) and XPS to determine the core level (CL) positions (see *e.g.* Figure 2.2.1(a) and (c)). Further in this work the UPS will be also referred to as Valence Band Photoemission Spectroscopy (VB-PES) whereas the XPS will be also called Core Level Photoemission Spectroscopy (CL-PES).

Furthermore, to study the unoccupied DOS a complementary technique to VB-PES is used, *i.e.* Inverse Photoemission Spectroscopy (IPES). IPES consist in a beam of collimated electrons entering the system and afterwards they decay, either radiatively or non-radiatively to states at lower energy [Smit88] (Figure 2.2.1(b)). The radiative decay can be detected by a photon detector. Therefore IPES samples all the unoccupied DOS [Fugg92, Hüfn03]. There are two ways for scanning: fixed electron energy and a tuneable photo detector or having a photo detector with a fixed photon energy and sweeping the energy of the excited electrons (also referred to as Bremsstrahlung Isochromat Spectroscopy [Smit88]). Most of the IPES experiments are performed in the second configuration, as were also the ones performed within this work.

X-ray Absorption Spectroscopy (XAS) measures the absorption of radiation which induces a transition of an electron from a core level into an unoccupied valence state. Therefore the spectra is related to the unoccupied DOS. However, XAS provides information only on site- and symmetry-selected DOS [Fugg92]. In this way it is a complementary technique to IPES. As schematically represented in Figure 2.2.1(d) the decay of the produced core hole can result in fluorescence or excite an Auger electron. The measurements in this study were performed by detecting the total electron yield (TEY) of the absorption process. This will be presented in more detail in section 2.2.4.

It should be noted, that it is an exceptional opportunity to perform both NEXAFS and IPES experiments to study the unoccupied electronic states of molecules. First, the measurement time at synchrotron radiation facilities is limited. Second, although IPES does not require measurement time application, it is not a common measurement
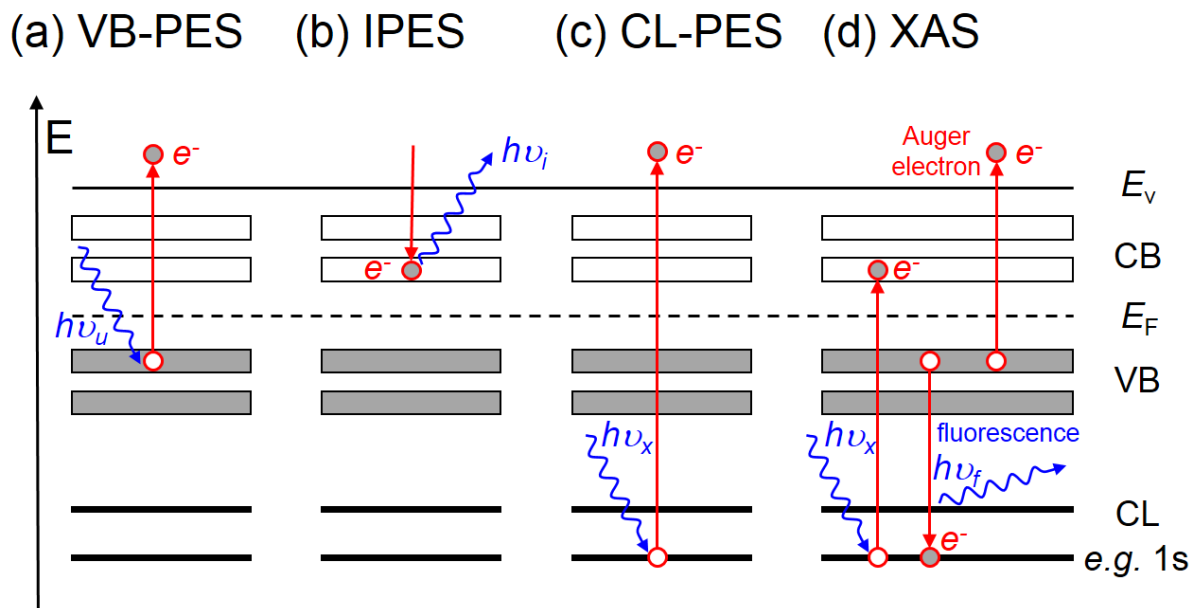
Figure 2.2.1. Schematic representation of the physical processes which take place in the following spectroscopic techniques: (a) VB-PES, (b) IPES, (c) CL-PES, and (d) XAS.

method. There are only few groups in the world, besides the semiconductor physics group in Chemnitz, which successfully implemented the technique. With a great interest towards organic materials, the groups of A. Kahn (Princeton University) and H. Yoshida (Kyoto University) provide good competition in the field of IPES.

2.2.1. Theoretical Considerations

PES, IPES, and XAS are described by complicated many body theories [see *e.g.* Hüfn03, Fugg92, Smit88, Stöh96, and literatures within]. These take into account the transition probability from an initial state i to a final state f with the wave functions Ψ_i and Ψ_f, respectively. This section provides just very short introduction on the theoretical part.

With the assumption of a small perturbation Δ *"Fermi's Golden Rule"* yields the transition probability per unit time P_{if} as:

$$P_{if} \propto \frac{2\pi}{\hbar} \left| \langle \Psi_f | \Delta | \Psi_i \rangle \right|^2 \delta \left(E_f - E_i - \hbar\omega \right). \qquad (2)$$

The perturbation Hamiltonian is given in the most general form by the formula:

$$\Delta = \frac{e}{2mc}(\boldsymbol{A} \cdot \boldsymbol{p} + \boldsymbol{p} \cdot \boldsymbol{A}) - e\Gamma + \frac{e^2}{2mc^2}\boldsymbol{A} \cdot \boldsymbol{A}, \tag{3}$$

where $\boldsymbol{A}$ and Γ are the vector and scalar potentials of the radiation field and $\boldsymbol{p} = i\hbar\boldsymbol{\nabla}$ represents the momentum operator. Due to the commutation relation the following equation can be written: $\boldsymbol{A} \cdot \boldsymbol{p} + \boldsymbol{p} \cdot \boldsymbol{A} = 2\boldsymbol{A} \cdot \boldsymbol{p} + i\hbar(\boldsymbol{\nabla} \cdot \boldsymbol{A})$. Furthermore, the $\boldsymbol{A} \cdot \boldsymbol{A}$ term can be neglected (represents the two photon processes), and it can be assumed that $\boldsymbol{\nabla} \cdot \boldsymbol{A} = 0$ (because of translational invariance in the solid) as well as $\Gamma = 0$ (Coulomb gauge). Finally, the remaining interaction Hamiltonian results [Hüfn03]:

$$\Delta = \frac{e}{mc}\boldsymbol{A} \cdot \boldsymbol{p}. \tag{4}$$

For UV light the wavelength of light is much larger than the distance between the atoms and therefore $\boldsymbol{A} = \boldsymbol{A_0}$ can be considered as constant (dipole approximation). Thus, the matrix elements of Δ are constants and together with the assumption that also the DOS are constant at fixed photon energy the equation (2) can be rewritten as:

$$\begin{aligned} I^{int}(E, \hbar\omega, \boldsymbol{k}) &\propto \frac{2\pi e^2}{\hbar m^2 c^2} \left|\langle \Psi_f | \boldsymbol{A_0} \cdot \boldsymbol{p} | \Psi_i \rangle\right|^2 \sum_{fi} \delta\big(E_f(\boldsymbol{k}) - E_i(\boldsymbol{k}) - \hbar\omega\big) \delta\big(E - E_f(\boldsymbol{k})\big) \\ &\propto \sum_{fi} M_{fi}\, f(E_i)\delta\big(E_f(\boldsymbol{k}) - E_i(\boldsymbol{k}) - \hbar\omega\big)\delta\big(E - E_f(\boldsymbol{k})\big) \end{aligned}, \tag{5}$$

where M_{fi} represent the matrix elements and $f(E_i)$ is the Fermi distribution function.

Equation (5) represents the internal electron current density directed towards the surface having an energy E and a wavevector $\boldsymbol{k}$ [Lüth10]. It represents the first step in the *three-step model*. Although less accurate than the *one-step model* (for more information see reference [Hüfn03]), it is simpler and more instructive.

The *three-step model* stepwise explains the following:
(i) Photo excitation of an electron in the sample material → the matrix element in equation (5) is evaluated between two Bloch states in the solid.
(ii) Propagation of the excited electron to the surface → damping of the electron wave described by a complex wave vector.
(iii) Emission of the electron into the vacuum → conservation of $\boldsymbol{k}_{||}$.

On their way to the surface (step (ii)) most of the electrons undergo inelastic scattering processes. Their kinetic energy is reduced. These electrons contribute to the *secondary electrons background* which will be mentioned again in section 2.2.2.

The propagation can be described by the transport probability proportional to the mean free path:

$$D(E, \boldsymbol{k}) \propto \lambda(E, \boldsymbol{k}). \tag{6}$$

Finally, in step (iii) the photoelectron has to be transmitted through the surface which requires the conservation of the parallel component of the wave vector:

$$\boldsymbol{k}_{||}^{ex} = \boldsymbol{k}_{||} + \boldsymbol{G}_{||}. \tag{7}$$

From the conservation of energy it can be deduced:

$$E_{kin} = \frac{\hbar^2}{2m}\left(\left(\boldsymbol{k}_\perp^{ex}\right)^2 + \left(\boldsymbol{k}_{||}^{ex}\right)^2\right) = E_f - E_{vac}, \tag{8}$$

which can be directly related to equation (1) together with the relations: $\hbar\omega = E_f - E_i$, $\Phi = E_{vac} - E_F$, and $E_B = E_F - E_i$.

From equation (7) the transmission rate can be described by:

$$T(E, \boldsymbol{k})\delta(\boldsymbol{k}_{||} + \boldsymbol{G}_{||} - \boldsymbol{k}_{||}^{ex}). \tag{9}$$

Finally, the emission current according to this model can be written together with the equations (5), (6), and (9) [Lüth10]:

$$I^{ex}(E, \hbar\omega, \boldsymbol{k}_{||}^{ex}) = I^{int}(E, \hbar\omega, \boldsymbol{k})D(E, \boldsymbol{k})T(E, \boldsymbol{k})\delta(\boldsymbol{k}_{||} + \boldsymbol{G}_{||} - \boldsymbol{k}_{||}^{ex}). \tag{10}$$

Although IPES could be assessed as the time-reversed version of PES there are some differences in the theoretical background. First of all photoemission involves transition from the $n \to n-1$ electron system, whereas inverse photoemission involves the transition $n \to n+1$ [Smit88]. Still, the Hamiltonian associated to the electromagnetic wave is described as in photoemission by equation (3). Taking into account equation (5) the cross sections for the photoemission and inverse photoemission processes are given by:

$$\begin{aligned}
\left(\frac{d\sigma}{d\Omega}\right)_{PES} &= \frac{e^2}{2\pi\hbar c}\frac{k}{m}\frac{1}{\hbar\omega}|\langle k|\boldsymbol{A_0}\cdot\boldsymbol{p}|b\rangle|^2 \\
\left(\frac{d\sigma}{d\Omega}\right)_{IPES} &= \frac{e^2}{2\pi\hbar c}\frac{\omega}{mc^2}\frac{1}{\hbar k}|\langle b|\boldsymbol{A_0}\cdot\boldsymbol{p}|k\rangle|^2
\end{aligned}^{,} \tag{11}$$

where the state $|\mathbf{k}\rangle \equiv \Psi_k(\mathbf{r})$ with no photons is the final state in PES and initial state in IPES. Whereas, the bound state $|b\rangle \equiv \Psi_b(\mathbf{r})$ plus a photon with wave vector $\mathbf{q}$ represents the initial state in PES and final state in IPES processes. Calculating the ratio of the two cross sections with the following equation results:

$$r \equiv \left(\frac{d\sigma}{d\Omega}\right)_{IPES} \left(\frac{d\sigma}{d\Omega}\right)_{PES}^{-1} = \frac{\omega^2}{c^2 k^2} = \left(\frac{\lambda_e}{\lambda_p}\right)^2, \tag{12}$$

where λ_e and λ_p are respectively the wavelength of the photo-emitted electron and the photon. This formula indicates that the cross section of inverse photoemission is much lower than for the photoemission process. The value of r is 10^{-5} in UV and around 10^{-3} in the X-ray region [Smit88].

Now, the cross section of the XAS process (σ_X) will be evaluated. It is defined by the probability of the emission of a photoelectron (equation (5)) divided by the photon flux (F_{ph}):

$$\sigma_X = \frac{I^{int}}{F_{ph}}, \qquad \text{where} \qquad F_{ph} = \frac{A_0^2 \omega}{8\pi\hbar c}. \tag{13}$$

With the expression of the energy of the final states written as $\delta(E_f)$ the expression of the cross section becomes [Stöh96]:

$$\sigma_X = \frac{4\pi^2\hbar^2}{m^2} \frac{e^2}{\hbar c} \frac{1}{\hbar\omega} |\langle \mathbf{k}|\mathbf{e} \cdot \mathbf{p}|b\rangle|^2 \delta(E_f). \tag{14}$$

The most important feature of the above equation is the angular dependence contained in the dipole matrix elements. This dipole selection rule provides a direct correlation between the polarisation of the excitation light and the symmetry of the probed environment. The molecular orbitals have strong directional character and direct correlation between the form of the orbitals and the molecular geometry. Thus, resonances associated with, *e.g.* σ^* and π^* final states are expected to exhibit different angular dependences on the incoming polarised light [Stöh96]. This dependence together with the physical information which can be gathered from it is discussed in more detail in section 2.2.4.

All the techniques presented above are very surface sensitive due to the low mean free path (MFP) of the photoelectrons in the materials. According to the *"universal"* MFP curve [Hüfn03] at low energies produced in the UV region the

information depth is less than 1 nm and increases to a maximum value of 2 nm for kinetic energies in CL-PES experiments. The penetration depth of light is many orders of magnitude higher and plays no role in the surface sensitivity.

2.2.2. VB-PES and IPES: Setup and Data Evaluation

Both VB-PES and IPES systems are attached to the same ultra-high vacuum (UHV) chamber (ARUPS10, see Figure 2.2.2(a)) with a base pressure in the low 10^{-10} mbar. To change between the experiments the sample has to be only rotated.

Although there is the possibility to perform angle resolved UPS measurements, due to the polycrystalline nature of the samples studied in this work the experiments were performed at fixed angle. The measurements were recorded using a hemispherical analyser with detection geometry of the photo-emitted electrons along the surface normal. The excitation source was a He discharge lamp. For all the experiments the He I ($hv = 21.22 \ eV$) excitation line was used. In Figure 2.2.2(b) the VB-PES and IPES setups are presented in more detail.

The inverse photoemission spectrometer is a "home built" system which operates in the isochromatic mode. It has two main components: a low energy electron gun (electron excitation source) and a Geiger-Müller (GM) tube (photon detector). The collimated beam of the electron gun is mono-energetic, the energy being spanned by changing the cathode voltage. The current density (in the range of 10^{-6} A/cm^2, focused on 1 mm^2 sample surface) is low enough not to damage the organic molecules. The GM counter is filled with an Ar (10 mbar) and Ethanol (2 mbar) gas mixture and has a MgF$_2$ entrance window. It is used as a fixed energy photon detector ($hv = 10.9 \ eV$).

The resolution of the VB-PES and IPES setup is 0.20 eV and 0.50 eV, respectively, determined from the Fermi edge of clean, Ar$^+$ sputtered Au and Co foils. The Fermi edge of the metals was used as well to calibrate both valence band and inverse photoemission spectra.

The analysis chamber is connected to the sample storage area (or "Carousel", see Figure 2.2.2(a)) where a base pressure in the low 10^{-8} mbar is maintained. All the sample transfers between the Load-Lock, OMBD chamber, and the ARUPS10 were performed through this chamber.
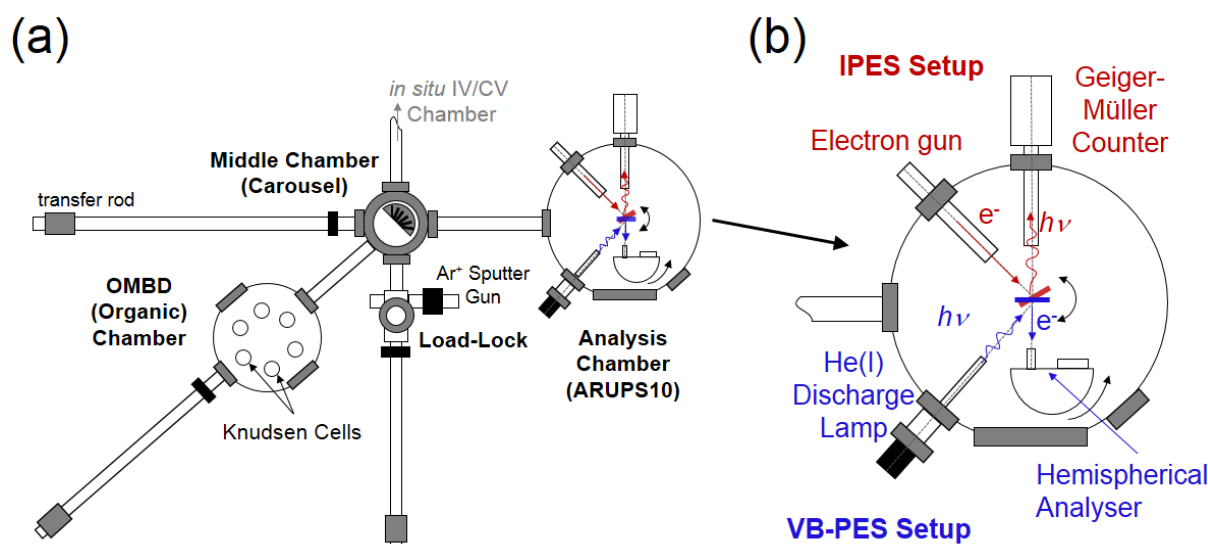
Figure 2.2.2. (a) The UHV system which contains the ARUPS10 analysis chamber, the sample preparation chamber (OMBD), the fast-entry Load-Lock, and the Middle Chamber (used for sample transfer). (b) A closer insight into the ARUPS10 system: the VB-PES (blue) and IPES (red) setups.

The Load-Lock was used to introduce samples into the system without breaking the vacuum in the other chambers. Furthermore, all the substrates for the VB-PES and IPES experiments were cleaned by Ar^+ ion bombardment in this chamber. For Ar^+ sputtering the partial pressure of the Ar gas was 5 x 10^{-6} mbar and the power of the ions was 3.5 kV. Similar cleaning procedure was implemented in the CL-PES setup as well (see section 2.2.3) where the absence of contamination was confirmed.

The fourth part of the UHV system is the preparation chamber or OMBD chamber (Figure 2.2.2(a)). The base pressure was 5 x 10^{-10} mbar and it did not exceed 1 x 10^{-8} mbar during molecular evaporation. The molecules were sublimed from Knudsen cells. The amount of evaporated organic materials was monitored by the oscillation frequency shift of a quartz crystal microbalance (QCM) which was previously calibrated. The calibration sample was composed of a thick film of CuPc deposited onto Si with native oxide. The CuPc thickness was subsequently determined by spectroscopic ellipsometry.

In the following an example of VB-PES and IPES data evaluation will be presented. Figure 2.2.3 shows the valence band and inverse photoemission spectra of a clean Co foil substrate together with an additional 20 nm thick CuPc film on top. For clarity the spectra are normalised in intensity. Additionally, regions of the valence band photoemission spectra are increased in intensity with the values written in the figure.
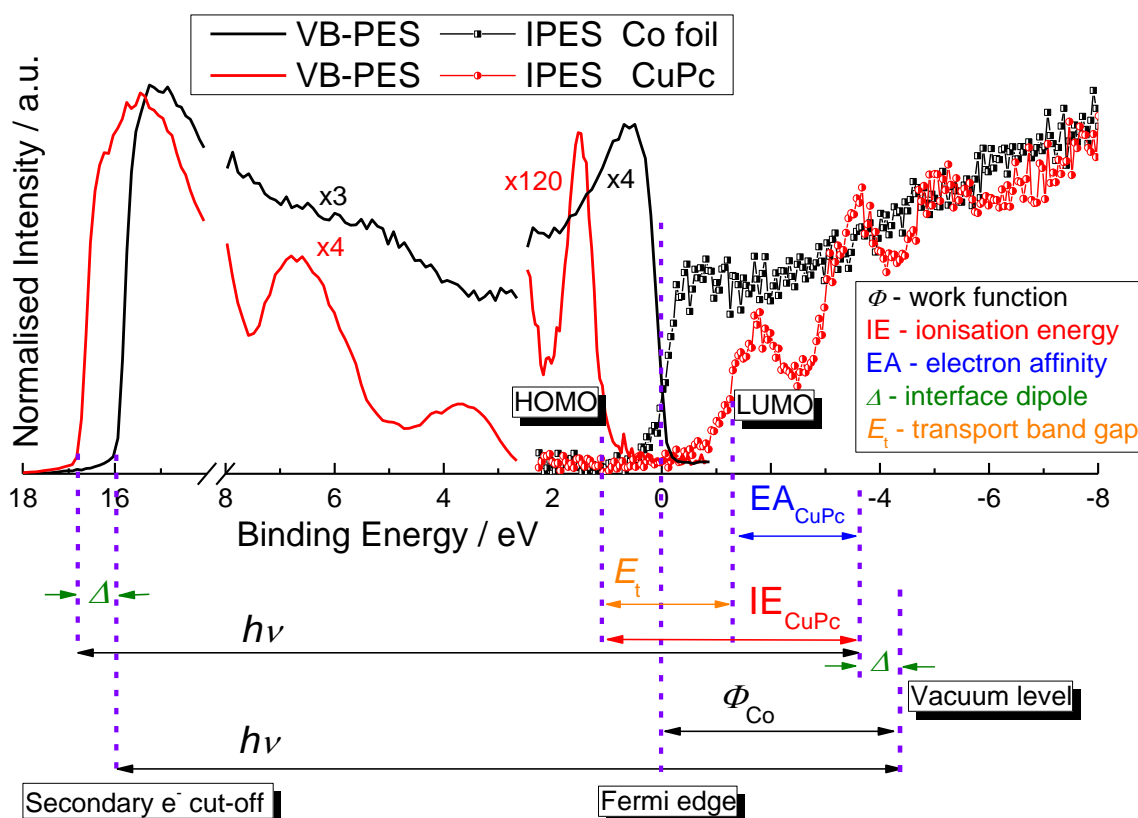
Figure 2.2.3. Example of VB-PES and IPES data analysis for a clean Co substrate (black lines and symbols) and for a CuPc(20 nm)/Co film (red lines and symbols). In specified regions the data is scaled for clarity. The physical quantities to be determined are defined by coloured vertical arrows.

For historical reasons the valence band spectra are plotted with decreasing binding energy (BE) from left to right. Following this convention the inverse photoemission spectra follows on the right hand side as well with the same trend, however with negative values. All spectra are plotted with respect to the Fermi edge ($E_F = 0$ eV). Please note that all the combined valence band and inverse photoemission spectra in this work will be presented in this fashion.

The highlighted parts of the combined valence band photoemission spectra and inverse photoemission spectra in Figure 2.2.3 are the *secondary electron cut-off*, the *vacuum level*, the *Fermi edge* (only for the Co foil), and the *HOMO* (highest occupied molecular orbital) and *LUMO* (lowest unoccupied molecular orbital) *onsets* (both only for the CuPc film). The position of the vacuum level (VL) is not directly seen in the spectra but it is determined by subtracting the energy of the excitation photons $h\nu = 21.22$ eV from the position of the secondary electron cut-off. After all the above specified spectral positions are identified the physical quantities presented in the following paragraphs can be determined.

The work function of the metal substrate (Φ_{Co}) is given by the difference between the Fermi edge position and the VL. Because the semiconducting organic materials have no Fermi edge they also have no work function. However, for further discussions the work function of the CuPc sample (Φ_{CuPc}) is defined by keeping in mind that the Fermi level remains at the same energy position as long as the upper layer (CuPc film) is in contact with the substrate and there are no charging effects. The value of Φ_{CuPc} is the energy between VL of the CuPc film and the Fermi edge of the substrate. The second quantity to be determined is the interface dipole Δ given by the difference in energy of the VL of the substrate (Co foil) and the VL of the material above (CuPc).

Further, the ionisation energy (IE) and electron affinity (EA) of the organic film are determined by subtracting the energy of the VL from the HOMO and LUMO onsets, respectively. Knowing these two quantities the last, and probably most important quantity can be determined, which is the transport band gap E_t. It is defined as the difference between the IE and the EA.

The spectra were fitted using the UNIFIT2010 [UNIF, Hess03] data analysis software. The HOMO and LUMO peaks were fitted with Gaussian line shapes and the background with a third order polynomial function [Gorg05]. For the inverse photoemission spectra the resolution of the setup has to be taken into account. Thus, a deconvolution of the peaks has to be performed according to the formula:

$$FWHM_{exp}^2 = FWHM_{setup}^2 + FWHM_{LUMO}^2, \tag{15}$$

where $FWHM_{exp}$ is the full width at half maximum of the experimental data, $FWHM_{setup} = 0.5 \text{ eV}$ is the resolution of the IPES setup and $FWHM_{LUMO}$ represents the physical broadening of the peak. The last value has to be determined to find the exact LUMO onset position.

Figure 2.2.4 exemplifies the exact method for determining the onset positions. The value of the secondary electron cut-off position is given by the intersection of a straight line through the experimental points with the energy axis (see Figure 2.2.4(a)). The HOMO and LUMO onset positions were determined from the intersection between the energy axis and tangent lines to the fitted HOMO Gaussian and deconvoluted LUMO Gaussian peaks, respectively, (see Figure 2.2.4(b)).
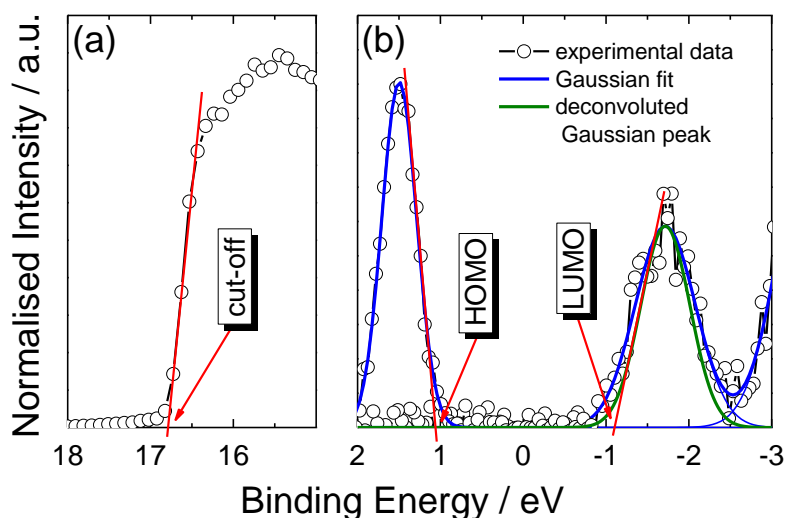
Figure 2.2.4. Example to precisely determine the cut-off position (a), and the HOMO and LUMO onset positions (b). The open symbols represent the experimental VB-PES and IPES data. The blue lines represent the fitted HOMO and LUMO peaks and the green line is the deconvoluted LUMO peak.

Schematic representations and further detailed explanations on the interface formation between organic semiconducting and inorganic semiconducting materials can be found *e.g.* in references [Zahn06, Ishi99].

2.2.3. CL-PES Setup and Measurement Conditions

CL-PES measurements were performed at the Russian-German beamline [RGBL] at the BESSY II synchrotron radiation facility, Helmholtz-Zentrum Berlin [BESS]. The experimental station (RGL end‑station) is equipped with a SPECS PHOIBOS 150 analyser with a 2D CCD detector. The energy resolution of the analyser is better than 7 meV [RGBL] and the overall energy resolution also accounting for thermal broadening is given in Table 2.1. The excitation energy of the monochromator ranges from 72 eV up to 1500 eV.

The CL-PES measurements were recorded with detection geometry of the photo-emitted electrons along the surface normal. For the acquisition of the core level (or valence band) spectra the excitation energies listed in Table 2.1 were utilised. Those excitation energy values were selected for which the atomic photo-ionisation

cross sections have large values and the secondary electrons tail does not have strong influence on the photoemission spectra.

All measurements were performed under UHV conditions with a base pressure in the low 10^{-10} mbar range. The base pressure in the preparation chambers was 5×10^{-10} mbar. The substrates were cleaned by Ar^+ ion bombardment under the same conditions as in section 2.2.2.

The energy scale of all CL-PES data was calibrated by identifying the Au 4f peak positions for each excitation energy. Correction of signal intensity was not needed as the *top-up mode* was implemented for electron injection [BESS] which provides almost constant photon flux. For an exact study of the chemical composition (atomic concentration) the transmission function of the analyser and detector has to be known. However, in this work only the K atom to C atom ratio is investigated for which the core levels are only ~10 eV apart. In such a small spectral region the transmission function is constant and has no influence on the upper mentioned peak ratio. In conclusion, only the atomic photo-ionisation cross sections were taken into account to determine the K atomic concentration as it is described in section 2.2.5.

Fitting of the CL-PES spectra was performed as well using the UNIFIT2010 [UNIF, Hess03] software. In the fitting procedure of the CL-PES data Voigt peaks and a Shirley background were implemented. The peak shapes have both Lorentzian and Gaussian contributions. The limited lifetime of the core hole state produce a Lorentz type of broadening while the measurement setup induces a Gaussian broadening. The convolution of the two profiles, the so called Voigt profile, reproduces the most adequately the experimental data [Hess07]. The Shirley model [Shir72] is a successful approximation for the inelastic background of the core level peaks.

core (or valence) levels	Cu 2p	Mn 2p	N 1s	K 2s	K 2p	C 1s	valence band
excitation energy / eV	1080	750	500	500	500	500	150
cross section / Mb[a]	0.75[b]	1.2[b]	0.45[b]	0.2[b]	1.0[b]	0.30[b]	
resolution / eV	~0.4[c]	~0.25[c]	0.23[c]	0.23[c]	0.23[c]	0.23[c]	~0.15[c]

Table 2.1. The excitation energies utilised for the acquisition of core level and valence band spectra, the respective cross sections, and the spectral resolution at the specified energies. Notes: [a] Mb (mega barn) represents a unit of area, 1 Mb = 10^{-22} m^2, data according to ref. [b] [Yeh85] and ref. [c] [Molo05].

2.2.4. NEXAFS Data Interpretation

Near Edge X-ray Absorption Fine Structure (NEXAFS) spectroscopy is an XAS technique which analyses the absorption features close to the edge of a certain electronic shell (*e.g. K edge* and *L_2 + L_3 edges* for 1s and 2p shells, respectively). A prerequisite for the technique is the possibility of varying the excitation photon energy. This can be achieved at the synchrotron facility.

NEXAFS experiments were performed at the Russian-German beamline [RGBL] on the same system presented in section 2.2.3. The TEY signal was measured in a specific photon excitation energy range as exemplified in Figure 2.2.5(a) for the C *K edge.* The photon flux was recorded using a clean gold grid placed in the beamline before the sample. Its signal was used to normalise the TEY spectrum of the sample. As the signal intensity depends on many more parameters, *i.e.* incidence angle, film thickness, surface roughness *etc.*, it has to be normalised for comparison. The illuminated area on the sample surface is function of the incidence angle of the excitation beam. Thus, the overall intensity of the spectrum changes accordingly. For very thin films the substrate signal might influence the spectra and should be excluded. The pre-edge part and the spectral tail are normalised to 0 and 1, respectively, as seen in the example of Figure 2.2.5(a). For more detail about this subject please refer to the references [Stöh96, Schö03, Watt06].

NEXAFS spectra were recorded for the CuPc and MnPc molecules as they exhibit an anisotropic (planar) geometry which can be exploited to determine molecular orientation. Please note that the discussion in this section only refers to *K shell* excitations, *i.e.* C *K edge* and N *K edge*. For these transitions the spectra can be divided into two parts (see *e.g.* Figure 2.2.5(a)): features belonging to the 1s core level $\rightarrow \pi^*$ transitions (red hatched area) and to the 1s core level $\rightarrow \sigma^*$ transitions (blue hatched area). It should be noted that the π^* and σ^* orbitals have out-of-plane respectively in-plane symmetry with regard to the molecular plane. The electric field vector $\mathbf{E}$ of the incident light interacts with the electric dipole moment. For *K shell* excitations the initial 1s state has σ symmetry while the final state has either π or σ symmetry, allowed by the dipole selection rules [Stöh96]. Thus, if $\mathbf{E}$ is perpendicular to the plane of the molecule the π^* resonances are excited while for $\mathbf{E}$ oriented parallel to the molecular plane the σ^* resonances are excited [Stöh96]. Making use
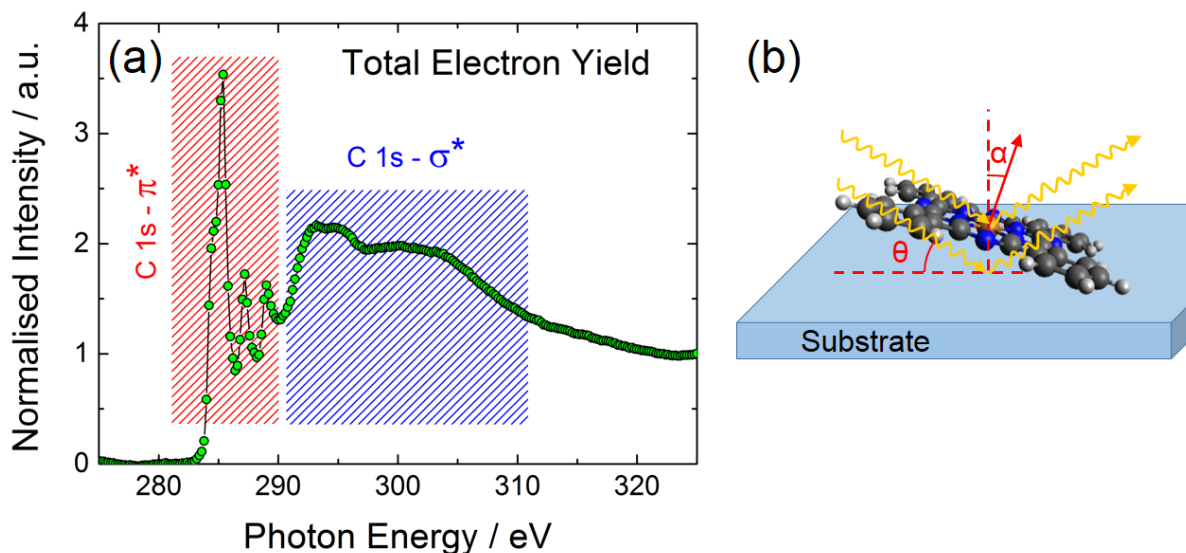
Figure 2.2.5. (a) Example of NEXAFS carbon *K edge* spectra for CuPc. The data represent the total electron yield of the absorption process. The red hatched area emphasises the C 1s $\rightarrow \pi^*$ transitions while the blue hatched area emphasises the C 1s $\rightarrow \sigma^*$ transitions region. (b) Schematic representation of a metal phthalocyanine molecule on the sample surface. The angle defined by the incident light beam and the sample surface was labelled θ. The average molecular orientation with respect to the sample surface is described by the angle α.

of the geometrical dependence of the dipole transitions on the light polarisation the following formulas can be deduced for the intensities of the two resonances [Stöh96]:

$$I_{\pi^*} \sim P\left(\cos^2\theta\cos^2\alpha + \tfrac{1}{2}\sin^2\theta\sin^2\alpha\right) + \tfrac{1-P}{2}\sin^2\alpha, \qquad \text{and} \qquad (16)$$

$$I_{\sigma^*} \sim P\left(1 - \cos^2\theta\cos^2\alpha - \tfrac{1}{2}\sin^2\theta\sin^2\alpha\right) + \tfrac{1-P}{2}(1 + \cos^2\alpha), \qquad (17)$$

where $P = 0.98$ represents the degree of polarisation for the linearly polarised light. The angles θ and α are defined in Figure 2.2.5(b). θ represents the angle between the incident light beam and the substrate plane, and α is the angle between the plane of the molecule and the substrate plane. By combining equation (16) and (17) the following formula is deduced:

$$\frac{I_{\pi^*}}{I_{\sigma^*}} = B\,\frac{P(2\cos^2\theta\cos^2\alpha + \sin^2\theta\sin^2\alpha) + (1-P)\sin^2\alpha}{P(2 - 2\cos^2\theta\cos^2\alpha - \sin^2\theta\sin^2\alpha) + (1-P)(1+\cos^2\alpha)}, \qquad (18)$$

with B a constant which depends on many parameters and has to be fitted together with the average molecular tilt angel α. Although the example in the Figure 2.2.5(a) presents the line shape of the C *K edge*, the equation (18) can be employed to

determine the average molecular orientation from the N *K edge* as well, as will be presented in section 3.1.3.

2.2.5. Sample Preparation and Investigation

The molecules presented in section 2.1 were sublimed from Knudsen cells as discussed above in detail. Pure Co (Alfa Aesar, 99.997 % Puratronic®) and Au (MaTecK, 99.995 %) foils were employed as substrates. These are unpolished and exhibit large surface roughness.

For the surface roughness determination an Agilent Technologies 5420 Atomic Force Microscope (AFM) was employed in tapping mode. The substrates were analysed before (Figure 2.2.6) and after (Figure 2.2.7) Ar$^+$ ion bombardment.

All substrates were sputtered to get rid of surfaces contaminations like oxygen and carbon. Before sputtering the topography of the Au foil exhibits many scratches in comparison with the surface of the Co foil (see *e.g.* Figure 2.2.6(a) and (b)). The root mean square (RMS) roughness of the Au and Co foils were determined to be 52.5 nm and 27.7 nm, respectively.

After sputtering both substrates present more roughness due to the invasive effect of the cleaning procedure. The RMS roughness of the Au and Co foils (AFM images in Figure 2.2.7(a) and (b)) were determined to be 95.5 nm and 75.2 nm, respectively. Both RMS values increased after sputtering and the Au substrate still has a rougher surface.

The investigated thicknesses of the molecular films ranged from 0.5 nm to 22 nm. It should be mentioned that a monolayer of CuPc is ~0.3 nm considering flat laying molecules [Würt11]. Films thicker than 20 nm yield no extra information for the thickness dependence study [Gorg05, Haid13A] and within this thickness range there are no charging effects.

Selectively, the impact of alkali metal intercalation and air exposure on the molecules was investigated. Potassium was evaporated from a dispenser (SAES Getters S.p.A, Italy) mounted close to the sample in the preparation chambers of each technique above. The amount of evaporated K was monitored through time by maintaining a constant rate. The ratio of K atoms per molecule was determined by
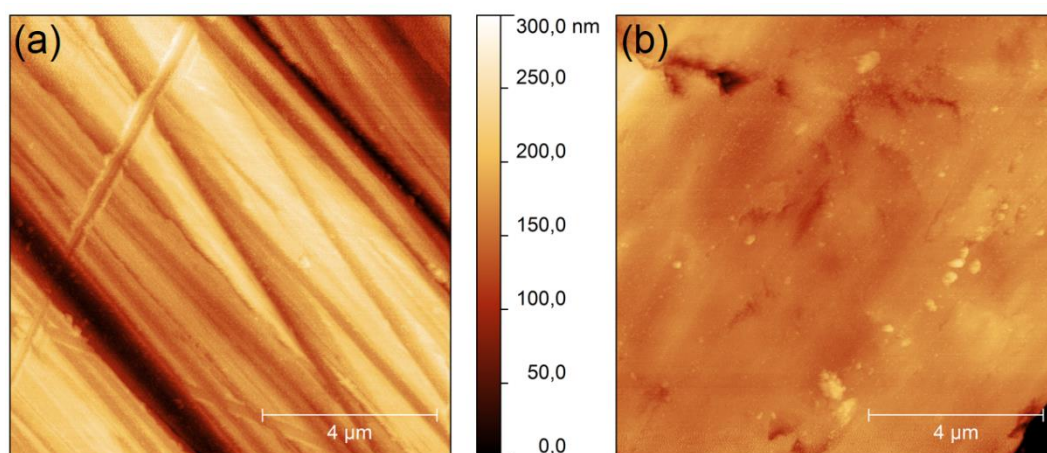
Figure 2.2.6. AFM topography images of as received Au (a) and Co (b) foils. The image sizes are 10 x 10 μm^2. The determined RMS values are 52.5 nm for the Au foil (a) and 27.7 nm for the Co foil (b).
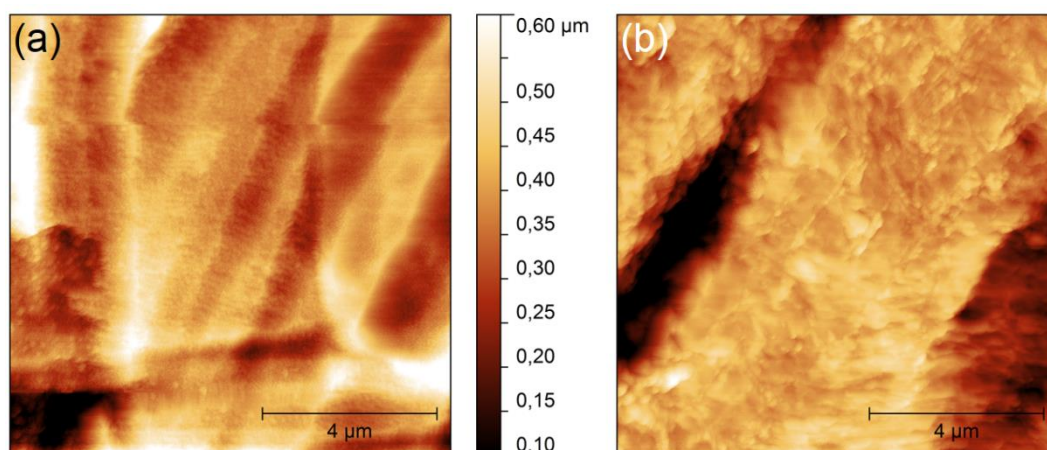
Figure 2.2.7. AFM topography images of sputtered Au (a) and Co (b) foils. The image sizes are 10 x 10 μm^2. The determined RMS values are 95.5 nm for the Au foil (a) and 75.2 nm for the Co foil (b).

CL-PES measurements and a calibration curve was obtained as presented in Figure 2.2.8.The CL-PES results on K intercalated MnPc together with the fitting procedure are presented in more detail in section 3.2.2.2. Here, the calibration procedure is shortly presented.

To determine the amount of K in the molecular film after each doping procedure the K 2p and C 1s fitted peaks were considered in the calculations. Taking into account the different cross sections for K and C atoms (see *e.g.* Table 2.1 and reference

[Yeh85]) and the number of C atoms in the molecule the ratio of the peak areas yields the amount of K in the organic film according to equation:

$$N_K = N_C \frac{A_K}{A_C} \frac{\sigma_C}{\sigma_K}, \tag{19}$$

where N_K and N_C, A_K and A_C, and σ_K and σ_C represent the number of atoms per molecule, the core level peak areas, and the cross sections of K and C, respectively. The determined N_K (K / MnPc) values after each doping procedure are plotted in Figure 2.2.8 function of the doping time. The slope of the linear fit yields the doping rate $r = (0.15 \pm 0.02)\ \mathrm{min}^{-1}$ in K atoms per molecule per minute. This value was used to determine the amount of K dopant in the rest of the experiments. In all experiments the K source was mounted at 10 mm in front of the sample and was operated at the same heating current of 7.0 A. Please note, as already mentioned in section 2.2.3, the transmission function of the spectrometer was considered to be constant in the short energy range (~10 eV) covering both core levels.

Finally, a list of the investigated molecules by different techniques is given in Table 2.2. With different symbols the implemented measurements processes are listed. An extension of the table is presented in the following, *In Situ* Spectroscopic Ellipsometry subchapter (Table 2.3).

Equation	y = a + b*x	
		Value	Error
K / MnPc	Intercept	0	--
	Slope	0.15	0.02
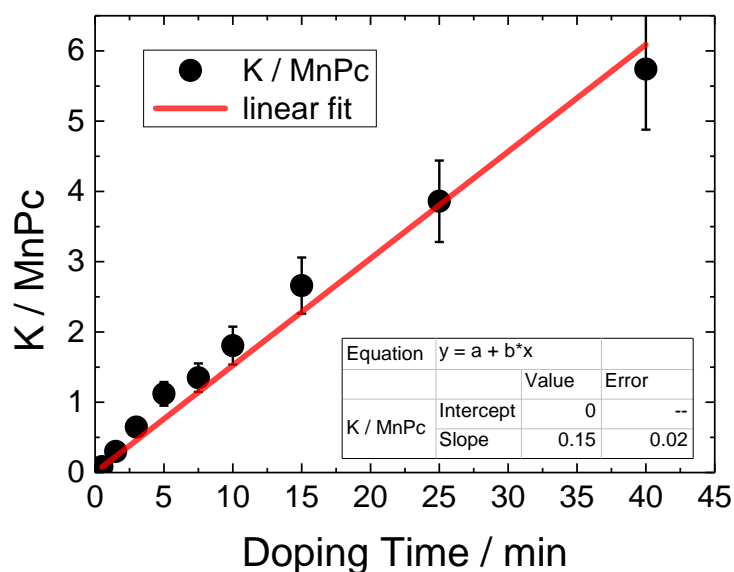
Figure 2.2.8. The number of K atoms per MnPc molecule determined by CL-PES measurements (black symbols). The red line represents the linear fit. The resulting rate is 0.15 min^{-1} with the error of 15 %.

	CuPc	MnPc	Alq$_3$	α-NPD
VB-PES and IPES	**X**	**X O +**	**X O**	
CL-PES	**X**	**X O**		
NEXAFS	**X**	**X O**		

Table 2.2. Measurement techniques applied for the different molecular systems together with the studied processes: **X** → pristine material or thickness dependent study, **O** → doping process, **+** → oxidation or air exposure.

2.3. *In Situ* Spectroscopic Ellipsometry

Spectroscopic Ellipsometry (SE) is a non-destructive optical measurement technique which is widely used in industry and fundamental research to determine film thicknesses and/or dielectric functions of the studied materials. Moreover, due to its high sensitivity in a large range of thicknesses it can be utilised to study layers with bulk-like properties down to films with thicknesses <1 nm [Gord06, Haid12]. It is more often used in characterisation of insulating and semiconducting materials which have a wide range of transparent region in their optical spectra. This property is employed for exact film thickness determination. With the proper modelling techniques, however, SE can even be employed in studying layers without transparent region in the spectra, *e.g.* metal thin films [Haid12].

SE is very well suited to characterise molecular films [Himc05, Gord06, Zahn06, Haid14]. It is mostly used to determine non-invasively the film thicknesses and more importantly their optical properties. In this work SE was employed to study *in situ* the optical properties of three representative molecules (MnPc, Alq$_3$, and α-NPD) in their pristine form and the effect of oxidation and reduction processes.

In the following subchapters theoretical considerations on polarised light are shortly presented. The *in situ* SE setup is introduced afterwards. In the last part the ellipsometric parameters and the data analysis procedure are introduced by giving two examples. Without going much into the detail a layer model is built and the film thickness and optical constants are determined.

2.3.1. Theoretical Background

Ellipsometry measures the change in the polarisation after reflection on a sample surface. The polarisation of the electromagnetic wave refers to the behaviour in time of one of the field vectors appropriate to that wave, *i.e.* electric field, observed at a fixed point in space [Azza87]. The light wave is composed of the electric vector (**E**), the magnetic vector (**B**) and the wave vector (**k**) perpendicular on each other as sketched in Figure 2.3.1(a). The light propagates along **k** (in an isotropic media) and for a monochromatic wave the time variation of **E** is sinusoidal [Azza87] (Figure 2.3.1(a)). Mathematically the equation can be written as:

$$E = E_0 \cos(\omega t - Kx + \delta), \tag{20}$$

where E_0 is the amplitude of the wave, ω represents the angular frequency, K is the wavenumber, and δ is the initial phase.

The state of polarisation of the light wave is defined by the electric field **E** because at the interaction of light with matter it exerts much greater force on the electrons than the magnetic field **B**. If all the waves existing in a light beam are added together the resulting light can be polarised or unpolarised. If at one certain point in space different waves have different orientation of **E** then the light is unpolarised. However, if all the waves have the same orientation of **E** it is said that the light is polarised.

The plane of incidence is defined as the plane which contains the incident beam, the reflected beam and the normal to the sample surface (Figure 2.3.1(b)). For the polarised light at one point on the incidence axis the **E** vector can be decomposed into two components with regard to the plane of incidence: $\vec{E}_p$ and $\vec{E}_s$. $\vec{E}_p$ is the component in the plane of incidence and $\vec{E}_s$ is perpendicular to it. The two components have the same angular frequency and wavenumber.

The most general state of polarisation is the elliptically polarised light. It is achieved if the phase difference has a value different from 0, $\pi/2$ and $-\pi/2$, or if the phase difference is equal to $\pi/2$ or $-\pi/2$ but the amplitudes of $\vec{E}_p$ and $\vec{E}_s$ have different values. For the special cases when $\delta_p - \delta_s = 0$ the light is linearly polarised and when $\delta_p - \delta_s = \pi/2$ or $-\pi/2$ the light is right-handed or left-handed circularly polarised, respectively. The names for the polarisation states are given by the shape the electric vector describes in time at a given position.

In the following the material properties are defined and the relations between them are given. For an absorbing material the complex refractive index ($\tilde{n}$) is given by the relation:

$$\tilde{n} = n + ik, \tag{21}$$

where n is the refractive index and k is the extinction coefficient which is related to the absorption coefficient (α) at specific wavelength (λ) by the formula:

$$\alpha = \frac{4\pi k}{\lambda}. \tag{22}$$
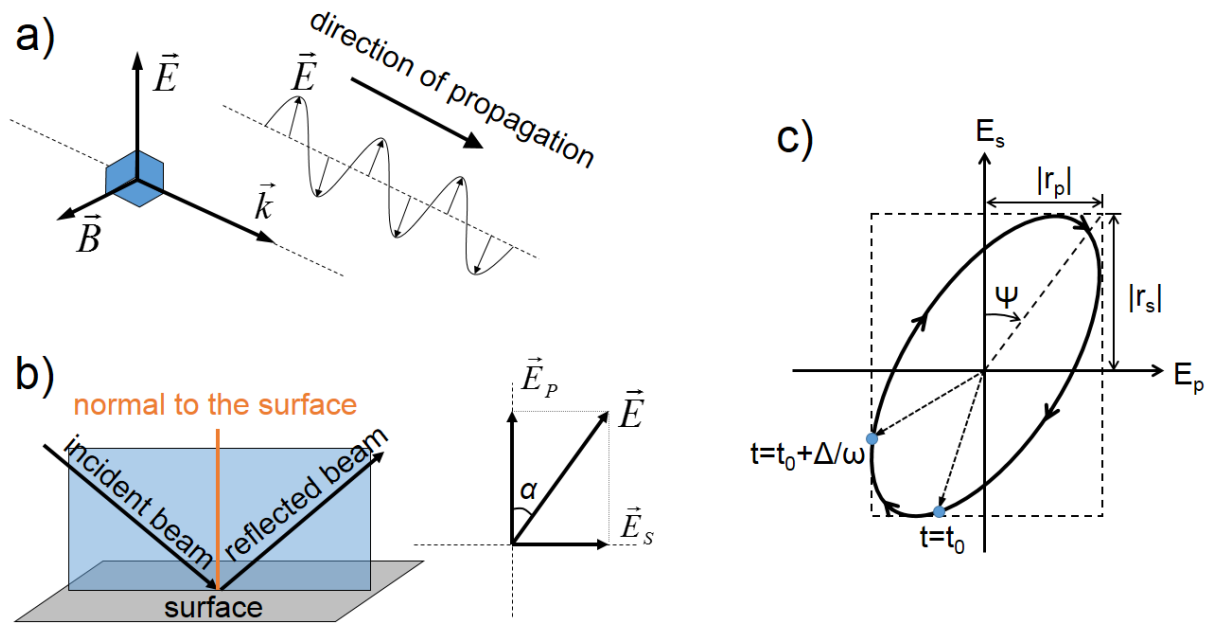
Figure 2.3.1. (a) The electric vector **E**, magnetic vector **B** and the wave vector **k** together with the propagation of a sinusoidal wave. (b) The definition of the plane of incidence together with the decomposition of the electric vector into the components in the plane (p) and perpendicular ti it (s). (c) Polarisation ellipse described by the ellipsometric angles Ψ and Δ. The propagation direction of the light wave is towards the reader.

From *Beer's law* the absorption coefficient is defined in an absorbing media by:

$$I = I_0 \exp(-\alpha d), \tag{23}$$

where I is the intensity of light at the distance $x = d$ in the material and I_0 is the intensity of light at the distance $x = 0$.

The relationship between the complex refractive index ($\tilde{n}$) and the complex dielectric function (ε) can be written as:

$$\tilde{n}^2 = \varepsilon = \varepsilon_1 + i\varepsilon_2, \tag{24}$$

where ε_1 and ε_2 are the real and imaginary parts of the complex dielectric function, respectively. With this the final relationship between the components is written as:

$$\varepsilon_1 = n^2 - k^2, \qquad \varepsilon_2 = 2nk. \tag{25}$$

It should be mentioned, however, that in the equations (21) and (24) we defined the *complex refractive index* and the *complex dielectric function* with "+" sign in front

of their imaginary part. This is a convention used in physics while in optics the two numbers are defined with "-" sign [Fuji07, Tomp05].

The quantity measured by the ellipsometer is the ratio of the complex Fresnel reflection coefficients r_p and r_s for the two polarisation states (*p*) and (*s*) sketched in Figure 2.3.1(c) and is defined as [Azza87, Tomp05]:

$$\rho \equiv \tan \Psi \exp(i\Delta) \equiv \frac{r_p}{r_s}, \tag{26}$$

where Ψ and Δ are the ellipsometric parameters, expressing the amplitude ratio and the phase difference between *p-* and *s-polarisations*, respectively. In Figure 2.3.1(c) the two angles are presented, having the following relations:

$$\tan \Psi = \frac{|r_p|}{|r_s|}, \qquad \Delta = \delta_p - \delta_s. \tag{27}$$

2.3.2. Experimental Setup and Sample Preparation

A general ellipsometer is formed of five components: the light source, a polariser, the sample, an analyser and the photo-detector. The analyser is nothing else than a rotating polariser. The light source gives unpolarised light which goes through the polariser where it is linearly polarised at a certain angle. After the reflection on the sample surface the polarisation state changes to elliptical. Afterwards the light goes through the rotating analyser and gives a sinusoidal signal at the detector. From this signal and from the angular frequency of the rotation the polarisation ellipse (see Figure 2.3.1(c)) can be deduced [Tomp05]. This is, however, the simplest configuration. In the following the setup utilised in this work is presented.

The Spectroscopic Ellipsometry measurements were performed using a commercial T-Solar™ ellipsometer with an M-2000® Rotating Compensator (J. A. Woollam Co., Inc.). It is mounted on a high vacuum chamber at a fixed angle of incidence of (69.5 ± 0.5)°, as schematically presented in Figure 2.3.2. The working principle is similar to the one presented above with some crucial differences: the linearly polarised light given by the polariser is elliptically polarised by the rotating compensator (auto-retarder) such that after the reflection on the sample surface the polarisation state should be circular.
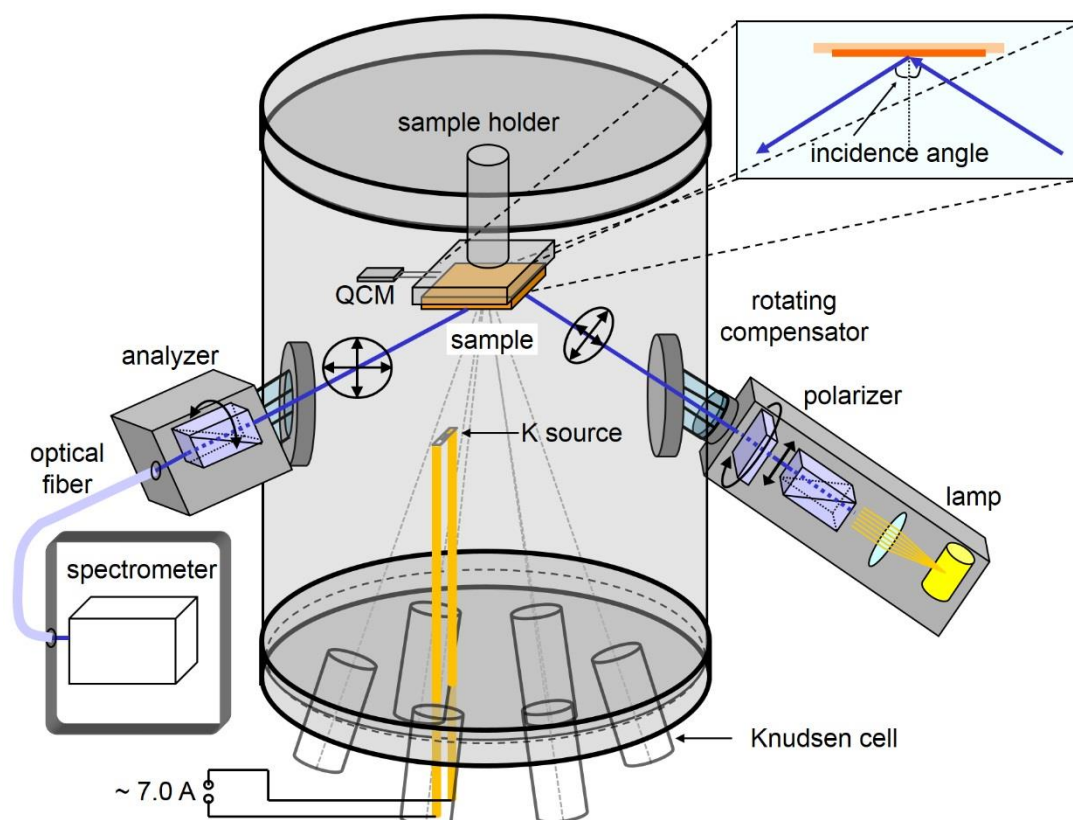
Figure 2.3.2. Schematic representation of the *in situ* Spectroscopic Ellipsometer setup mounted on the high vacuum OMBD chamber. The path of the light beam is sketched by the blue line which enters and exits the chamber through viewports and is reflected on the sample surface. The sketch on the upper right hand side represents a magnified side look of the light path at the reflection on the sample surface. The sample is mounted on top of the chamber while the organic material is sublimed from the Knudsen cells from the bottom. The QCM is in the vicinity of the sample. The K source is mounted in front of the sample at a close distance.

This configuration is also referred to as rotating compensator ellipsometer. The main advantages are: accurate measurement of Ψ and Δ over the complete angular range ($\Psi \in [0°, 90°]$ and $\Delta \in [0°, 360°]$) and the capability to directly measure the depolarisation [Wool10]. The spectral range is between 0.73 eV and 5.03 eV. The integration time per spectrum was set to 10 sec.

The base pressure in the vacuum chamber is better than 5 x 10^{-7} mbar. All experiments were performed *in situ*. The molecules were sublimed by OMBD from Knudsen cells mounted at the bottom of the chamber (Figure 2.3.2).

As substrate one side polished, (111) oriented *p-type* silicon single crystals was chosen which had a native oxide layer (~2 nm) on top. Its well-known optical properties provide a big advantage in building the models for fitting (see *e.g.* subchapter 2.3.3).

For cleaning the substrates were dipped in acetone, ethanol, and de-ionised water in an ultrasonic bath for 10 minutes each. Afterwards they were dried with nitrogen gas and immediately introduced into the vacuum chamber. The studied molecular films had thicknesses around 70 nm. The deposition rates were 1 nm/min for Alq$_3$ and α-NPD and only 0.2 nm/min in the case of MnPc due to higher deposition temperature (see *e.g.* subchapter 2.1). The film thicknesses and rates were determined from ellipsometric data analysis combined with the frequency shift of a QCM mounted close to the sample (see Figure 2.3.2).

Alkali metal, *i.e.* potassium (K), was evaporated from a dispenser (SAES Getters S.p.A, Italy) mounted close to the sample (Figure 2.3.2). The evaporation rate was kept constant. The frequency shift of the QCM was strongly influenced by the heat of the glowing K source in the close vicinity, thus the amount of K had to be determined by other means. To relate the spectra the doping time was chosen as parameter.

Exposure of the samples to gas was performed through a leak valve. The pressure inside the chamber was constantly monitored. The gases used in the experiments were O$_2$ (5N), N$_2$ (6N), and atmospheric air.

Finally, Table 2.3 lists the processes applied for different molecular systems studied in this work by *in situ* SE.

	CuPc	MnPc	Alq$_3$	α-NPD
in situ SE		**X O +**	**X O**	**X O**

Table 2.3. List of the studied processes applied for different molecular systems: **X** → pristine material or thickness dependent study, **O** → doping process, **+** → oxidation or air exposure.

2.3.3. *In Situ* SE Data Interpretation

Data acquisition and analysis was performed using the CompleteEASE software from J. A. Woollam Co., Inc. To analyse the measured data a layer model has to be built which reflects the structure of the sample. In a fitting procedure values for the unknown parameters are given and the generated data is compared with the measured one. The difference is quantified by the mean square error (MSE):

$$MSE = \sqrt{\frac{1}{2N-M}\sum_{i=1}^{N}\left[\left(\frac{\Psi_i^{mod}-\Psi_i^{exp}}{\sigma_{\Psi,i}^{exp}}\right)^2 + \left(\frac{\Delta_i^{mod}-\Delta_i^{exp}}{\sigma_{\Delta,i}^{exp}}\right)^2\right]}, \qquad (28)$$

where N is the number of experimental points, M is the number of parameters, σ is the standard deviation and the superscripts mod and exp refer to the generated (modelled) and measured (experimental) data, respectively. The recursive algorithm is fitting the variables until the MSE is minimised [Wool10].

The raw data of a SE measurement contains the ellipsometric parameters Ψ and Δ in the measured energetic range. An example is plotted in Figure 2.3.3(a). In a variable angle setup there is a separate dataset at each measured angle. However, due to the fixed angle of incidence of the setup employed in this study the *in situ* measurements provided only one dataset. To obtain information on film thickness and optical constants a model has to be built like the one in the inset of Figure 2.3.3(a). In this simple example the Si substrate has a native oxide layer on top with unknown thickness. In this specific example the optical constants of both the semi-infinite Si substrate and the thin SiO$_2$ layer are known. The only fitting parameters are the film thickness and the exact value of the angle of incidence. The latter can slightly vary (<0.2°) at each sample change. Therefore it has to be exactly determined for each sample. The thickness of the oxide layer for this particular substrate was determined to be (1.7 ± 0.1) nm (inset Figure 2.3.3(a)). The generated data from the fit is plotted with the dashed green lines in Figure 2.3.3(a).

Often, besides the film thickness also the optical properties are not exactly known for the studied layer. The difficulty in this case is the coupling between the unknown parameters: thickness and optical constants. However, if the material is transparent in the low energy region a Cauchy layer [Smit01, Gord04] can be used to determine the film thickness. Knowing the thickness the optical constants can be determined in various ways, one of it will be presented in the followings.

The Cauchy layer is a modelled layer with the optical constants which have the following relations function of wavelength of light (λ):

$$n(\lambda) = A + \frac{B}{\lambda^2} + \frac{C}{\lambda^4} + \cdots \quad \text{and} \quad k(\lambda) = 0. \qquad (29)$$

This is also referred to as the Cauchy dispersion function [Smit01]. In practice only the first two terms are important with the unknown variables A and B.
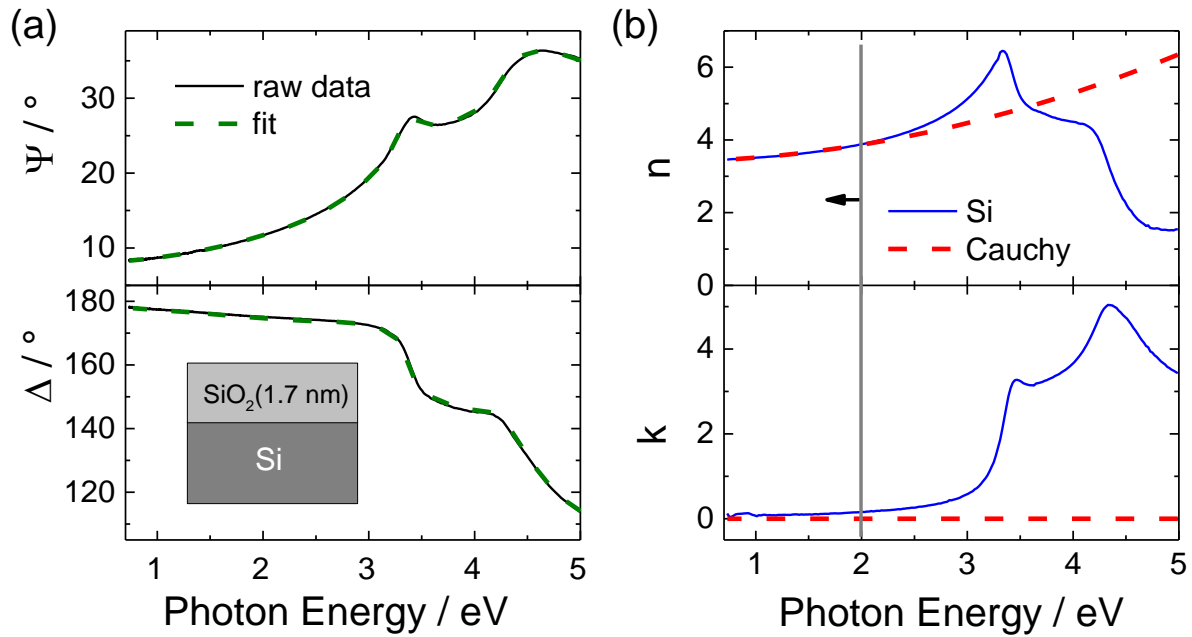
Figure 2.3.3. (a) The ellipsometric parameters Ψ and Δ deduced from measured data (full black lines) and the fitted data (dashed green lines). Inset: layer model used for the fit. (b) The real (n) and imaginary (k) part of the optical constants of Si (full blue lines) and the fit using the Cauchy dispersion formula (dashed red lines). The vertical grey line delimits the spectral region used in the fit.

An example for a Si sample is plotted in Figure 2.3.3(b). In the energy region lower than 2 eV the absorption is very small and the Cauchy model can be utilised. The results of the fit are: $A = 3.396$ and $B = 0.182\,\text{nm}^2$. In the figure the optical constants of this layer are plotted with red dashed lines. In the energy region 0.7 eV - 2.0 eV the measured and generated data overlap very well.

After the film thickness is known the dielectric function (optical constants) can be determined by using a Kramers-Krönig (KK) consistent B-Spline layer [Johs08] which is implemented in the data analysis software. The "B-Spline" stands for "basis-spline" and is composed of a basis set of polynomial spline functions [Johs08]. Besides the KK consistency it also ensures that ε_2 is always positive. Its advantage over a general oscillator layer is the efficient computation, especially for the study of a large set of spectra. The KK dispersion relations relate the real part of the optical susceptibility to the imaginary part (see *e.g.* [Hutc92, Kram27, Krön26]).

The example of Alq3 film growth monitoring is presented in Figure 2.3.4. The upper inset schematically shows the layer model: the substrate is composed of Si with native oxide on which the Alq3 film is deposited. During deposition *in situ* SE measurements were performed. For each time slice a Cauchy layer in the energy range

0.7 eV – 2.5 eV was used in the fit for the Alq$_3$ thickness determination. This thickness is plotted against measurement time in the lower inset. It should be noted that the measurement does not start from 0 nm due to a delay in starting the acquisition. The linear growth shows the stability of the evaporation through time.

At last, for the film thickness of x = 69 nm the B-Spline layer is employed in the model. The fit is Kramers-Krönig consistent and yields the dielectric function of the Alq$_3$ layer (blue line in Figure 2.3.4).
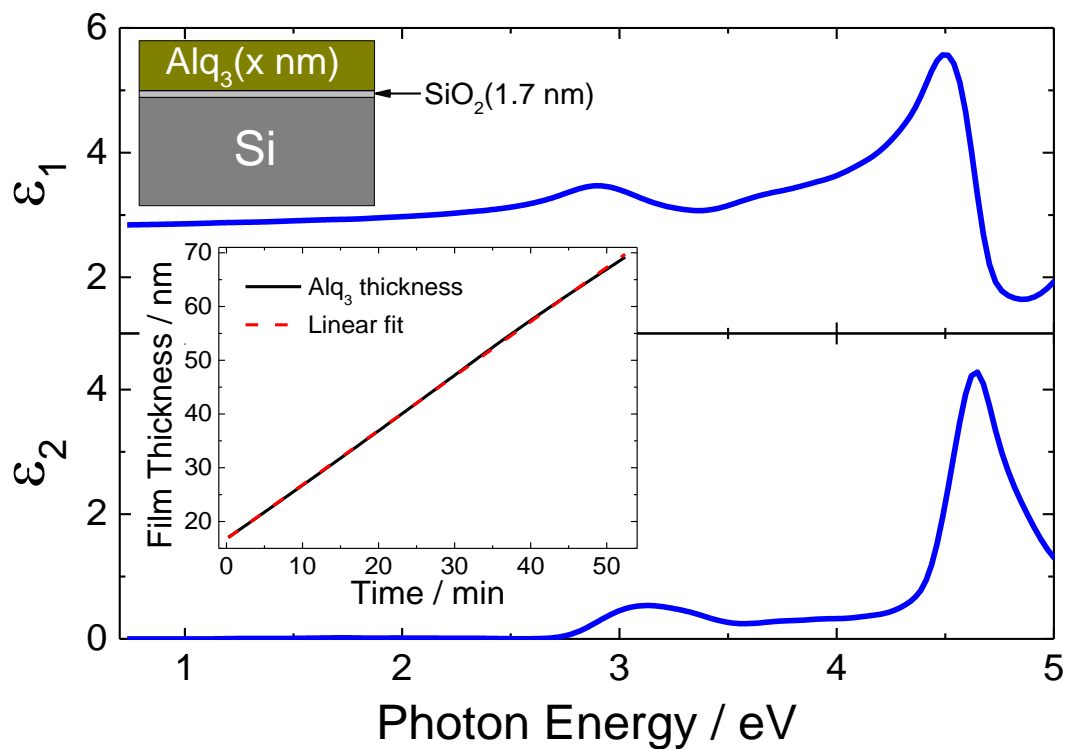
Figure 2.3.4. The real (ε_1) and imaginary (ε_2) part of the dielectric function of Alq$_3$ film (69 nm) deposited on Si with native oxide. Upper inset: the layer model employed in the fit. Lower inset: Alq$_3$ film thickness vs. measurement time. The full black line represents the results of the Cauchy layer fittings at each acquisition. The dashed red line is a linear fit of this data.

3. Results and Discussions

This chapter presents in detail the results of the measurements performed on the four investigated molecules. Each molecule has a dedicated subchapter with introduction part, followed by sections dedicated for each experimental technique and measured system in part, and finally the conclusions section of each subchapter. Please note, the introduction sections are not particularly labelled, but they are given under the title of each subchapter. These sections introduce a thorough literature research with regard of the molecule examined in the particular system and the investigative techniques. The subchapters deal with the molecules in the following sequence: CuPc, MnPc, Alq$_3$, and α-NPD.

3.1. Copper Phthalocyanine: M-O Interface

Metal phthalocyanines (MPcs) are chemically and physically stable molecular dyes vastly used in science and technology. Copper phthalocyanine (CuPc) is the most important one and is manufactured on a large scale [Würt11]. It is probably the most studied molecule in the family of phthalocyanines and porphyrins. It has three polymorphs, among which β-CuPc is the thermodynamically most stable one [Würt11].

As underlined by van den Brink and Mopurgo, organic materials are rarely magnetic, however the MPcs represent an exception to the rule [vdBr07]. Recently, CuPc is being considered a good candidate for molecular spintronics. Studies on spin injection and transport properties are being reported [Cinc09, Stei11, Lach12]. The most studied hybrid interfaces are between Cobalt, due to its excellent spin filtering properties, and different organic molecules, *e.g.* Alq$_3$ [Caru05, Barr10], CoPc [Lach12], FePc [Schm11, Lach12], and especially CuPc [Schm11, Lach12, Stei11, Aris09A, Cinc09].

Valence Band Photoemission Spectroscopy (VB-PES) and Inverse Photoemission Spectroscopy (IPES) are complementary techniques to analyse the occupied and unoccupied electronic states [Zahn06], respectively. CuPc is well characterised in literature by VB-PES [Hill00A, Gorg05, Zahn06, Grob09, Peis02, Schm11, Gorg06] and IPES measurements [Rocc90, Hill00A, Yosh01, Gorg04, Gorg05, Zahn06, Schm11, Gorg06]. Thus, its bulk-like electronic properties were

determined on thicker films [Rocc90, Hill00A, Yosh01, Zahn06, Grob09] where the influence of the substrate is minimal. The inorganic semiconductor-organic semiconductor (I-O) [Gorg04, Gorg05] and metal-organic semiconductor (M-O) [Peis02] interfaces were characterised by thickness dependent studies starting with ultra-thin (mono-) layers of CuPc up to bulk-like thicknesses (~20 nm). However, this geometry builds up only half of a device. In addition, to study the upper contact interface, metal was evaporated with gradual thicknesses on thicker CuPc films [Gorg06, Schm11]. Chemical reactions and inter-diffusion [Schm11] or the absence of inter-diffusion (*e.g.* for Co on pentacene) [Popi06] were observed.

The combination of VB-PES and IPES techniques was applied to study the impact of the substrate on the electronic properties of CuPc deposited on Au and Co substrates. Previous thickness dependent VB-PES and IPES studies of CuPc deposited on hydrogen passivated Si(111) present *band bending* behaviour [Gorg05], as expected for an I-O interface [Scot03]. At the M-O interface a *band gap opening* is expected, induced by the image charge potential [Knup05, Flor09, Tsip02, Scot03, Neat06]. This represents the electric potential produced by the image of the molecular electron cloud mirrored in a conductive, *e.g.* metal, substrate. Au as a non-magnetic and non-reactive [Peis02] substrate was used as reference. The magnetic and more reactive Co [Schm11] substrate provides different properties at the interface with CuPc which are of high interest for possible spintronic applications.

3.1.1. VB-PES and IPES Measurements

We studied the M-O interface between CuPc and the ferro- and diamagnetic metal substrates of Co and Au, respectively, by performing thickness dependent VB-PES and IPES measurements. Figure 3.1.1 displays the spectra evolution with increasing thickness of the CuPc films on the two metal substrates.

From the secondary electron cut-off (Figure 3.1.1(a) and (e)) the work functions (Φ) of the substrates and of the consecutively deposited CuPc films are determined. The difference between Φ_{Co} (or Φ_{Au}) and Φ_{CuPc} defines the interface dipole (Δ).

Figure 3.1.1(b) and (f) show the evolution of the valence band region with increasing CuPc film thickness on the Co and Au foils, respectively. The spectra plotted with black empty rectangles represent the clean substrates. The valence band

photoemission spectra of Co is smooth and featureless with a well-defined high intensity Fermi edge given by the low lying d-band states. Au on the other hand presents strong d-band features between 2 eV and 6 eV and as well a well-defined Fermi edge.
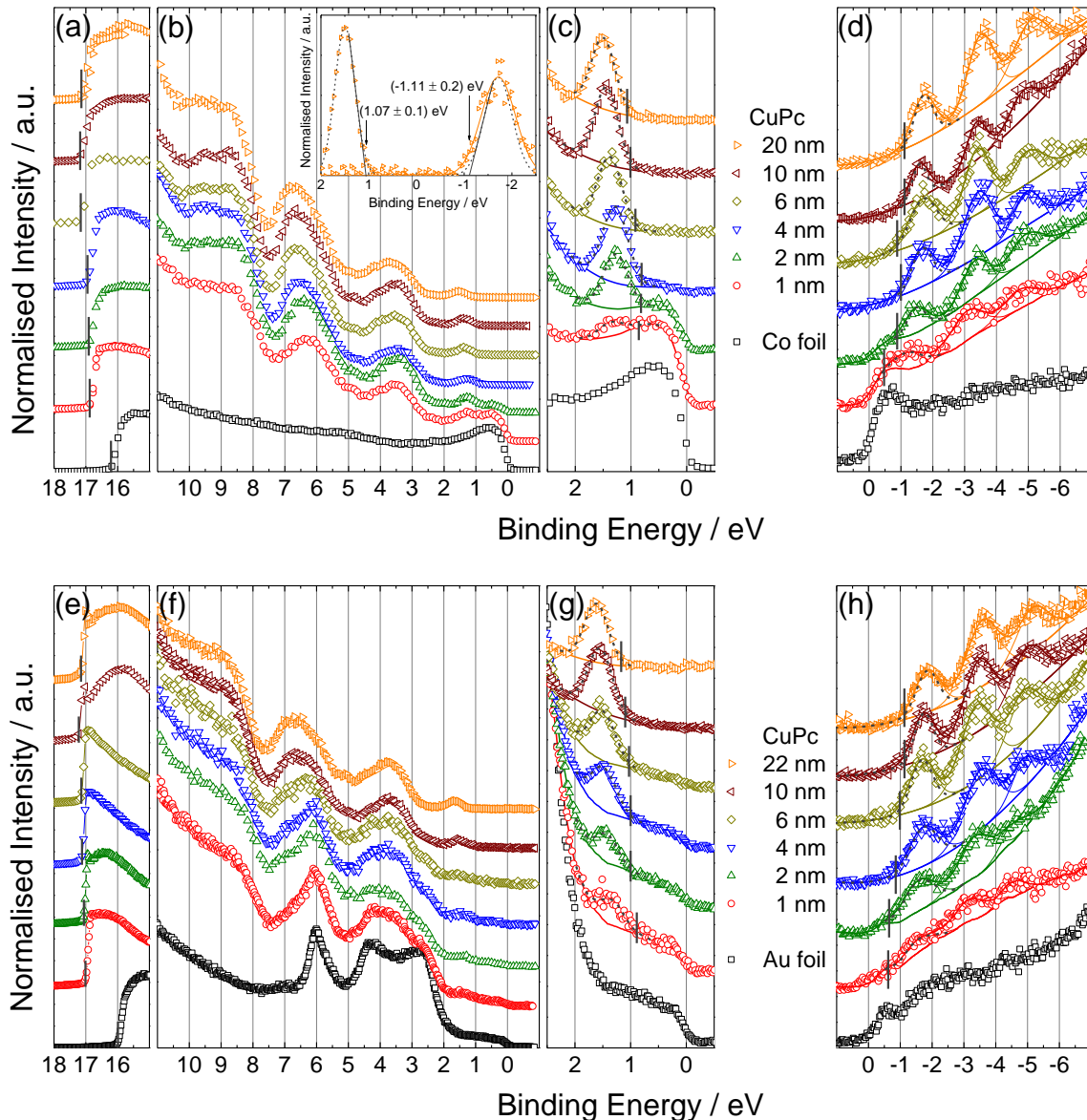
Figure 3.1.1. Thickness dependent VB-PES and IPES measurements on CuPc deposited on Co (a, b, c, d) and Au foils (e, f, g, h). The secondary electron cut-off (a) and (e), the HOMO onset (c) and (g), and the LUMO onset (d) and (h) positions are marked by vertical bars for CuPc on Co and Au foils, respectively. The valence band region overview is presented in (b) and (f) for CuPc on Co and Au substrates, respectively. The inset in (b) shows how the HOMO and LUMO onset positions were determined for the 20 nm CuPc film.

The features evolving closest to the Fermi edge in Figure 3.1.1(c) and (g) represent the highest occupied molecular orbital (HOMO) of CuPc. The HOMO onset was determined by fitting the spectra with a Gaussian peak and a polynomial background and is marked in the figure by vertical bars. In case of the thinner films (< 6 nm) the substrate signal was subtracted accordingly.

Furthermore, the inverse photoemission spectra evolution with increasing film thickness is plotted in Figure 3.1.1(d) and (h). The Co and Au substrates give different spectral shapes also in the IPES region: Co has a single feature close to the Fermi edge, while Au has a multitude of features belonging to different orientations of its polycrystalline surface [Häbe01]. The spectra were fitted like in the HOMO region with three Gaussian peaks of which the closest one to the Fermi level represents the lowest unoccupied molecular orbital (LUMO). To exclude the experimental broadening (0.5 eV) the LUMO peak was deconvoluted [Zahn06] according to equation (15) from section 2.2.2. The deconvoluted peaks are plotted with dashed dark grey lines and their onset is marked by vertical bars.

The inset in Figure 3.1.1(b) exemplifies the HOMO and LUMO onset determination for the CuPc(20 nm)/Co sample with subtracted backgrounds. In this manner the onset positions were determined for each film thickness. Please note that the energy scales in Figure 3.1.1 represent the binding energies (BEs) with regard to the Fermi level ($E_F = 0$).

At this point we can identify at each film thickness the following quantities: Φ, Δ, ionization energy (IE), electron affinity (EA), and the transport band gap energy (E_t). All the determined quantities are plotted in Figure 3.1.2(a) function the CuPc film thickness.

First, for the clean substrates the Φ were determined. These have the values (5.0 ± 0.1) eV and (5.2 ± 0.1) eV for the polycrystalline Co and Au substrates, respectively, in good agreement with literature data [Mich77]. The values are plotted in Figure 3.1.2(a) as black full and empty squares for the Co and Au substrates, respectively, at the CuPc film thickness of 0 nm. The values of the vacuum level (VL) are given in Figure 3.1.2(b) as well. All the other parameters are obtained from measurements on CuPc films with increasing film thicknesses and are plotted in Figure 3.1.2(a) and (b).

In Figure 3.1.2(a) the Φ, IE, EA, Δ, and the E_t are plotted at each film thickness. The quantities are given in BE with regard to the VL energy position (E_v).

Figure 3.1.2(b) represents the energy values of the E_v, the HOMO onset (HOMO), and the LUMO onset (LUMO) with regard to the Fermi level (E_F). Full and empty symbols in both Figure 3.1.2(a) and (b) represent values for measurements on Co and Au substrates, respectively. Grey symbols are data points for a second set of samples. Each symbol represents the quantity given by its coloured counterpart and is not explicitly provided in the legends. Note that the energy scales are flipped, so that Figure 3.1.2(b) resembles the energy level diagram in Figure 3.1.2(c). The dashed, short dashed, and solid lines in Figure 3.1.2(a) and (b) are guidelines for the eye. The short dashed and the solid lines mark the evolution of the empty and full symbols, respectively. The dashed lines mark the average evolution between the empty and full symbols.

The energy band diagram (Figure 3.1.2(c)) sketches the energy levels at the metal (Co or Au) and organic semiconductor (CuPc) interface. On the left hand side the bulk properties of the two metals are represented. To highlight the interface properties present at any M-O junction the average energy values are given for the CuPc covered films (independent from metal substrate). The sketch is plotted against CuPc film thickness. On the right hand side (thicker film) the bulk-like properties are given.

The similarities and more interestingly the differences of the CuPc properties on the two metal substrates are discussed in the following. Previous thickness dependent VB-PES and IPES measurements on CuPc deposited on hydrogen passivated Si(111) (H-Si) show a *band bending* at the I-O interface [Gorg05]. The band gap remains constant for all film thicknesses but the HOMO and LUMO shift parallel towards higher BEs. The overall value of the shift is (0.4 ± 0.1) eV [Gorg05]. As shown in Figure 3.1.2(c) the M-O interface exhibits a *transport band gap opening*. It saturates above 10 nm film thicknesses having the final value of (2.2 ± 0.3) eV as previously reported [Hill00A, Gorg05, Zahn06]. The transport band gap opening is the result of the image charge potential screening [Knup05, Flor09] for very thin films.

A decrease of the E_t close to the metal surface was reported by Tsiper *et al.* [Tsip02] in their VB-PES and IPES studies of 3,4,9,10-perylene-tetracarboxylic dianhydride (PTCDA) deposited on silver and scanning tunnelling spectroscopy studies of PTCDA on Au. They observe a reduction of E_t by 400 meV (200 meV in the occupied and 200 meV in the unoccupied electronic states region) for monolayer
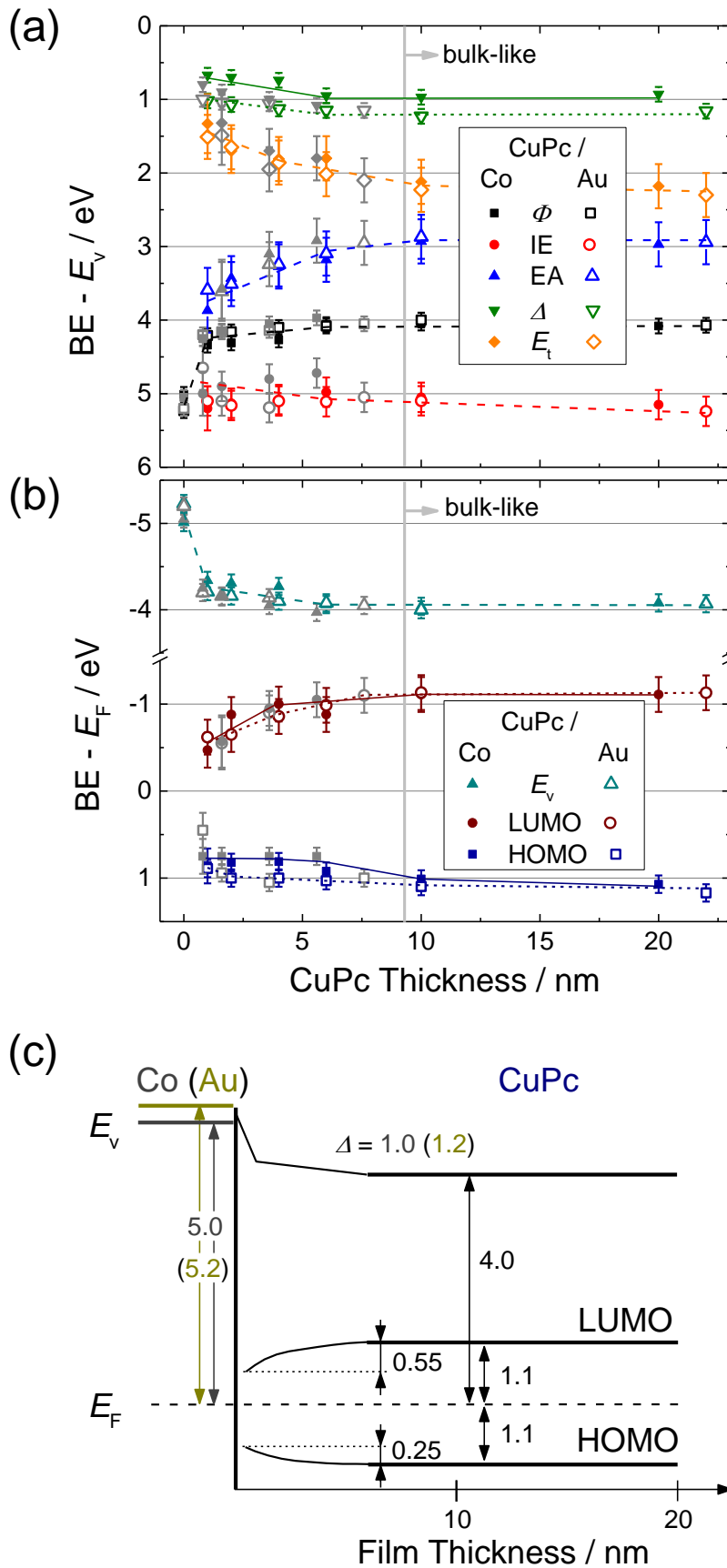
Figure 3.1.2. (a) Evolution of the work function (Φ), ionization energy (IE), electron affinity (EA), interface dipole (Δ), and transport band gap (E_t) of a CuPc film deposited on Co (full symbols) and Au (empty symbols) substrates as a function of film thickness. (b) Energy of the vacuum level (E_v), LUMO onset and HOMO onset positions for CuPc on Co (full symbols) and Au (empty symbols) foils as a function of film thickness. Grey symbols represent the second set of measurements on new samples. Dashed, short dashed and solid lines are guidelines for the eye. (c) Schematic energy band diagram of the CuPc/Co(Au) interface (for simplicity the average values from measurements on both substrates are plotted).

coverage in comparison with thicker films. They explain this by the different polarisability of the metal substrate (at the interface) and the vacuum (at the film surface). It is also noted that the interface dipole (*i.e.* the work function of the substrate) has no influence on the reduction of E_t. It was even observed that on the same type of metallic substrate molecules with different interface dipoles (work functions) show the same amount of shifts of their HOMO levels [Knup05]. Moreover, MnPc deposited on Co foil shows a smaller band gap opening of 0.35 eV [Haid13A]. Finally, theoretical calculations of benzene physisorption on graphite (0001) predict as well a strong renormalization of the electronic gap [Neat06], giving rise to a *band gap opening*.

In Figure 3.1.2(a) with orange symbols the E_t for the CuPc on Co (and Au) is plotted. It grows with film thickness from (1.4 ± 0.3) eV for 1 nm CuPc to the final value of (2.2 ± 0.3) eV for CuPc films larger than 10 nm. The band gap opening is a consequence of the shift of both the HOMO and the LUMO onsets away from the Fermi energy, which are plotted in Figure 3.1.2(b). Partially influenced also by the position of the VL with regard to E_F (Figure 3.1.2(b)) the shifts are reflected in the IE and the EA (Figure 3.1.2(a)). Thus, the EA has a larger change with CuPc thickness than the IE.

The position of E_v with regard to E_F is plotted with triangles in Figure 3.1.2(b) and is given in negative values. It actually represents the Φ, which is plotted in Figure 3.1.2(a) with rectangles. For the thinnest CuPc film (1 nm, first deposition) E_v has a large shift of ~0.8 eV toward E_F. This is followed by a smoother shift with a total value of Δ up to 1.0 eV and 1.2 eV on Co and Au substrates, respectively. The values saturate above 10 nm film thicknesses. The reason for the shift is the formation of an interface dipole (plotted with green triangles in Figure 3.1.2(a)) which has a higher value by 0.2 eV on the Au substrate than on the Co substrate, *i.e.* 1.2 eV, in agreement with Peisert *et al.* [Peis02]. There, the authors investigated the interface between single crystalline and polycrystalline Au and CuPc molecules by VB-PES and CL-PES techniques. The formation of a 1.2 eV interface dipole and a shift of the HOMO towards higher BE by 0.25 eV was observed [Peis02], which is in good agreement with the observations of this study. It was shown that CuPc thin films on both single- and polycrystalline Au surface have a similar behaviour for thicknesses larger than 1 nm, although the molecular growth is most probably quite different. The shift of the HOMO in the early stages was ascribed to final state screening effect induced by the metallic substrate [Peis02]. The complementary IPES measurements of this study give a total shift of the LUMO onset by 0.55 eV away from the Fermi level. The final bulk-like

positions of the HOMO and the LUMO are at 1.1 eV beneath and above the Fermi level, respectively (see Figure 3.1.2(c)).

The substrate of higher interest is the polycrystalline Co foil due to possible spintronic applications like magnetic tunnel junction [Barr10]. CuPc behaves similarly on the Co like on the Au substrate except for some essential differences. First of all, Co has a smaller work function, which induces a smaller interface dipole of 1.0 eV (green full triangles in Figure 3.1.2(a)). The second and more obvious difference is within the HOMO region (Figure 3.1.2(b)). The HOMO position is closer to the E_F by 0.2 eV which is highlighted in Figure 3.1.2(b) by the eye guiding blue lines. This difference is not induced by the interface dipole but more likely by charge transfer to the Co substrate. With incremental thickness the onset of the HOMO of CuPc on Co saturates at larger thicknesses similarly as in the case of the Au substrate. This will be discussed in much more detail in the following paragraphs after presenting the CL-PES results on the same thin film system.

3.1.2. CL-PES Measurements

Figure 3.1.3 presents the core level spectra of CuPc, deposited with incremental thickness on Au and Co foils plotted with empty circles and full rectangles, respectively. For clarity, spectra at different thicknesses are shifted vertically to each other. There is also a slight vertical shift at the same thickness for spectra of CuPc on the two different substrates.

In Figure 3.1.3(a) the spectra of Cu $2p_{3/2}$ is shown which is fitted with a single asymmetric Voigt peak. The peak positions, marked by vertical grey lines, are different for the two samples and with increasing film thickness they shift towards higher BE.

Figure 3.1.3(b) presents the N 1s spectra for different thicknesses of CuPc deposited on Au and Co foils. The main peak at around 399 eV BE has contributions of two nitrogen atoms with different chemical environment, *i.e.* at lower BE the N atoms bound to the central metal ion (N_M) and at slightly higher BE the N atoms bound to the pyrrole rings (N_P). The two types of N atoms (source of the two components) are schematically shown in Figure 3.1.3(d). The peaks presented in Figure 3.1.3(b) with red and blue patterns for N_M and N_P components, respectively, cannot be well resolved energetically. In the fit the line shapes and the intensities were coupled.
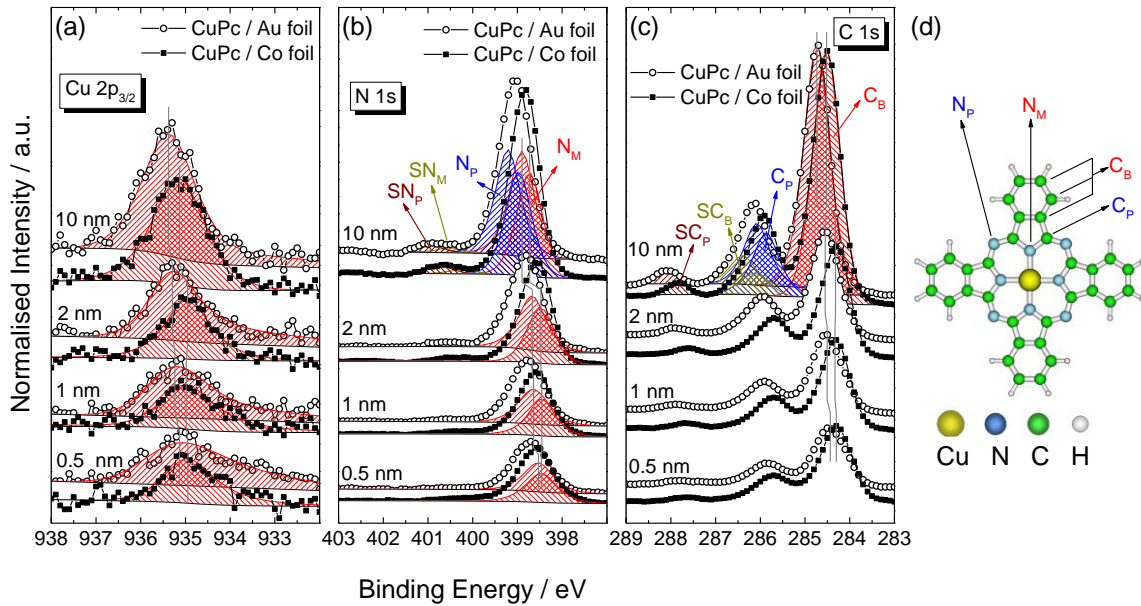
Figure 3.1.3. Core level spectra of CuPc on Co (full symbols) and Au (empty symbols) substrates, respectively, at different film thicknesses (a, b, c). Cu 2p$_{3/2}$ (a), N 1s (b), and C 1s (c) peak evolution with film thickness. N$_M$, N$_P$, C$_B$, and C$_P$ represent the N and C atoms with different chemical environments and SN$_M$, SN$_P$, SC$_B$, and SC$_P$ are their corresponding shake-up satellites. The grey vertical lines follow the Cu 2p$_{3/2}$, N$_M$, and C$_B$ features evolution. (d) Schematic representation of the CuPc molecular structure together with the different N and C species labelling.

The small line shape at higher energy is the shake-up satellite peak of the main feature composed as well of two components, SN$_M$ and SN$_P$. For clarity, the thickness evolution only of the N$_M$ component of the main peak is shown.

Between 284 eV and 288 eV BEs the 1s peaks related to carbon atoms are visible (Figure 3.1.3(c)). The main feature at ~284.5 eV is assigned to C atoms from the benzene rings referred to as C$_B$ and sketched in Figure 3.1.3(d). The second feature at ~286 eV is assigned to C atoms from the pyrrole rings, *i.e.* which are bonded to N, and is referred to as C$_P$. The small peaks labelled as SC$_B$ and SC$_P$ in Figure 3.1.3(c) are the shake-up satellite peaks of C$_B$ and C$_P$, respectively. The sum of the C$_P$ and SC$_P$ peak areas is 3 times smaller than the sum of the C$_B$ and SC$_B$ peak areas as it is expected from stoichiometry. All the C 1s peaks have a similar behaviour as Cu 2p$_{3/2}$ and N 1s, *i.e.* a shift towards higher BEs with film thickness.

The previously mentioned *shake-up satellites* are the effect of the excitation of valence electrons into higher unfilled energy levels [Hüfn03]. The energy required for the transition leads to a reduction of the kinetic energy of the primary photoelectrons. Due to the lower kinetic energies, the shake-up structures emerge at higher BEs in the

spectra. The first most likely transition is the one from HOMO to LUMO state, thus the literature [Bren04, Ruoc08, Rocc08] associates the main peak to satellite distance being equal to the HOMO-LUMO gap.

Figure 3.1.4(a) summarizes the peak positions determined in Figure 3.1.3 versus the CuPc film thickness. Note that the energy (vertical) scales are reversed for comparison with the HOMO onset position in Figure 3.1.2(b). Within the error bars all the core level peaks from CuPc on Co foil are at 0.2 eV lower BE as the ones for CuPc on Au foil. This is in good agreement with the HOMO positions within this thickness range (<10 nm). The VB-PES measurements are more surface sensitive, hence they provide similar HOMO onset positions for the 10 nm CuPc film on the two substrates, unlike the CL-PES results. The shift of the core level spectra with increasing film thickness is between 0.20 eV and 0.25 eV which is, as well, in good agreement with the 0.25 eV HOMO onset shift.

The relative position of the shake-up satellites with regard to the main peak is plotted in Figure 3.1.4(b). Orange and green symbols mark the positions of C 1s and N 1s satellites, respectively, while open and full symbols are employed to represent measurements on Au and Co substrates. To tell apart, the symbols of SC_B and SN_M are connected by continuous lines and the SC_P and SN_P positions are connected by dashed lines. First, it can be observed no difference between satellites of CuPc deposited on the Au and Co substrates. Then, the shake-up satellites of the benzene and pyrrole carbon features are relatively positioned to the main peak at 1.7 eV and 2.0 eV, respectively, and present no thickness dependency. On the other hand, the nitrogen related satellites have all the same split of 1.8 eV to the main peak, except of the very thin films for which the satellites are positioned closer to the main feature (~1.6 eV), another evidence of the band gap opening. These quantities are in a good agreement with the literature [Bren04, Ruoc08]. As underlined in a previous paragraph, the relative position of the shake-up satellites can be associated to the HOMO-LUMO transition, *i.e.* the transport gap, which for CuPc was determined by VB-PES and IPES to be 2.2 eV. This value is higher than all the shake-up relative positions (see *e.g.* Figure 3.1.4(b)). Moreover, for some of the shake-up satellites the relative energy position is even lower than the optical band gap of CuPc $(E_{opt} = 1.76\,eV$ [Zahn06]). This was observed for several molecules, see *e.g.* [Rocc08]. The lowered satellite to main peak distance in comparison to the transport gap of the molecule can be related to final state screening of the core hole and to an optimised redistribution of charge
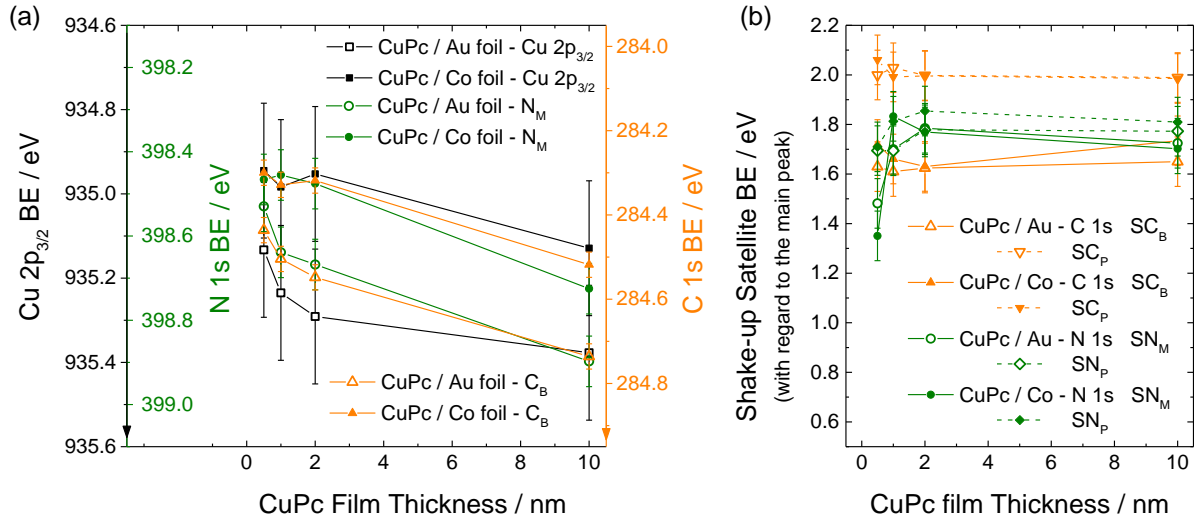
Figure 3.1.4. (a) Dependence of the core level peak positions as a function of CuPc film thickness. Data points of Cu $2p_{3/2}$ (black), N_M (green), and C_B (orange), adopted after the fittings in Figure 3.1.3. Full and empty symbols are for CuPc on Co and Au substrates, respectively. (b) Energy positions of the shake-up satellites with regard to the main peaks as a function of the CuPc film thickness.

within the molecule upon photo excitation [Rocc08, Hüfn03].

All these results raise the questions: what is the reason for the peak shifts with film thickness and why is there a difference in the core level and valence band spectra between CuPc on Au and on Co substrates? The first question was already answered in the previous sections: the image charge potential not only reduces the transport band gap for very thin films it also influence their core levels, *i.e.* all spectra are shifted towards smaller BEs as it was previously observed also for CuPc on Au [Peis02].

The second question can be addressed by taking a look at different metal-CuPc interfaces in literature. There are two geometries to determine the interface properties: evaporated CuPc on metal substrates (*bottom interface*) and evaporated metal on thick CuPc film (*top interface*). The first one excludes the possibility of metal atoms inter-diffusion into the organic layer. The high reactivity of the Co surface was observed only for ultra-thin sub-monolayer CuPc films deposited onto Co(001) [Lach12]. At the *top interface* geometry, where Co is evaporated on thick CuPc films [Aris09A, Schm11], the reactive interface between Co and CuPc is more obvious. Although Co [Popi06, Aris09A] and Fe atoms [Aris09B] do not diffuse so deep into the organic layer as Ag [Gorg06] due to their higher reactivity with the molecules, they still react with much more molecules as in the *bottom interface* configuration. Co [Schm11, Popi06, Aris09A] and Fe [Aris09B] atoms transfer charge to the CuPc molecules reducing the Cu atoms at the interface from Cu(II) to Cu(I). Our layer system is composed of rough

polycrystalline Co foil on which an island-like growth mode of the molecules is expected. This is underlined by the fact that the Fermi edge is visible up to a film thickness of 6 nm in the valence band and inverse photoemission spectra (Figure 3.1.2(c) and (g)). Due to the ill-defined interface of the samples from this work no monovalent Cu(I) state could be observed in the Cu $2p_{3/2}$ core level spectra at low thicknesses (above one monolayer coverage), as was shown by Lach *et al.* [Lach12] and by Ruocco *et al.* [Ruoc08] (sub-monolayer coverage). A full picture of the metal-organic semiconductor-metal system Co/pentacene/Co [Popi06] shows that the two interfaces are not really symmetric and should not be considered identical.

For further reasoning, the Ag/CuPc interface should also be examined. In the *top interface* configuration Ag presents no chemical reaction and exhibits high diffusion into the CuPc layer [Gorg06]. With increasing Ag thickness on CuPc the HOMO shifts by 0.2 eV closer to E_F [Gorg06] which is a sign of charge transfer from the CuPc molecules into the upper Ag layer, *i.e.* a *p-type* doping of the underlying CuPc film. Thus, their finding is similar to the CuPc/Co interface studied in this work. For the *bottom interface* configuration, the partially fluorinated CuPc molecule (F$_4$CuPc) deposited on Ag substrate was taken into consideration [Schw04]. However, in this second case the interface study shows a net charge transfer from Ag to the more electronegative F$_4$CuPc molecules. The F$_4$CuPc/Ag interface has similar properties with the *n-type* doping by K intercalation [Schw04]. Comparing valence band spectra of F$_4$CuPc films with a thickness of 2 nm deposited on silver substrate to the one deposited on gold substrate, the HOMO has an onset position with 0.4 eV higher BE [Schw04]. Since in this study the HOMO onset of the CuPc on Co is at 0.2 eV lower BE than the one deposited on Au the conclusion can be made that at the CuPc/Co interface there is a net charge transfer from the CuPc molecules to the Co substrate, hence a *p-type* kind of doping of the molecule.

3.1.3. NEXAFS: Molecular Orientation

In the previous sections the impact of the substrate on the electronic properties of the top CuPc layer was investigated. Here, the focus will be on the average molecular orientation of CuPc on the two substrates, *i.e.* Au and Co foils. The N *K edge* NEXAFS spectra of 10 nm thick CuPc film on two substrates were recorded at the
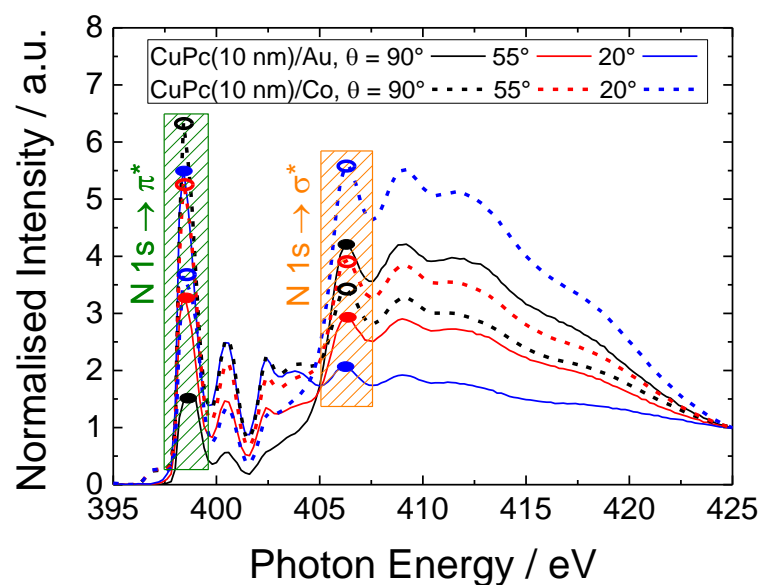
Figure 3.1.5. NEXAFS N *K edge* of a CuPc(10 nm) film deposited on Au (solid lines) and Co (dashed lines) foils at three different incidence angles: 90°,55°, and 20°. The green and orange marked regions represent the features from the $N\,1s \to \pi^*$ and $N\,1s \to \sigma^*$ transitions, respectively, employed in the molecular orientation calculations. The full and empty circles mark the intensities of these features displayed by the solid and dashed lines, respectively.

incidence angles of 90°, 55°, and 20° (see Figure 3.1.5) .Although, the $N\,1s \to \pi^*$ transitions present 3 features at 398.5 eV, 400.5 eV, and 402.5 eV which belong to transitions to different unoccupied electronic states [Molo08B], only the intensities of the first peaks were determined for the calculations. The region is marked by the green hatched area in Figure 3.1.5 and the peak intensities are marked by full and empty circles for the solid and dashed lines, respectively. The same holds for the $N\,1s \to \sigma^*$ resonances. The intensities of the first features (orange hatched area in Figure 3.1.5) were determined.

The intensity ratios of the $N\,1s \to \pi^*$ and $N\,1s \to \sigma^*$ resonances are plotted in Figure 3.1.6 for CuPc on Au and Co substrates. Equation (18) was implemented to fit the average molecular orientation angle α. The second outcome of the fit is the constant B which was used as normalisation constant. This procedure was employed for both substrates and the results are plotted in the same figure.

The average molecular orientation angles on Au and Co substrates were (37.9 ± 2.6)° and (65.7 ± 0.5)°, respectively. This means that the molecules on the Au foil tend to lie more flat and on the Co foil they tend to stand. As it was determined in
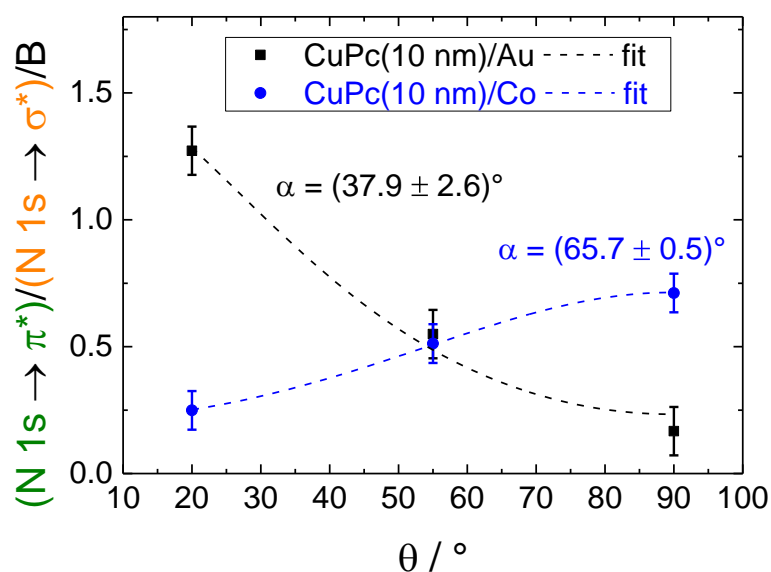
Figure 3.1.6. Normalised ratio of π^* and σ^* resonances from Figure 3.1.5 as a function of the angle of incidence. The dashed lines are the results of the fit.

section 2.2.5 both surfaces were rough after Ar$^+$ ion treatment. However, the Au foil presented a higher roughness value than the Co foil. This disagrees with the hypothesis that a rougher surface would leads to a larger angle α. Thus, the conclusion is drawn that Au has a higher interaction with the π orbitals which orients the molecules to lay more flat on the surface, while this interaction is less pronounced on the Co foil.

Thus, the question arises whether or not the molecular orientation has an impact on the electronic properties. The study by Toader *et al.* [Toad09] reveals that the orientation of the molecules plays a role in the line shape of the valence band spectra. However, the feature positions remain unchanged, only their spectral weight changes due to different orientations. Finally, it can be concluded that neither the surface roughness (see *e.g.* reference [Peis02]) nor the orientation of the molecules have an influence on the shifts observed in VB-PES and IPES and CL-PES measurements. It should be mentioned that highly ordered molecular films exhibit an intermolecular energy band dispersion (up to 0.2 eV for DiMe-PTCDI film [Gavr04]) and high intensity dependency of the HOMO feature on the average molecular orientation [Toad09] or in case of angle resolved VB-PES measurements on the take-off angle of the electrons [Okud99]. The HOMO feature intensity dependency on the average molecular

orientation was observed in this work as well (see *e.g.* Figure 3.1.1). Flat lying CuPc molecules on Au single crystal were determined to exhibit a band dispersion of less than 0.1 eV [Evan09].

3.1.4. Conclusions

Combined VB-PES and IPES measurements on CuPc thin films in dependence of film thickness were performed with the purpose to study the energy band evolution at the M-O interface. One of the employed substrates was Co which is a highly studied metal contact for spin injection into organic materials [Caru05, Barr10, Lach12, Schm11, Stei11, Aris09A, Cinc09]. The second substrate was Au, a non-magnetic and non-reactive reference metal contact, which is often utilised in PES [Peis02, Grob09].

The transport band gap of thick bulk-like CuPc films was determined to be (2.2 ± 0.2) eV in good agreement with literature [Hill00A, Gorg05, Zahn06]. For thinner (1 nm) films it decreases to a value of (1.4 ± 0.2) eV on both metallic substrates. It is the first time that the phenomenon was demonstrated on the CuPc on metal systems with the combined study of VB-PES and IPES. Tsiper *et al.* observed such a decrease of E_t for PTCDA on metals [Tsip02] and Peisert *et al.* only performed VB-PES and CL-PES on the CuPc on Au system [Peis02]. The reason for the decrease of E_t is the image charge potential [Knup05, Flor09, Tsip02] in the metal substrates which acts on the HOMO and LUMO onset positions. They are shifted closer to the Fermi level by 0.25 eV and 0.55 eV, respectively.

In addition, a difference of 0.2 eV between the HOMO onset positions on Au and Co substrates was observed for CuPc films at lower thicknesses (< 10 nm). This was strengthened by CL-PES measurements which present as well a difference of 0.2 eV between core level spectra on the two substrates. The energy positions on the Co substrates are shifted closer to E_F, implying a charge transfer from the CuPc molecular film to the Co metal substrate.

Finally, NEXAFS study provides information on the average molecular orientation on the two substrates. CuPc tends to lie on the Au foil and to stand on the Co foil. This denotes that there is a higher interaction between the Au foil and the π orbitals of the molecule.

3.2. Manganese Phthalocyanine

In this sub-chapter the electronic and optical properties of manganese phthalocyanine molecular films were studied together with their evolution upon O_2 exposure and K intercalation. The first two sections focus on the electronic properties in pristine, oxidised, and doped states. In the first section the MnPc-Co interface and the impact of O_2 on the electronic bands of MnPc is studied by VB-PES and IPES. Since the second section has significant dimensions it was divided into 4 sub-sections and will be introduced accordingly. Within the third and fourth sections the optical properties of pristine, O_2 exposed, and doped MnPc are investigated by *in situ* SE. Finally at the end the conclusions will be presented in correlation with literature findings.

Among the transition metal phthalocyanines (TMPcs) series, MnPc is the most interesting one due to its magnetic properties in bulk [Barr70, Ishi10] and in films [Heut07] at low temperatures. MnPc has an intermediate-spin state of S = 3/2 [Barr70, Tagu06] due to 3 unpaired 3d electrons which form a singly occupied highest molecular orbital (SOMO) originating from the 3d states of the central metal ion with *$1e_g$* symmetry above the highest occupied molecular orbital (HOMO) distributed on the phthalocyanine ligand [Shen10A, Grob11]. The magnetism of a single MnPc molecule was addressed by scanning tunnelling microscopy demonstrating a practical way to modulate the Kondo resonance [Fu07].

Further theoretical studies on a single MnPc molecule sandwiched between two single walled carbon nanotubes reveal its nearly perfect spin filtering properties [Shen10A]. It was already shown that the intermediate-spin ground state of MnPc S = 3/2 can be changed to S = 1 by adsorption on a Bi(110) surface [Stro12], or S = 1/2 by reaction with CO [Stro12], or O_2 [Frie12]. Moreover, the low-spin state of S = 1/2 can be obtained by ligation with pyridine [Liao05]. A high-spin state of S = 5/2, on the other hand, can be obtained by doping with alkali metals [Tagu06]. Furthermore, spin dependent conduction can be obtained by carefully selecting the metal contact at the M-O interface while chemical interactions are induced: *e.g.* physisorbed versus chemisorbed MnPc on Cu(001) and Co(001) substrates, respectively [Java10].

While for inorganic semiconductors the transport gap can be considered to be close to the optical gap and can thus be determined from optical absorption or Spectroscopic Ellipsometry measurements, the strong excitonic effects present in

organic molecules are responsible for the large mismatch between the optical and transport gaps of organic semiconductors [Hill00A, Zahn06]. The optical band gap can thus be smaller by up to 1.4 eV than the transport band gap [Hill00A], the difference represents the exciton binding energy. Therefore, for a correct transport band gap determination, the combination of direct and inverse photoemission measurements should be employed, rather than optical absorption based methods (see *e.g.* ref. [Zahn06]).

Regarding the optical band gap of MnPc, contradictory values can be found in literature. Whereas the absorption for most Pcs is negligible in the energy range below typically 1.6 - 1.7 eV, MnPc exhibits absorption features also for lower energies [Grob10]. Optical absorption spectra presented by Kraus *et al.* [Krau09] correspond well to data derived from Electron Energy Loss Spectroscopy (EELS) and show a well resolved absorption peak centred at ~ 0.5 eV. This would be an indication that the optical band gap amounts to 0.5 eV. Other studies based on absorption measurements on thin films [Raje01] or on sandwich structures [Raje05, Arsh02, Güns11] suggest an optical band gap above 2.5 eV [Raje05, Arsh02] or even above 3.0 eV [Raje01, Güns11]. Even though Spectroscopic Ellipsometry is widely accepted as a reliable method for the determination of dielectric functions and optical band gaps, ellipsometry measurements of MnPc films are still rare in literature with the exception of a study concentrating on film morphology without presenting optical properties of MnPc [Yana09].

TMPcs have been found to easily coordinate small molecules to their metal centres, *e.g.* NO [Nguy10], CO, O_2, NO_2, and NH_3 [Mori97]. Moreover, the affinity to molecular oxygen of MnPc is well known since 1959 [Elvi59], the reaction is found to be reversible [Elvi59, Leve81]. Thus, phthalocyanines have very good gas sensing properties by changing their properties upon reaction with particular gas molecules, *e.g.* O_2 [Bohr07]. Besides, the oxygen reduction capabilities were investigated in microbial fuel cells with MnPc as the cathode material [Zhao05]. In consequence, they are promising candidates for many applications. Another, even more promising tool for tuning the electrical, optical, and even spin properties of TMPc molecules is the so called doping, *i.e.* providing extra charges by *e.g.* alkali metal intercalation. The electrical conductivity of a series of TMPcs is highly increased upon K doping [Crac05, Crac06]. A special attention was given to the K intercalation of MnPc and shown that unlike the other Pcs it presents 3 stable doped phases [Mahn11].

3.2.1. VB-PES and IPES Study on the M-O Interface and the Impact of O_2 on the Electronic Properties

In this section the energy level alignment between MnPc and a polycrystalline Co substrate is determined by the combination of VB-PES and IPES measurements. The evolution of the transport band gap of MnPc films is presented as a function of the film thickness and the subsequent air exposure. Co was chosen as a substrate due to its attractiveness for organic spintronics applications provided by its high spin polarisation properties [Barr10, Djeg13].

The occupied electronic states of MnPc were intensively studied by VB-PES [Grob09, Grob10, Grob11]. The unoccupied electronic states of MnPc were previously determined by IPES by Yoshida *et al.* [Yosh01]. The latter study concentrated on the 3d levels of the central metal ion for different TMPcs and a detailed comparison with unoccupied electronic levels determined by Near Edge X-ray Absorption Fine Structure was presented [Koch85]. The data regarding the transport gap of MnPc presented in this section was recently published in ref. [Haid13A].

Recent spin polarised VB-PES and IPES measurements on MnPc deposited on Co(001) reveal a high interface spin polarisation at room temperature [Djeg13]. It is a purely ligand related interface phenomenon concentrated at the first monolayer of organic molecules [Atod10]. Focusing on possible applications for electronic and spintronic devices this study concentrates on the electronic and optical properties of MnPc films with thicknesses in the nanometre range.

Figure 3.2.1 shows the evolution of the valence band photoemission and inverse photoemission spectra with increasing film thickness. According to the explanations from section 2.2.2 the following quantities were determined: Φ, Δ, IE, EA, and E_t. For exact determination of the HOMO and LUMO onsets both valence band and inverse photoemission spectra were fitted with Gaussian shaped peaks and cubic polynomial backgrounds. Unlike for CuPc the HOMO region is defined by two peaks: the large one having a pure ligand nature, and the smaller one closer to the Fermi level having Mn 3d character [Grob11]. The LUMO feature was fitted by a single peak. It is broader due to the larger influence of the experimental broadening of approximately 0.5 eV and was deconvoluted in order to reduce the influence of the instrumental broadening.
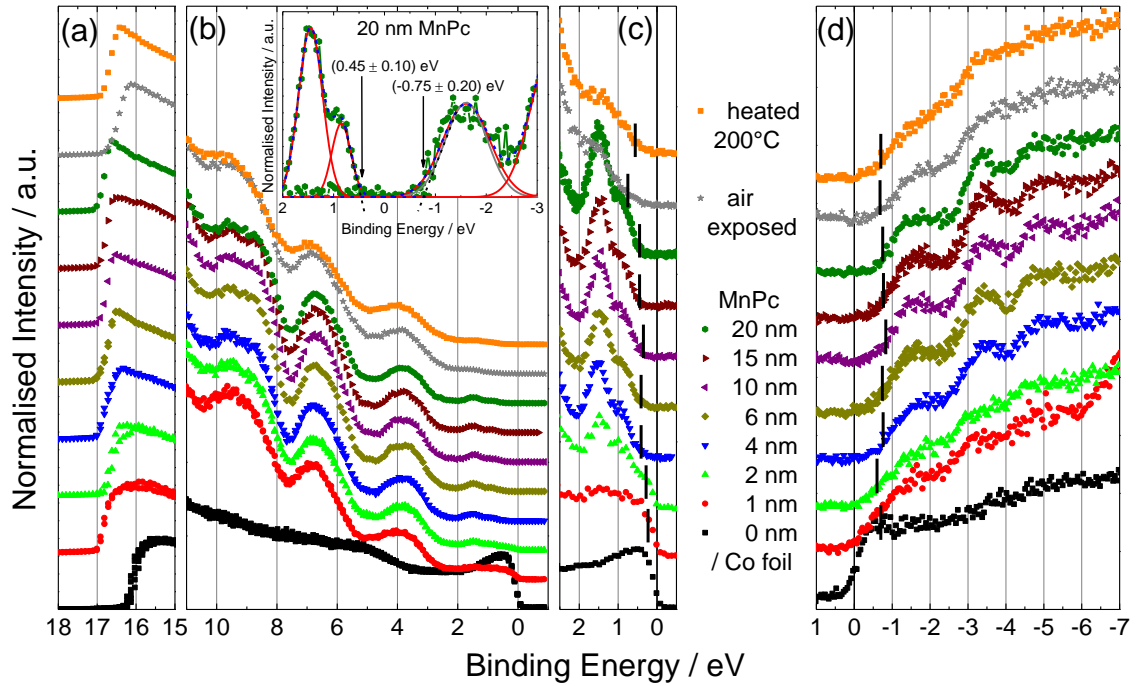
Figure 3.2.1. Valence band (a, b, c) and inverse (d) photoemission spectra of MnPc film at different thicknesses deposited onto Co foil. The spectra are normalised and a vertical offset is introduced for clarity. Valence band photoemission spectra: secondary electron cut-off (a), an overview of the valence band region (b), and the HOMO region (c). The inset exemplifies the HOMO and LUMO onset determination. The HOMO and LUMO onsets are marked by vertical bars for each spectrum (c, d).

The inset of Figure 3.2.1(b) exemplifies the onset determination for the spectra of a 20 nm thick film with subtracted backgrounds. The determined onset positions are marked in Figure 3.2.1(c) and (d) by vertical bars. For very thin films of 1 nm and 2 nm the influence of the Co substrate signal at the Fermi level is visible. This was as well accordingly subtracted.

Due to image charge potential contributions at the metal-organic semiconductor contact in the nanometre range a reduction of the barrier height is expected [Tsip02, Scot03, Knup05, Flor09, Barr10]. This was clearly evidenced for CuPc in section 3.1.1. Here, the resulting opening of the transport band gap for MnPc within the first 4 nm of film thickness was observed. The HOMO and LUMO shift away from the Fermi level by 0.20 eV and 0.15 eV, respectively (see *e.g.* Figure 3.2.2(c)).

At the MnPc/Co interface a constant interface dipole $\Delta = (-0.7 \pm 0.1)\,eV$ is observed indicating charge transfer between the MnPc molecules and the metallic substrate, as already observed in the case of MnPc/Au [Petr12]. This behaviour is different from what was observed for *e.g.* CuPc deposited on a semiconducting

substrate, namely hydrogen passivated Si (H-Si) [Gorg05]. There, a band bending type of behaviour for HOMO and LUMO positions was found at the inorganic semiconductor-organic semiconductor interface with Δ decreasing slowly with increasing film thickness [Gorg05].

The electronic properties of the thickest MnPc film investigated here (20 nm) are summarized in Figure 3.2.2(c) as an energy band diagram. These values represent the bulk-like MnPc not affected by the substrate any more. The much smaller transport gap of MnPc (1.2 ± 0.3) eV compared to CuPc (2.2 ± 0.3) eV is the result of additional electronic levels close to the Fermi level [Grob11]. The presence of these states with metallic 3d contribution having e_g symmetry is supported by density functional theory (DFT) calculations [Grob11, Frie12].

It is well known that MnPc is reactive in air [Cook09, Frie12]. Here the impact of air exposure (time = 1 h) on the MnPc electronic structure was investigated by performing VB-PES and IPES measurements. In order to test the reversibility of the oxidation process the sample was re-measured after annealing it in vacuum for 10 minutes at 200 °C.

The corresponding spectra are plotted in Figure 3.2.1 in full range and in Figure 3.2.2(a) and (b) in a smaller energy range together with the fitted peaks. As a general trend, all peaks decrease in intensity and become broader upon air exposure. In particular, the low energy feature at 0.9 eV in the valence band spectrum disappears almost completely and shifts towards higher energies. As discussed above, this $1e_g$ state stems from the 3d-orbitals of the Mn central ion [Grob11]. The peak at 1.5 eV having π nature [Grob11] does not shift. Even though the peaks related to unoccupied states also weaken upon air exposure, they are still well visible and have an onset very close to the one prior to air exposure.

These observations provide clear evidence for the hypothesis that the oxygen molecule attaches to the metal centre of the MnPc molecule and thus the uppermost occupied 3d states of the Mn ion are affected by this oxygen attachment. This is in good agreement with theoretical results of DFT calculations, which predict a MnPc-O_2 complex formation with a small binding energy of only 0.5 eV [Frie12]. The broadening of the peaks might be related to the appearance of additional occupied and unoccupied states related to the MnPc-O_2 complex [Frie12], as well as by a distortion of the molecular geometry during the oxygen diffusion into the MnPc film.
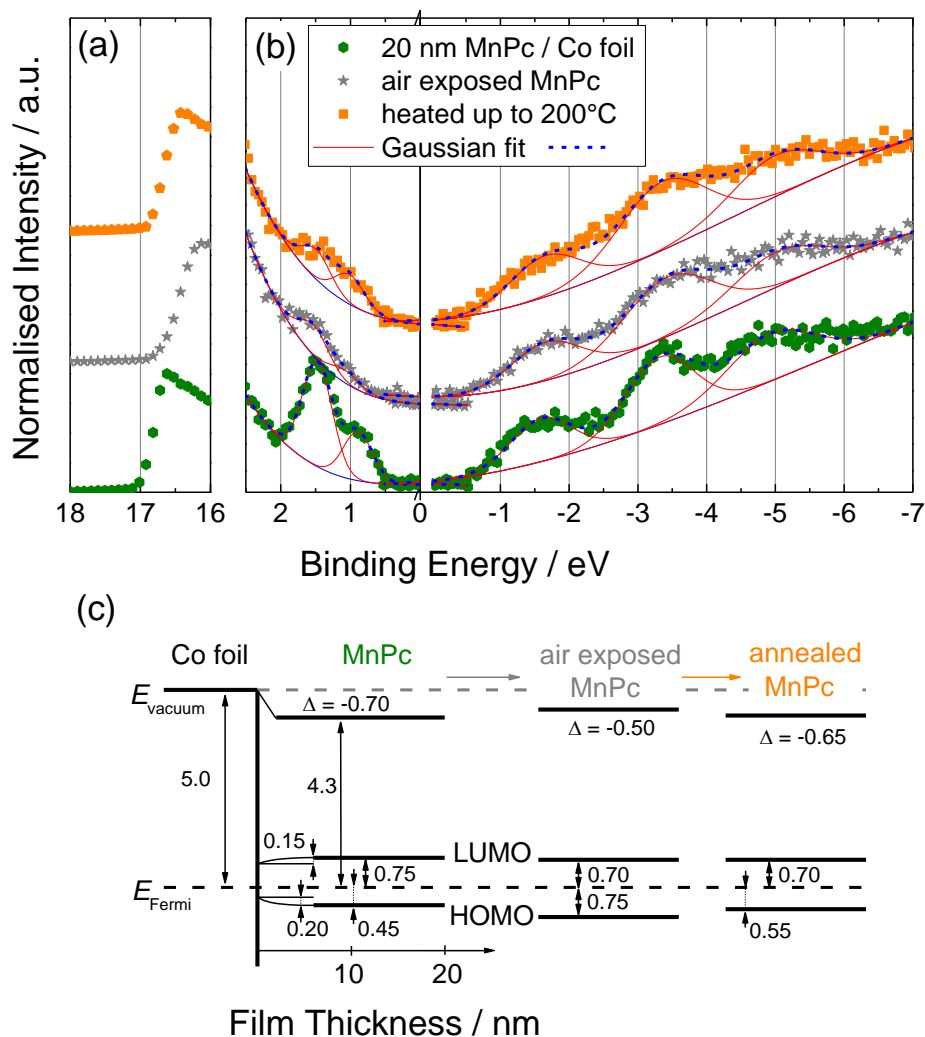
Figure 3.2.2. (a) The secondary electron cut-off region of the valence band photoemission spectra of a pristine, air exposed, and annealed MnPc (20 nm) film. (b) Fitted valence band and inverse photoemission spectra for the same sample. (c) Thickness dependent energy band diagram of the MnPc/Co interface and the evolution of the energy levels after air exposure and heating.

In addition, upon air exposure the interface dipole was lowered and the HOMO onset position increased by 0.2 eV. The valence band photoemission spectrum of the sample annealed at 200 °C for 10 min shows a recovery of the low lying peak denoting desorption of the oxidising agent. It does, however, not have the same shape as the one of the pristine material probably due to a morphology change upon annealing [Kozl12]. In a second annealing step at 270 °C the molecules completely desorbed from the substrate. The O_2 desorption temperature might be very close to the sublimation temperature of MnPc molecules from thin layers. The challenge to reversibly desorb the oxygen was tackled by *in situ* SE measurements as well in section 3.2.3.

3.2.2. Impact of K Doping on the Electronic Properties

Identifying the changes of the electronic properties of TMPc molecules upon alkali metal intercalation is a hot topic nowadays and plenty of VB-PES, CL-PES, and XAS data on different systems already exists. MnPc, however, was not yet fully investigated leaving many questions still open. Thus, this section is dedicated to study the impact of K intercalation on the electronic properties of MnPc thin films. Since it is the most extensive section for clarity it is divided into 4 subsections focused on the VB-PES and IPES, CL-PES, and NEXAFS studies and finally on the film morphology.

3.2.2.1. VB-PES and IPES Measurements

The impact of K intercalation on the occupied and unoccupied electronic states of MnPc was studied by combined Valence Band Photoemission Spectroscopy and Inverse Photoemission Spectroscopy. On a clean Co foil 10 nm MnPc was sublimed which was consecutively intercalated with K. The spectra were recorded after each doping procedure.

Figure 3.2.3 presents VB-PES and IPES measurements on the substrate, the MnPc film, and the K intercalated layer as a function of K concentration. The amount of potassium (K atoms per MnPc molecules) was determined by using of the calibration curve from section 2.2.5. The error in determining the K quantity is 15 % and is not written in the legend. The HOMO and the LUMO regions of the spectra (Figure 3.2.3(c) and (d)) were fitted according to the description of section 2.2.2. The features in the LUMO region were deconvoluted by employing equation (15) and outlined with grey dashed lines in Figure 3.2.3(d).

Furthermore, the onset positions of HOMO (H), HOMO-1 (H-1), LUMO (L), and LUMO+1 (L+1) were assigned in Figure 3.2.3. With increasing amount of K the LUMO is filling up with electrons and appears as an additional filled state ascribed by L' in the valence band region. At the same time the intensity of the LUMO decreases until it fully disappears for high K dosage.

The onset energy positions of the above quantities are given in Figure 3.2.4(a) with regard to the Fermi level (E_F). Up to the K concentration of 0.9 the HOMO has an apparent shift towards E_F due to the missing L' extra peak in the fitting procedure.
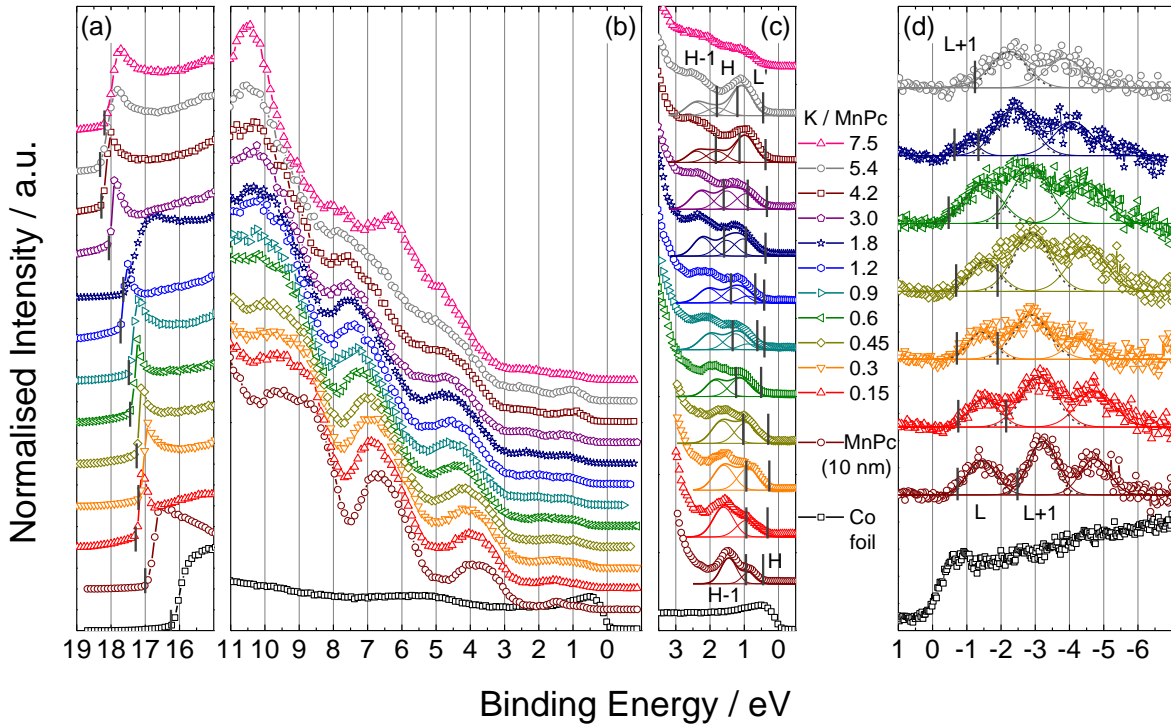
Figure 3.2.3. Evolution of the valence band (a, b, c) and inverse (d) photoemission spectra of K intercalated MnPc deposited on Co foil. The valence band photoemission spectra are divided in three regions: secondary electron cut-off (a), overview of the valence band (b), and the HOMO region (c). The inverse photoemission spectra, except for the Co foil, are background subtracted (d). The cut-off positions and the onset positions of the HOMO (H), HOMO-1 (H-1), filled LUMO state (L'), LUMO (L), and LUMO+1 (L+1) are marked with vertical bars.

However, the rest of the values all shift towards higher BE with as much as 1.0 eV. The exceptions are the LUMO and L' which do not cross E_F. Due to this pinning down the molecules do not present metallic properties from the electronic point of view and remain semiconducting [Garg10]. It was, however, previously shown by electrical measurements that the conduction increases dramatically by doping [Crac05].

Thus, to get a feeling on the amount the energy bands shift an energy level diagram was plotted in Figure 3.2.4(b) for the pristine MnPc and the fully doped one (K / MnPc = 5.4). Although, a rigid shift of all the bands is expected [Ding09], there are small differences to be observed between the shifts of occupied and unoccupied states. While H and H-1 position change by ~0.8 eV the L+1 on the other hand has a shift of 1.2 eV. This might be a result of the fitting procedure, however in the following section (3.2.2.2) will be shown that the core levels have an even less shift with the amount of K (Figure 3.2.6).
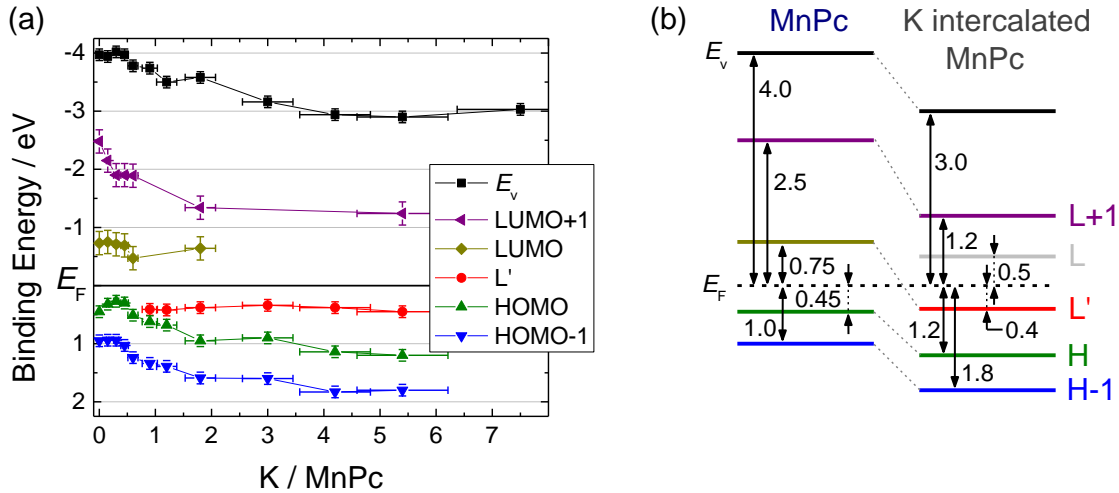
Figure 3.2.4. (a) The onset positions of the quantities determined in Figure 3.2.3 as a function of the amount of K per MnPc molecule. The vacuum level (E_v) is determined instead of the cut-off position. (b) Energy level diagram of the occupied and unoccupied electronic states of MnPc before and after K intercalation.

It is worth mentioning that VB-PES and IPES data analysis is not strait forward due to the smearing out of the features with alkali metal doping. It also broadens the features, especially in the IPES part, as was observed also by other authors [Schw03, Ding09]. However, by fitting the data the evolution of the features can be well pursued as presented in Figure 3.2.3(c) and (d). Moreover, the evolution of the VB part of the spectrum is studied by higher excitation energy (150 eV) as well (see *e.g.* Figure 3.2.7). There the 3d hybrid states are more pronounced than the ligand related feature due to larger cross section. The shifts of the feature onsets in the VB region acquired at 150 eV excitation energy reproduce well the ones presented above.

3.2.2.2. CL-PES Measurements

Core level spectra of K intercalated MnPc(10 nm)/Co films were recorded and evaluated. The excitation energies were selected according to Table 2.1 aiming to maximise the cross section of the analysed species. In Figure 3.2.5 the spectra are shown with increasing amount of K from top to bottom.

The data analysis is presented starting with the high energy peaks, *i.e.* Mn $2p_{3/2}$ and Mn $2p_{1/2}$. The doublet peaks were coupled together during the fit, although for clarity only the $2p_{3/2}$ peaks are presented in detail in Figure 3.2.5(a). According to
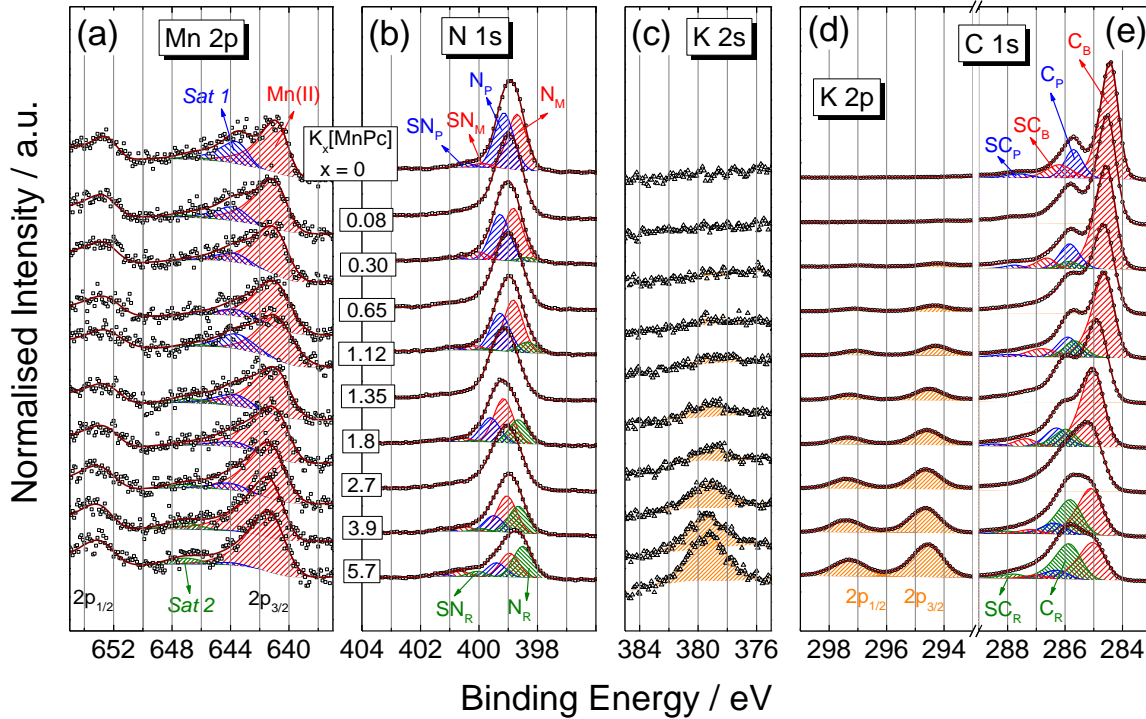
Figure 3.2.5. MnPc core level spectra function of K intercalation. Fitted spectra of Mn 2p$_{3/2}$ (a), N 1s (b), K 2s (c), K 2p (d), and C 1s (e). The amount of K increases from top to bottom as indicated in between panels (a) and (b) and holds for each core level spectrum. For clarity every second N 1s and C 1s core level spectrum is plotted without the fitted component features.

literature the manganese central ion is assigned to the oxidation state Mn^{2+} [Petr12], which is plotted with the red hatched feature in the Mn 2p fitted spectra and assigned as Mn(II). In the pristine form the Mn(II) peak has a shoulder at higher BE plotted with blue hatched area and designated as *Sat 1* in the figure. This extra (satellite) feature is a consequence of the multiplet effect [Krol12]. The main electronic configuration of MnPc in the ground state is still not yet well understood. Kroll *et al.* [Krol12] pointed out the equal possibility of two configurations: $b_{1g}^0 a_{1g}^1 e_g^3 b_{2g}^1$ and $b_{1g}^0 a_{1g}^1 e_g^2 b_{2g}^2$, where b_{1g}, a_{1g}, e_g, and b_{2g} represent the 3d shell orbitals with increasing BE in this order. The superscripts in the configurations represent the number of electrons. Recently Stepanow *et al.* [Step14] pointed out the sole configuration of $b_{1g}^0 a_{1g}^1 e_g^2 b_{2g}^2$ while Brumboiu *et al.* [Brum14] determined the $b_{1g}^0 a_{1g}^1 e_g^3 b_{2g}^1$ configuration as the ground state electron configuration.

As the amount of K increases the *Sat 1* peak decreases in intensity and has an insignificant contribution above 1.8 K atoms per molecule. This means that the ground state electron configuration of the pristine state changes and accommodates donated electrons upon K intercalation. The multiplet splitting has an even larger effect on the

Mn *L edge* NEXAFS spectral shape, presented in the following section (3.2.2.3). A third feature at 6 eV higher BE given by the green hatched area was assigned to a further satellite (*Sat 2*) better visible for the fully doped sample. The assignment of the Mn $2p_{3/2}$ features was done according to the references [Nesb98, Bies11, Krol12].

Further, the N 1s data is shown in Figure 3.2.5(b) for pristine and K intercalated MnPc. For clarity, the components of each second spectrum are not shown. Alike for CuPc (section 3.1.2) the pristine material presents two main features N_M and N_P plotted with red and blue hatched areas, respectively. The shake-up satellites of these main features were assigned as SN_M and SN_P, respectively. It should be mentioned that for both CuPc and MnPc the N 1s core level can be fitted with a single main peak as the spectral resolution is smaller than the split-up of the N_M and N_P peaks. However, fitting the data with two features makes it possible to further analyse the spectra after K intercalation, where by the influence of K^+ ions on the N_P feature (nitrogen atoms bridging the pyrrole rings, *e.g.* see Figure 3.1.3(d)), it decreases in intensity and an extra one assigned as N_R (green hatched area) rises at lower energy (please note, SN_R represents the shake-up satellite of N_R). As the intensity of N_R is even larger than N_M for the fully doped MnPc film, it can be deduced that also N_M atoms are affected by the K^+ ions. Thus, although K atoms preferentially occupy positions between the benzene rings (close to N_P) [Aris10], at a certain K concentration (K / MnPc > 1.8) positions closer to the metal centre start to be occupied.

In Figure 3.2.5(c) the K 2s peak evolution is given. However, due to the small cross-section the features are very broad and lack the intensity. Thus, the K 2p spectra (Figure 3.2.5(d)) were further analysed. These were fitted with a doublet for the $2p_{3/2}$ and $2p_{1/2}$ components.

Finally, the components of C 1s are presented in Figure 3.2.5(e). Again, alike CuPc, pristine MnPc shows two main features C_B and C_P given by hatched red and blue areas, respectively. Their shake-up satellites are ascribed by SC_B and SC_P. The C_B and C_P peaks originate from C atoms of the benzene and pyrrole rings, respectively. An extra peak designated as C_R (with its shake-up satellite SC_R) and depicted in the figure with green hatched area arises due to K^+ ion influence. Its energetic position is situated between C_B and C_P and is composed of both benzene and pyrrole C atoms affected by K.

The shake-up satellites of N 1s and C 1s core levels for pristine MnPc are at ~1.25 eV and ~1.8 eV higher BEs than the main peaks. The C 1s related satellite main
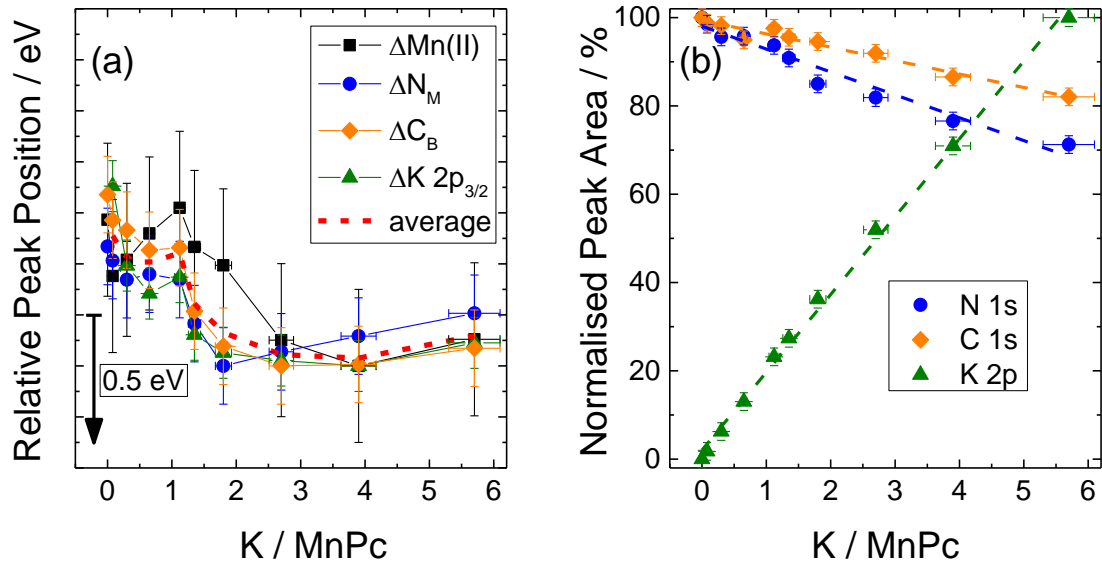
Figure 3.2.6. (a) Core level peak shift as a function of K amount. The relative shifts for Mn(II) $2p_{3/2}$, N_M 1s, C_B 1s, and K $2p_{3/2}$ are according to Figure 3.2.5. The red dashed line represents the average of these peak positions. (b) Normalised N 1s, C 1s, and K 2p peak areas as a function of K amount. The largest area of each species was employed as normalisation factor. The dashed lines represent the linear fit of the data points.

peak splitting of MnPc has a close value to the one of CuPc (between 1.7 eV and 2.0 eV), however the N 1s related satellite main peak splitting of MnPc is much smaller than for CuPc (1.8 eV), for the comparison see *e.g.* Figure 3.1.4(b). Moreover, the N 1s related shake-up satellite relative position with regard to the main peak (~1.25 eV) can be directly related with the transport band gap of MnPc (1.2 ± 0.3) eV determined by combined VB-PES and IPES. This is in very good agreement with the fact that the HOMO is composed of hybridised Mn 3d orbitals with the surrounding N ligand orbitals [Grob11]. On the other hand the C 1s shake-up satellites are rather related to the HOMO-1 ligand π nature electronic state, thus they present a larger splitting from the main feature (~1.8 eV). The origin of the shake-up satellites was discussed in more detail in section 3.1.2.

Another effect of donated electrons is the shift of the Fermi level towards the vacuum level and thus also of all the core levels towards higher energetic positions. In Figure 3.2.6(a) the relative shifts of the main core levels are plotted against the amount of K in the molecular layer. The energy scale is flipped over for comparison with the energy level diagram (Figure 3.2.4(b)). The magnitude of the shifts is related to the arrow in the plot which represents 0.5 eV. An average of the shifts is given by the red dashed line. A small shift for K / MnPc < 1 can be deduced, while for K / MnPc > 1 a

larger one is observed with saturation above K / MnPc = 4. The total shift is less than 0.5 eV, thus half the value determined for the HOMO-LUMO region (~1.0 eV, see *e.g.* section 3.2.2.1).

Figure 3.2.6(b) depicts the N 1s, C 1s, and K 2p normalised peak areas as a function of the K amount. The fitted spectra from Figure 3.2.5 was employed for data evaluation. For each determined area all the components were taken into consideration, *i.e.* N 1s: N_M, N_P, N_R, SN_M, SN_P, and SN_R; C 1s: C_B, C_P, C_R, SC_B, SC_P, and SC_R; K 2p: $2p_{3/2}$ and $2p_{1/2}$ (see *e.g.* Figure 3.2.5). The areas were normalised to their largest value and quantified in % in Figure 3.2.6(b). The dashed lines represent the linear fittings. First, it can be said that the area of K 2p increases linearly by the K amount, while the N 1s and C 1s areas decrease. For the fully doped sample (K / MnPc = 5.7) N 1s and C 1s areas decrease to 71 % and 82 %, respectively. The discrepancy of the two values might be due to specific localisation of the K atoms on the MnPc molecule closer to the N atoms and shielding their CL-PES signal. To be noted that the areas of C 1s and K 2p were employed for the K amount determination from section 2.2.5 by taking into consideration the absolute areas and the respective cross sections (see *e.g.* equation (19) and Table 2.1).

Additionally, more information on the d-states can be gathered by performing VB-PES measurements with higher excitation energy [Grob09]. In Figure 3.2.7(a) the evolution of the VB by increasing the amount of K is presented. The excitation energy was 150 eV. To be comparable with Figure 3.2.3 the evolution starts from the bottom spectrum towards the upper one. The features denoted by H-1, H, and L' represent the HOMO-1, HOMO, and filled LUMO states, respectively. They present similar behaviour as in the VB-PES experiments in the previous section (3.2.2.1). The additional feature assigned as A in the figure arises at small amounts of K (0.65) and fades away above 1.8 K atoms per MnPc. Figure 3.2.7(b) illustrates the zoom in of the HOMO region with additional overlapping spectra from Figure 3.2.3 represented by symbols. Only the spectra with similar quantities of intercalated K atoms is shown. By comparing the spectra at the two excitation lines (150 eV → solid lines   and   21.2 eV → symbols) the first observation can be made for the pristine MnPc film. The HOMO peak with higher excitation energy is more pronounced than at low photon energy due to its hybrid 3d character which has higher cross section for the 150 eV excitation [Grob09]. The second observation is with regard to the feature A which is not present in the low
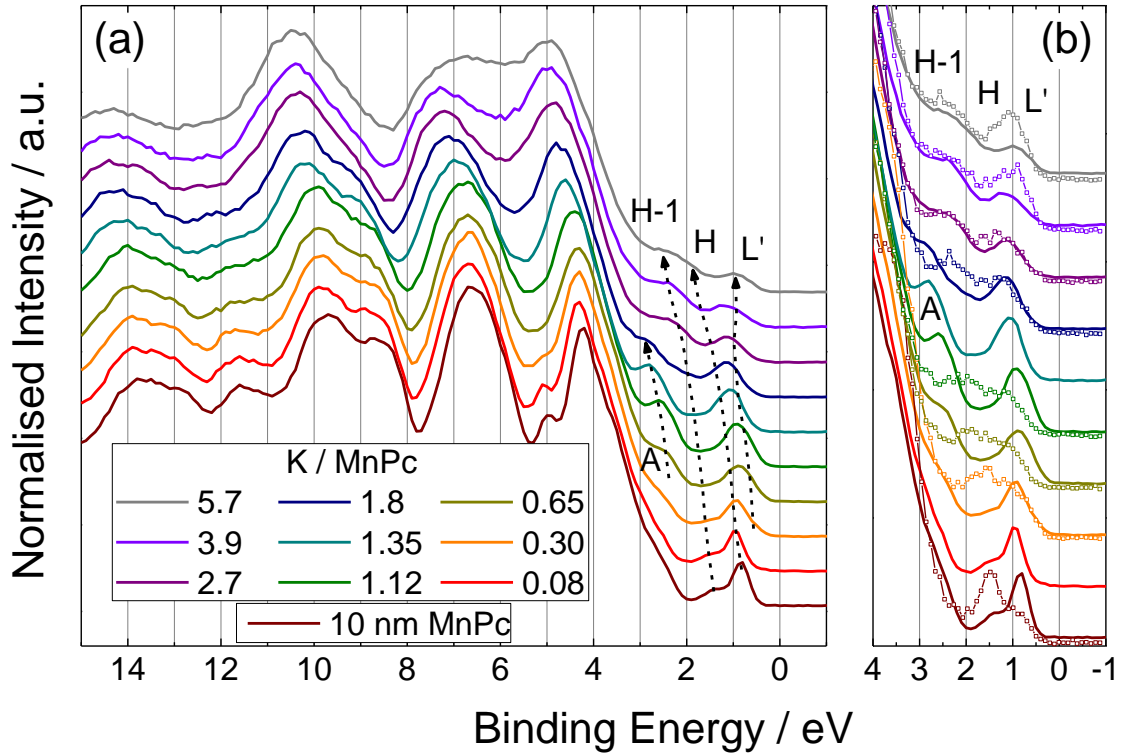
Figure 3.2.7. (a) Valence band spectra evolution as a function of the amount of intercalated K. The excitation energy of the photons was 150 eV. The features H-1, H, and L' represent the HOMO-1, HOMO, and filled LUMO states. The dashed arrows mark the evolution of the peak positions. (b) Zoom in of the HOMO region. The spectra with symbols are VB-PES measurements from Figure 3.2.3 where the He II excitation line was employed (21.2 eV).

excitation energy spectra, thus it is assigned to another Mn 3d related state at higher binding energy (~2.5 eV). This assumption is sustained by theoretical calculations by Brumboiu *et al.* [Brum14] who showed that different ground state electron occupation of the Mn 3d states provide different symmetry of the HOMO and different bond lengths in the MnPc molecular structure. According to them the most stable ground state configuration in thin MnPc films is $b_{1g}^0 a_{1g}^1 e_g^3 b_{2g}^1$ which does not have the additional A feature. However, the calculated electron configuration of $b_{1g}^0 a_{1g}^1 e_g^2 b_{2g}^2$ has a feature exactly at the energy position of peak A which implies that upon K intercalation the electronic configuration, molecular structure, and symmetry of the MnPc molecule is modified. The fade out of the feature above 1.8 K per MnPc might be related to the changes in the orbital configuration induced by doping. More information is provided by the NEXAFS measurements in the following section (3.2.2.3).

3.2.2.3. NEXAFS Measurements

NEXAFS measurements at the manganese *L*, nitrogen *K*, and carbon *K edges* were performed on K intercalated MnPc films. The spectra were recorded at normal ($\theta = 90°$) and grazing ($\theta = 20°$) incidence. Since XAS indirectly provides information on the local unoccupied electronic states [Simo13] the NEXAFS data were used for this analysis.

Figure 3.2.8 illustrates the evolution of Mn L_2 (higher energy) and L_3 (lower energy) *edges* as a function of the amount of K. The two edges stem from transitions from Mn $2p_{3/2}$ (L_3) and $2p_{1/2}$ (L_2) core levels onto unoccupied Mn 3d states, or in the case of MnPc hybridised d-states [Petr11]. In the panel (a) of the figure the spectra are given for incidence angles of 90° (solid lines) and 20° (dashed lines). Since there are no significant differences in line shape or intensity between the spectra at the two angles the attention will be focused on the evolution via K doping only at 20°.

The *L$_3$ edge* evolution at grazing incidence is presented in Figure 3.2.8(b). For pristine MnPc three features are visible denoted by A, B, and C. Up to 1.35 K atoms per molecule no significant changes are noticeable except of some slight shifts which can be correlated with the ones seen for the Mn 2p core levels as well (Figure 3.2.6). However, above this threshold the L_3 absorption features undergo huge changes. Since the evolution of features A, B, and C cannot be followed anymore the newly appeared features are noted as D, E, and F. These undergo shifts by 0.5 eV towards lower energies which are again correlated with the ones of the Mn 2p levels. The striking development, however, is the rise of these peaks, especially the first feature D. The L_2 edge (Figure 3.2.8(a)), on the other hand, remains almost constant in intensity only the spectral weight for the fully doped MnPc ($K_{5.7}$[MnPc]) is set on the first two features. These are more imposing as for the pristine material while the third feature fully disappeared.

The theoretical interpretation of the *L absorption edge* is rather complicated due to initial $3d^N$ and final $2p^5 3d^{N+1}$ states to which all the partially empty levels in the atom contribute. Moreover, the hybridisation of Mn 3d states with N 2p states contribute to this difficulty. However, theoretical calculations are available in literature, but often with contradictory results (see *e.g.* literature within [Petr11, Petr12]). Additionally, multi-electron effects further complicate the XA spectra analysis [Simo13, Krol12].

Without theoretical support a naive interpretation of the spectra ca be done by comparing the line shape with XAS data of different inorganic Mn compounds [Garv94, Gilb03]. The *L edge* of the fully doped $K_{5.7}$[MnPc] film is similar to spectra of Mn^{2+} compounds (*e.g.* MnO [Gilb03], MnF_2 [Garv94]). Furthermore, these complexes have five unpaired electrons and thus a high-spin state of S = 5/2. The line shape of pristine MnPc, on the other hand, cannot be assessed with a certain oxidation state, but instead with a superposition of more spectra distinct from Mn^{2+} [Garv94, Gilb03]. XAS spectra of inorganic Mn compounds [Mitr03, Kata10] suggest a superposition of Mn^{3+}, Mn^{4+},
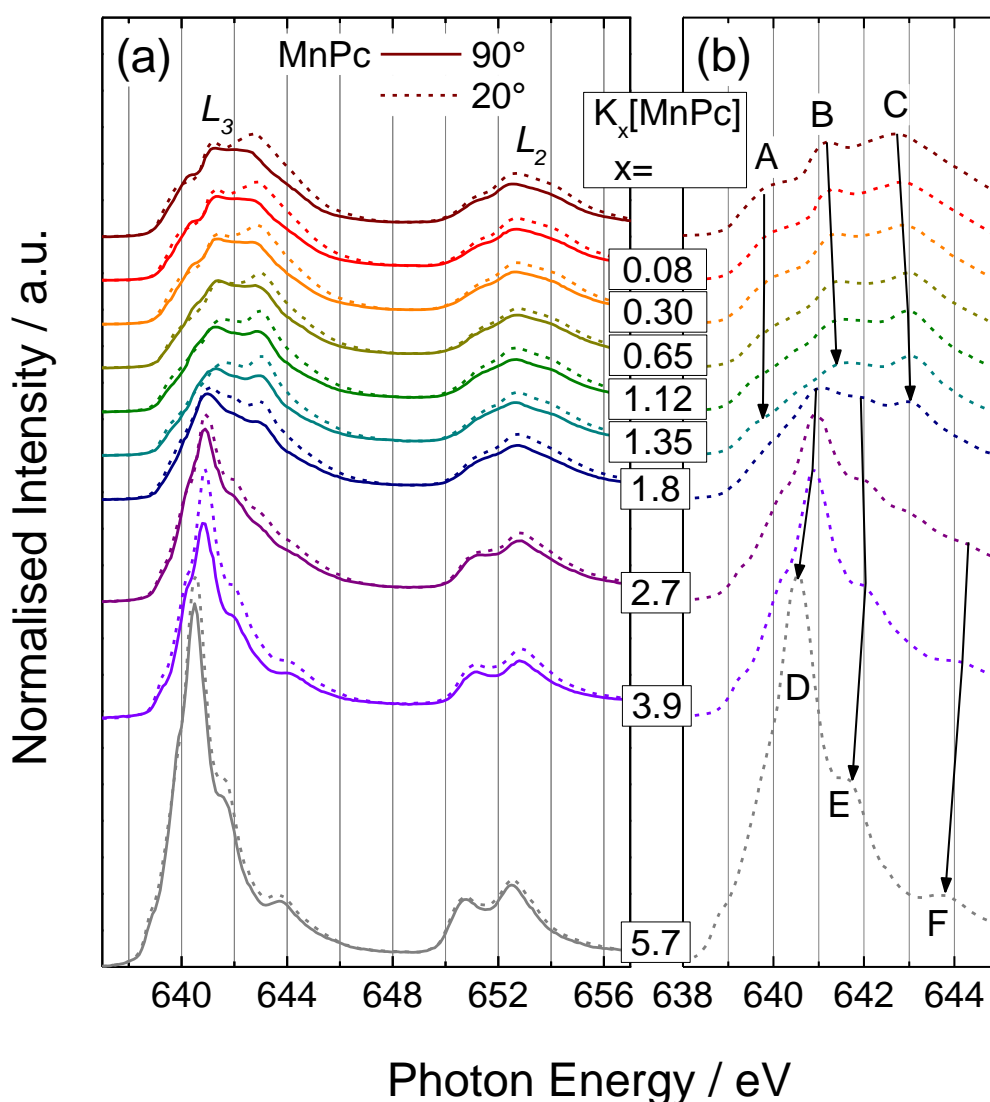
Figure 3.2.8. (a) Mn L_2 and L_3 *edges* as a function of K amount per MnPc molecule at normal incidence (solid lines) and at grazing incidence (dashed lines). (b) Highlighted Mn L_3 *edge* for the 20° incidence angle. The arrows track the evolution of the peak positions (A, B, and C, followed by D, E, and F). The spectral evolution is plotted from top to bottom with the K amount specified in between the panels.

and less Mn^{2+} ionic behaviour of the MnPc film. However, the electronic structure of the molecule is way different than for the previously mentioned inorganic compounds, thus a direct comparison of the spectral line shape does not provide enough information. Moreover, due to different final state effects, *e.g.* multiplet splitting [Krol12], the XA line shapes are highly influenced.

Important information can be gathered from the branching ratio (BR) of the L_2 and L_3 core-valence transitions [vdLa88, Thol88, Kosh00]. BR is defined as: $BR = \frac{A(L_3)}{A(L_2)+A(L_3)}$, where $A(L_x)$ represents the area of the respective *L edge* feature [Kosh00]. Thus, the BR for pristine MnPc and fully doped $K_{5.7}$[MnPc] was determined to be 0.68 ± 0.03 and 0.79 ± 0.03, respectively. Similar value for the pristine phase was determined by Koshino *et al.* [Kosh00] and attributed to an intermediate-spin state. Thus, MnPc in pristine form has the spin S = 3/2 [Frie12]. Taguchi *et al.* determined a spin state of S = 5/2 for fully doped MnPc [Tagu06]. In this study from the increase of the BR an increase of the spin state can be revealed, however, no quantitative information can be specified.

In the second set of NEXAFS spectra the evolution of N *K edge* was recorded during the K intercalation of MnPc. In Figure 3.2.9(a) the full spectra (both $N\,1s \rightarrow \pi^*$ and $N\,1s \rightarrow \sigma^*$ transitions) are plotted and in the panel (b) a zoom in of the $N\,1s \rightarrow \pi^*$ transitions is presented. The spectra for normal incidence ($\theta = 90°$) are plotted. For the analysis of the spectral development the Figure 3.2.9(b) is considered for discussions. Starting with the pristine MnPc the evolution of four features (labelled A, B, C, and F) can be followed. Up to the K concentration of 1.8 the peaks A and B are unchanged, while C and F shift slightly towards lower energy. Above K / MnPc = 1.8 the feature F can be further followed with a total shift of 0.5 eV. However, A, B, and C vanish and for the fully doped film the new features D and E arise (see *e.g.* Figure 3.2.9(b)). To better understand the origin of the features the data was compared with the literature.

First, the case of K intercalated metal free phthalocyanine (H_2Pc) [Nils12] illustrates only three features for the $N\,1s \rightarrow \pi^*$ transitions. These are attributed to the total LUMO of the molecule and comprise only 1/4th of it, the rest being attributed to C 2p antibonding states. Furthermore, the N *K edge* of CuPc is also composed of only three features [Molo08B, Molo08A] which suggest that the main contribution is given by the same π^* empty states located around the pyrrole ring and composed of both

N 2p and C 2p states. One can even overlap the N and C *K edges* with relatively good agreement [Molo08B]. By K intercalation in CuPc nothing spectacular was observed, just the usual downward shift of the features [Molo08A]. However, on the other hand FePc [Aris10], CoPc [Petr11], and MnPc [Petr11, Petr12] present four distinct features, similar to the results of this work. It is argued that the first two features (A and B from Figure 3.2.9(b)) belong to transitions from the two distinct nitrogen core levels (N_M and N_P in Figure 3.2.5(b)) onto the same low lying empty π^* state [Aris10]. The second argument is that the first features have significant contribution from the central metal ion, thus a hybridisation occurs between N 2p and Mn 3d states [Petr11, Petr12]. According to the results from this work the second argument can be strongly supported. The strong influence of Mn 3d on the N *K edge* can even be observed by correlating it with the evolution of Mn *L edges* (Figure 3.2.8). Thus, it can be said that for MnPc the empty states are composed on some extent of hybrid 3d orbitals [Grob11] which are highly influenced by electron donation from the intercalated K atoms.

Further information can be extracted from the spectral evolution of Figure 3.2.9(b). While the features A, B, and C survive up to the net doping of 1.8 (almost $K_2[MnPc]$) and the rising features D and E are clearly distinguishable above a net
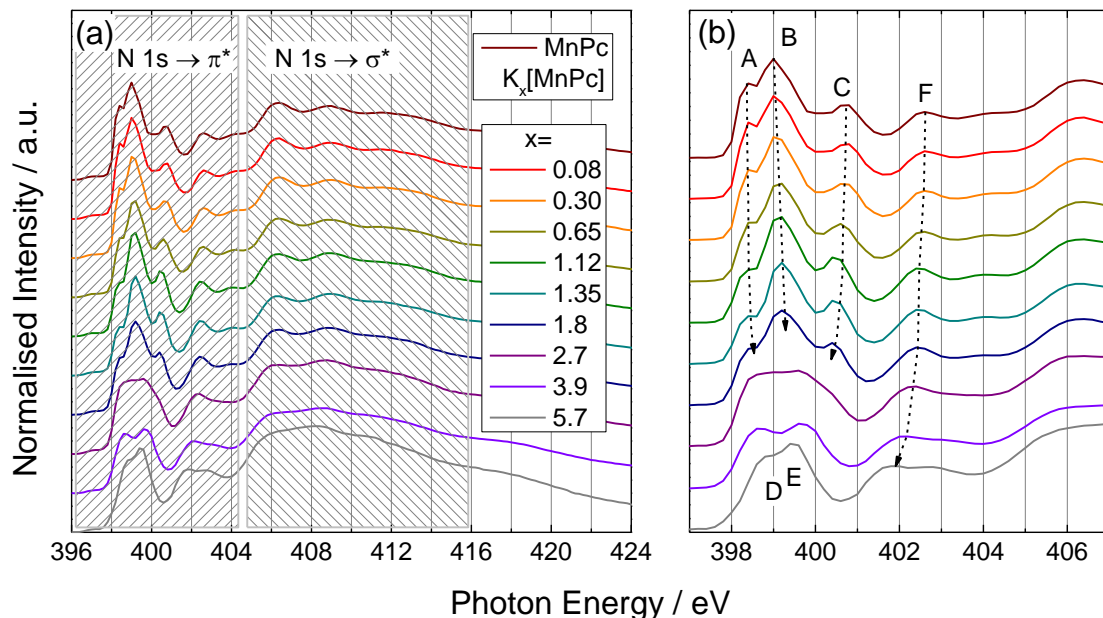
Figure 3.2.9. (a) Nitrogen *K edge* evolution as a function of the potassium amount per MnPc molecule. The $N\,1s \to \pi^*$ and $N\,1s \to \sigma^*$ transitions regions are marked by the hatched areas. (b) Focus on the region with the $N\,1s \to \pi^*$ transitions. The dashed arrows follow the evolution of the features labelled A, B, C, and F.

charge of 3.9 (thus $K_4[MnPc]$) there is no specific spectrum in between, but a linear combination of the two. Thus, the existence of the doped phases $K_2[MnPc]$ and $K_4[MnPc]$ can be deduced while a phase with 3 K atoms is missing, which is in good agreement with literature findings [Mahn11].

The third set of NEXAFS spectra is composed of the evolution of the C *K edge* of MnPc via K doping. In Figure 3.2.10(a) the full spectral range is presented. In the energy region from 296 eV to 302 eV the increase of the K 2p contribution is present. A zoom in on the $C\,1s \rightarrow \pi^*$ transition region is shown in panel (b). Four distinct features are present for the pristine material: A', A, B, and C. Contrary to the N *K edge* the four features are present for H_2Pc [Nils12] and CuPc [Molo08B, Molo08A] as well as for FePc [Aris10] or CoPc [Aris11]. Furthermore, a full agreement on the assignment of the first two peaks (A' and A) is provided in literature [Molo08A, Molo08B, Aris10, Aris11, Nils12]. Features A' and A are caused by excitation from benzene (C_B) and pyrrole (C_P) carbon atoms, respectively, into the LUMO. The energy difference between A' and A matches exactly with the one between C_B and C_P in Figure 3.2.5(e).
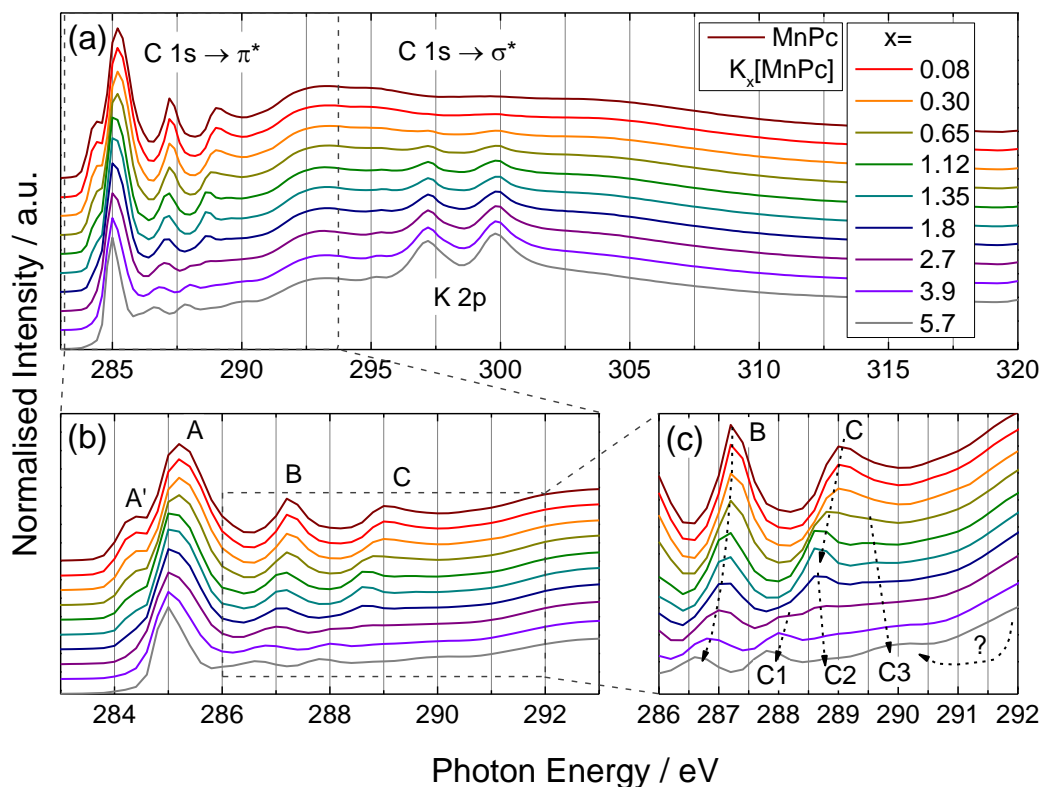
Figure 3.2.10. (a) Carbon *K edge* evolution as a function of potassium amount per MnPc molecule. The regions of $C\,1s \rightarrow \pi^*$ and $C\,1s \rightarrow \sigma^*$ transitions are defined in Figure 2.2.5(a). (b) Zoom in on the $C\,1s \rightarrow \pi^*$ transitions region. (c) Additional focus on the B and C peak evolution. The dashed arrows follow the features evolution. The dashed rectangles mark the emphasised regions.

As a result of K intercalation feature A slightly shifts towards lower energies and decreases in intensity while feature A' decreases and fully disappears above a K concentration of 1.8. The disappearance of A' is attributed to the filling of the LUMO with K 1s donated electrons.

Furthermore, panel (c) of Figure 3.2.10 presents a closer look at the evolution of the B and C features. For the empty state B a shift of 0.5 eV towards lower energies can be attributed. Whereas, feature C gradually decomposed into three more features labelled C1, C2, and C3. Although, the transitions seem to be gradually due to scanning mixtures of states some certain onset values for the K concentration (x in K_x[MnPc]) could be determined. Thus, the peak C3 (at highest energy) branches out at x ~ 1, the feature C2 starts to develop for x ~ 2 and the feature C1 can be clearly seen at x ~ 4. However, we cannot exclude some σ^* antibonding contribution in the development of C3 (depicted in Figure 3.2.10(c) by the "?").

All shifts of the XAS feature towards lower energies can be rationalised as the outcome of the electronic structures relaxation by filling up the unoccupied states by the donated electrons.

3.2.2.4. Average Molecular Orientation and Surface Morphology

In the previous section it was emphasised the composition and evolution of the unoccupied electronic states determined by NEXAFS. Here, however, the data will be analysed with regard to the molecular orientation and film morphology. From section 3.1.3 the conclusion was drawn that CuPc crystallises differently on Au and on Co foils. There the measurements were performed at three different angles of incidence and the formula for the average molecular orientation could be employed. Since for the K intercalated MnPc the spectra were recorded only at two incidence angles just a trend could be derived. Moreover, upon filling up the unoccupied states with electrons others become the lowest one, *i.e.* the LUMO. The new LUMO states might have different symmetries depending on the occupation level in the MnPc molecule [Krol12].

Thus, in Figure 3.2.11 and Figure 3.2.12 the carbon and nitrogen *K edges* are presented, respectively, at normal (solid lines) and grazing (dashed lines) incidence for K concentrations of x = 0, x = 1.8, and x = 5.7. From the π^* to σ^* ratio at the two angles the conclusions can be drawn that pristine MnPc molecules on Co foil prefer a
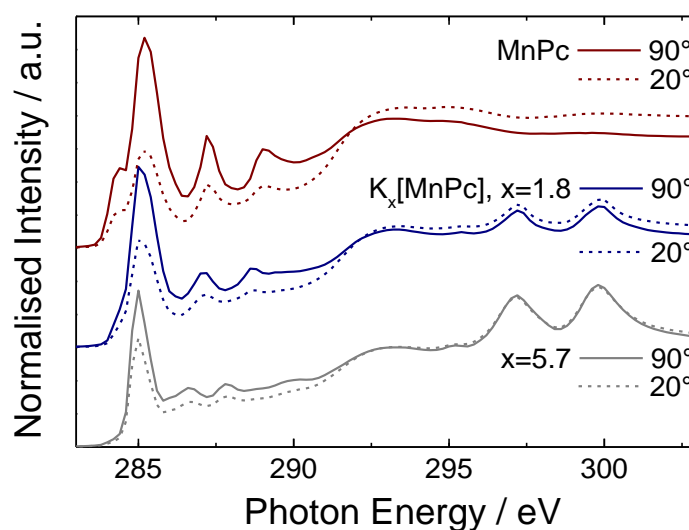
Figure 3.2.11. C *K edge* at normal ($\theta = 90°$, solid lines) and grazing ($\theta = 20°$, dashed lines) incidence for pristine and selected spectra of doped MnPc.

more standing orientation in a similar manner as CuPc does (see *e.g.* section 3.1.3). By the introduction of the dopant material within the crystalline structure of the molecules these reorient themselves. Moreover, upon K intercalation also phase transitions of Pc molecules were reported [Nils12, and literature within].

As the C *K edge* spectra at 90° and 20° approach each other upon K intercalation (Figure 3.2.11) the conclusion can be drawn that some reorientation of the molecules takes place. However, the evolution of the N *K edge* spectra (Figure 3.2.12) presents a different trend upon K doping, *i.e.* the π^* to σ^* ratio does not change. Therefore, a geometrical change in the π^* and σ^* antibonding electronic cloud should be taken into consideration, especially of the nitrogen atoms close to the central metal ion (N_M).

The surface of two samples was analysed by AFM. In Figure 3.2.13 the topography and phase images of two samples are presented. While the topography image provides information on the height of certain structures, the phase image is sensitive to the stiffness of the analysed materials [Mago97]. Thus, different types of materials can be distinguished by the analysis of the contrast in the phase image.

All the previously presented CL-PES and XAS measurements were performed on the MnPc(10 nm)/Co sample which is presented in Figure 3.2.13(b) and (d). It should be noted that the AFM measurements were performed in air after K intercalation ($x = 1.5$ for Au and $x = 5.7$ for Co substrate). The exposure to air could not be hindered
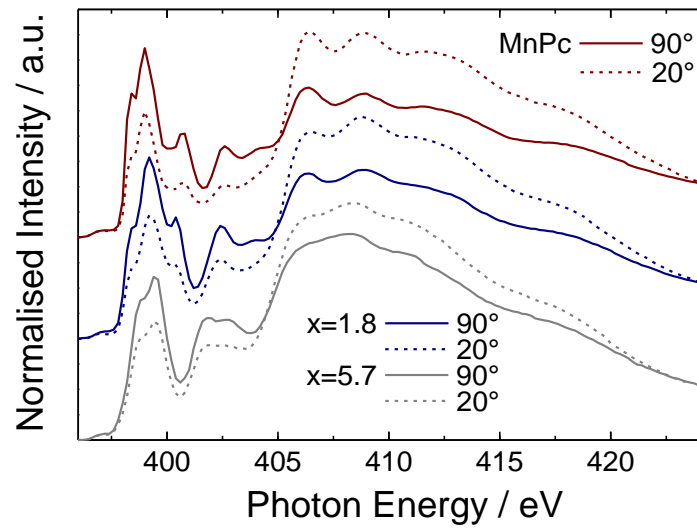
Figure 3.2.12. N *K edge* at normal ($\theta = 90°$, solid lines) and grazing ($\theta = 20°$, dashed lines) incidence for pristine and selected spectra of doped MnPc.
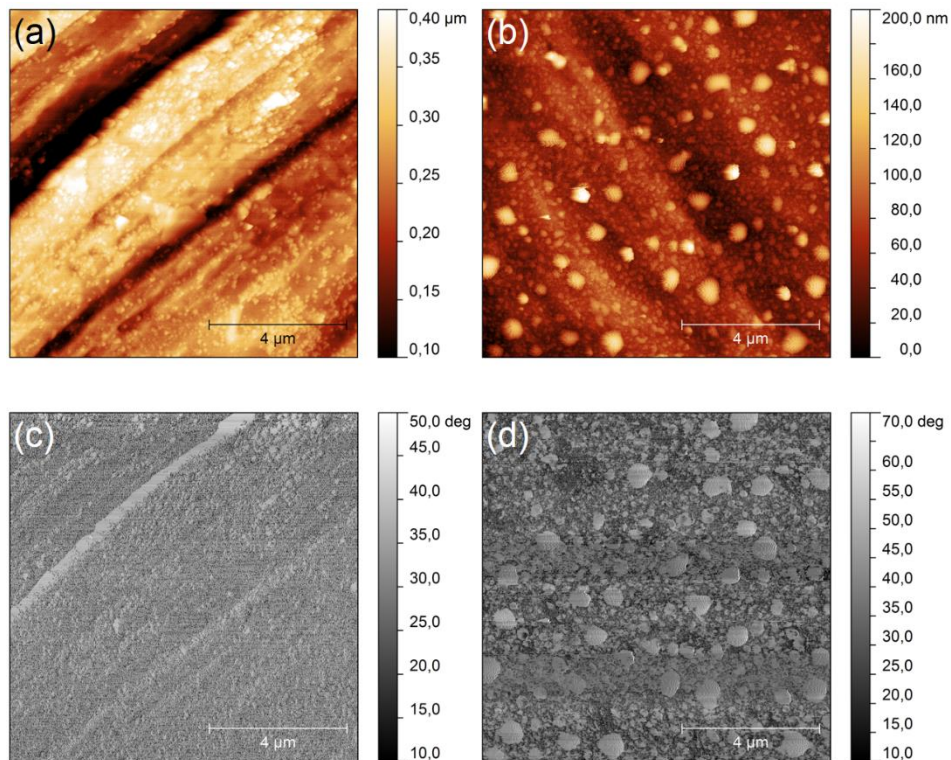
Figure 3.2.13. AFM topography (a, b) and phase (c, d) images of K intercalated MnPc(10 nm) films deposited on Au (a, c) and on Co (b, d) foils. The K amount was x = 1.5 on the Au (a, c) and x = 5.7 on the Co (b, d) foils. The images were taken in tapping mode.

and oxidation of K is expected. Besides the undulated surface of the Co foil in Figure 3.2.13(b) some island structures are visible. These can be clearly seen in the phase image (panel (d)) by having different contrast than the substrate. Since a 10 nm thick MnPc layer yields a closed film the contrast in the phase image is given between potassium oxide (and hydroxide) and the MnPc film.

To support the hypothesis that the islands are made of potassium oxides and hydroxides a second sample was produced and measured. For this sample 10 nm of MnPc was evaporated onto Au foil and intercalated with x = 1.5 amount of K. Again the AFM measurements were performed on the air exposed sample and are shown in Figure 3.2.13(a) and (b). Due to the smaller amount of K the islands are much smaller as in the case of the first sample.

Since the AFM images show the agglomeration of K oxides and hydroxides on the film surface the question is raised: whether or not K diffuses into the MnPc film and how deep can it go? Most of the work on alkali metal intercalation report an easy diffusion into the organic layers [Gao10, Hwan09, Ding05, Ge09, Crac05, Crac06, Mahn11, Nils12, Aris10, Aris11, *etc.*], however, there are some reports claiming the agglomeration on the surface [Fung04, Pi04, Kim12] due to strong chemical reactions especially in case of thicker organic films (> 30 nm [Kim12]).

For the 10 nm thick films studied in this work a diffusion through the whole organic layer is expected. The reaction between air and K is much stronger than the one between MnPc and K. Moreover, K atoms diffuse easier out of the molecular film than would O_2 and H_2O diffuse into the film. The conclusion can be drawn that the K oxides and hydroxides island formation on the MnPc film (Figure 3.2.13(b) and (d)) is most probably due to the air exposure which "extracts" via oxidation the intercalated K atoms out to the sample surface.

3.2.3. Influence of Air and O_2 Exposure on the Optical Properties

In situ SE measurements were performed on MnPc films prepared in the setup presented in section 2.3.2. The final nominal film thickness was as large as 90 nm in order to obtain a precise optical characterisation. All substrates were kept at room temperature during the experiments. The layer model for the fit was composed from a semi-infinite Si substrate with native oxide, and on top of it an isotropic B-Spline layer

[Johs08] which modelled the properties of the MnPc film. Even though Pc films usually have anisotropic optical properties [Gord04, Yana09], and the surface of the films can be rough, these properties were neglected due to the restricted measurements at fixed angle. To lower the correlation between the film thickness and the dielectric function, the data recorded at ten different thicknesses were coupled together during the fitting procedure. This means that the optical properties (*i.e. ε*) of all the films were kept the same only their thicknesses were different.

The imaginary part of the dielectric function (ε_2) determined for a MnPc film, and plotted as black line in Figure 3.2.14 resembles very well the absorption spectrum derived from EELS measurements in the energy range from 1 eV to 3 eV [Krau09, Grob10]. Therefore, the value of the lowest energy peak position reported in ref. [Krau09, Grob10] is considered as the optical band gap $E_{opt} = 0.5 \, \text{eV}$ of MnPc. Due to the limited spectral range from 0.7 eV to 5.0 eV of the SE measurements, with ellipsometry only the presence of an absorption feature below 1 eV can be confirmed, however its energetic position cannot be determined with good confidence (see *e.g.* the low energy side in Figure 3.2.14). The difference between E_t and E_{opt} provides a value for the exciton binding energy of (0.7 ± 0.3) eV. This value is close to that reported for CuPc, *i.e.* (0.5 ± 0.2) eV [Zahn06] or (0.6 ± 0.4) eV [Hill00A].
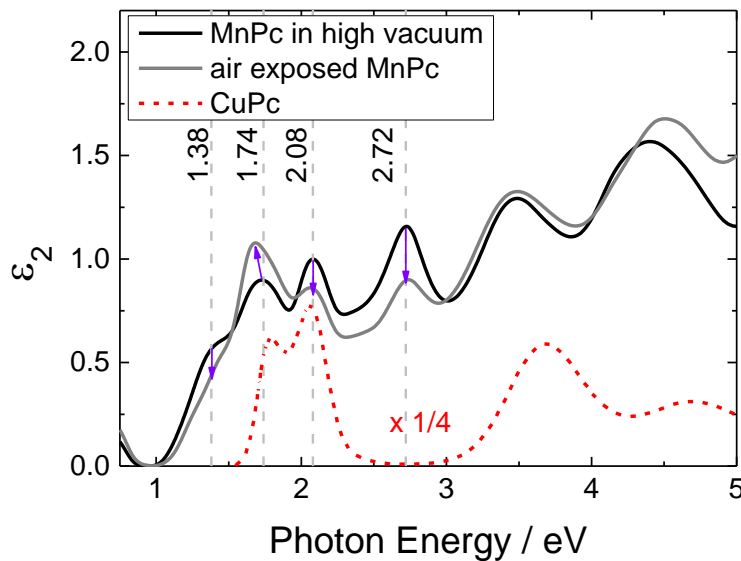
Figure 3.2.14. The imaginary part of the dielectric function of MnPc (black line), air exposed MnPc (grey line) and CuPc (red dashed line). The data for CuPc (from ref. [Gord04]) was recalculated to represent an isotropic layer and divided by a factor of 4 for comparison. The vertical dashed lines mark the most important peak positions for MnPc. The purple arrows indicate the peak evolution upon air exposure.

The optical absorption peaks at 1.38 eV and 1.74 eV in Figure 3.2.14 are attributed to the direct transitions between the first two occupied electronic bands, *i.e.* the HOMO (onset at 0.45 eV) and HOMO-1 (onset at 0.95 eV), and the LUMO (onset at -0.75 eV) as seen in the combined VB-PES and IPES study (Figure 3.2.2(b)) [Haid13A]. The attribution was done by observing the peaks evolution upon air exposure. While the HOMO has significant Mn 3d contribution, the HOMO-1 has a pure ligand π character [Grob11].

SE measurements performed on MnPc films after air exposure reveal marked changes in the dielectric function (Figure 3.2.14, grey line). The changes due to air exposure were attributed mainly to molecular oxygen [Frie12]. This is visible also in Figure 3.2.15 where the evolution of ε_2 is presented function of O_2 pressure in the experimental chamber. To exclude the influence of some artefacts produced by the change of pressure in the chamber the experiment was repeated with N_2. No spectral change was observed while the chamber was flooded with N_2, however immediately after ambient air was introduced the typical changes were recorded (see *e.g.* Figure 3.2.15). The results with N_2 exposure can be found in reference [Frie12]. The impact of water from ambient air cannot be excluded. The optical response changes fast due to air exposure, however, it requires significant time until it reaches saturation. The air
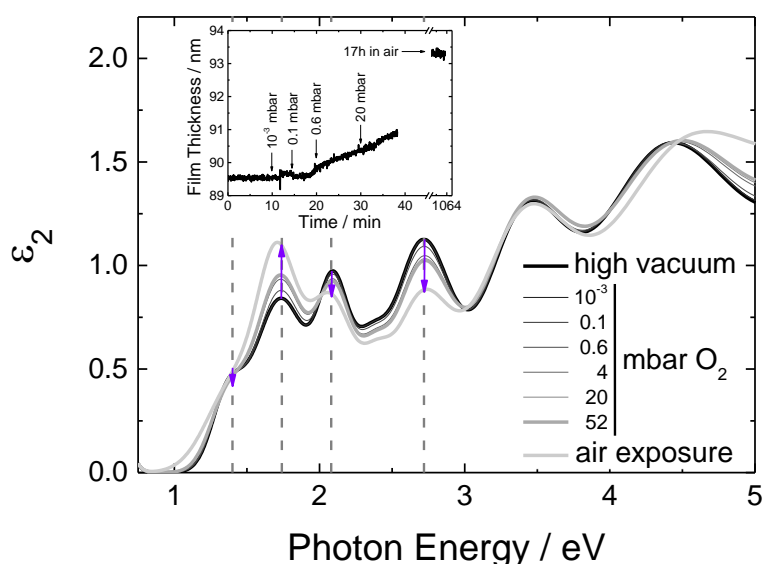
Figure 3.2.15. Evolution of the imaginary part of the dielectric function of MnPc upon O_2 and air exposure. Vertical grey dashed lines mark the peak positions according to Figure 3.2.14. The purple arrows indicate the evolution of the peaks. The inset presents the change in time of the MnPc film thickness via O_2 and air exposure.

exposure time for the results in Figure 3.2.14 was one day.

In Figure 3.2.15 a controlled experiment is presented: O_2 gas was introduced into the chamber while SE measurements were recorded. No significant change of ε_2 was observed for pressures lower than 1 mbar O_2. Consecutive increase of the O_2 partial pressure up to 52 mbar changes the features marked by the vertical dashed lines according to the direction given by the purple arrows. Three features decrease in intensity (at 1.38 eV, 2.08 eV, and 2.74 eV) while one increases (at 1.74 eV). After 17 h air exposure the latter peak also shifts to the red.

The evolution of the optical spectrum (Figure 3.2.15) is in concordance with the VB-PES and IPES measurements during air exposure (Figure 3.2.2(b)). The disappearance of the HOMO peak at 0.9 eV in the VB spectrum is mostly related to the reduction of the peak at 1.38 eV in the optical spectrum. The second peak at 1.74 eV (Q band for phthalocyanines [Gord04]) probably experiences an increase in oscillator strength due to a charge redistribution and/or deformation of the ligand upon the O_2 "adsorption". The inset of Figure 3.2.15 presents the change in thickness of the MnPc layer upon O_2 and air exposure. Through 17 h air exposure an increase of 4 % was determined from the fit. Although, the thickness is highly correlated with the optical constants this increase seems to be realistic.

Since the O_2 molecules (or water) cannot diffuse fast and fully through the MnPc film a long time is needed until saturation. In Figure 3.2.16 the ε_2 evolution upon heating of an air exposed MnPc sample is presented. The sample was kept in ambient air for one year. The resulting ε_2 is given by the thick light grey line. No perfect fit could be performed due to the complicated layered structure induced by the graded diffusion of O_2 into the thick film. The second difficulty was the increased roughness due to the long-time air exposure. For simplicity a homogeneous B-Spline layer was employed in the fit to model the modified MnPc film.

The evolution of ε_2 through the heating is monitored and presented by gradual change from the thick light grey line to the thick black line in Figure 3.2.16. The important features are marked by the vertical dashed lines and the trend is given by the purple arrows. The evolution is exactly reversed as in case of oxidation (see *e.g.* Figure 3.2.15). Not only is the intensity evolution reversed, but the peak at 1.74 eV has a blue-shift to the original position before oxidation. Thus, the O_2 "addition" process is fully reversible by heating up the molecular film. Although the trend is in the good direction, a final spectrum of pristine MnPc could not be obtained as the molecules
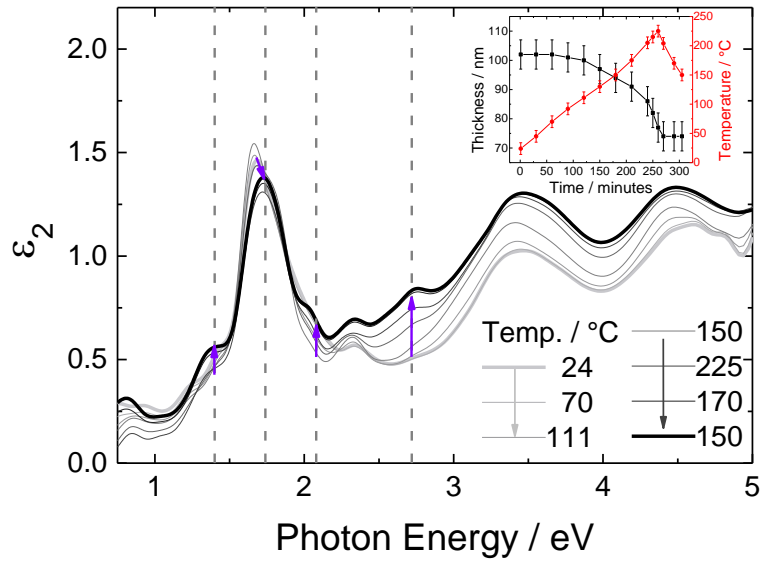
Figure 3.2.16. Evolution of the imaginary part of the dielectric function of a fully oxidised MnPc sample upon annealing. Vertical grey dashed lines mark the peak positions according to Figure 3.2.14. The purple arrows indicate the evolution of the peaks. The inset presents the change in film thickness and the sample temperature as a function of time.

started to desorb at temperatures above 200 °C (see the inset of Figure 3.2.16). Finally, the reversible process of the MnPc oxidation could be determined both by VB-PES and IPES (section 3.2.1) and SE measurements.

3.2.4. Impact of K Doping on the Optical Properties

In this section the development of the optical properties of MnPc via K intercalation are analysed. While oxygen removes electrons from the molecule, potassium donates its 1 s electron, thus the evolution of the absorption spectrum should differ considerably. MnPc film with ~70 nm thickness was deposited onto Si with native oxide substrate according to the experimental descriptions from section 2.3.2. The imaginary part of the dielectric function determined by *in situ* SE is plotted in Figure 3.2.17 with black line. It is in good agreement with the previous "oxidation" experiments (Figure 3.2.14 and Figure 3.2.15).

Whereas for the PES related measurements the doping procedure and spectra acquisition were performed in a stepwise manner, through all the *in situ* SE experiments the K intercalation could be monitored in real-time. The doping process of

the 70 nm thick film lasted several hours and spectra was acquired each 30 seconds. The outcome of the data analysis is plotted in Figure 3.2.17, where green, red, and blue lines represent the imaginary part of the dielectric function of MnPc with 1, 2, and 4 negative charges, respectively. These stem from K atoms with the particular concentration. All the intermediate steps are presented by thinner grey lines. The colour-bar inserted on the bottom of the plot denotes the colour of visible light in the specified energy range. This emphasises the strong changes in the visible rage of the absorption spectrum upon K doping.

In this subchapter the assignments $K_x[MnPc]$ with x = 1, 2, and 4 were given to the MnPc molecule charged with 1, 2, and 4 electrons, respectively. According to literature these represent the stable phases of the charged molecule [Mahn11]. In case of the *in situ* SE measurements the amount of K / MnPc could not be directly determined and the calibration from section 2.2.5 determined by means of CL-PES cannot be applied due to different thicknesses of the organic layer. Nevertheless, each change in SE spectra is attributed to a new phase formation which were assigned by comparing ε_2 with absorption features derived from EELS measurements in ref. [Mahn11]. Moreover, *in situ* Raman measurements confirmed the formation of the individual phases.
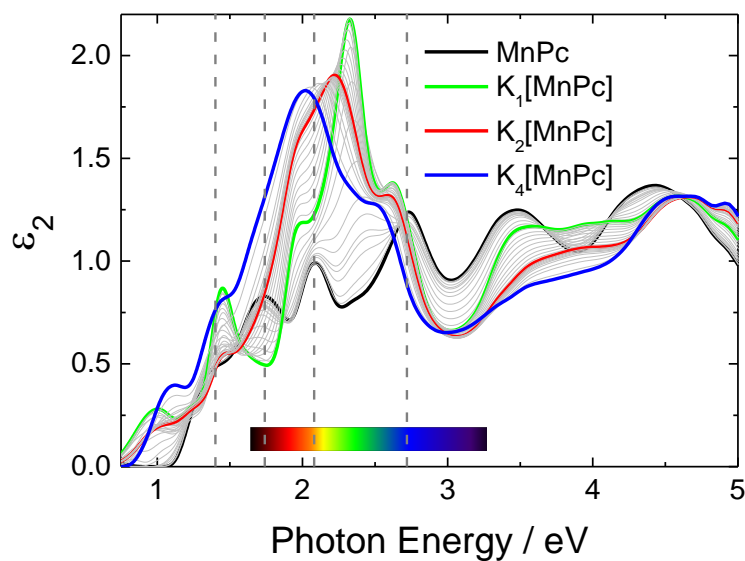
Figure 3.2.17. Evolution of the imaginary part of the dielectric function of MnPc upon K intercalation. The individual phases are presented by thick lines while the intermediate steps are given by thin grey lines. The colour-bar on the bottom denotes the colours of visible light in the specified energy range.

For a step-by-step analysis of the ε_2 evolution Figure 3.2.17 was stripped in three parts within the Figure 3.2.18. For consistency the previous colour code was preserved. Panel (a) depicts the gradual changes from the pristine MnPc towards the K_1[MnPc] phase. The direction of the peak evolution is provided by the red arrows. The peaks positioned on the dashed line marks follow several changes. Please note that these positions are followed during the "oxidation" studies of MnPc as well (section 3.2.3). The peak at 1.38 eV increases while the one at 1.74 eV decreases in intensity. Furthermore, the feature at 2.08 eV increases and has a red-shift, though the one at 2.72 eV shows no evolution. Moreover, the former feature seems to be an isosbestic point. Besides this one the spectra evolution displays several isosbestic points marked by blue circles. These mark the transition between two distinct phases without any intermediate step.

Consequently, all spectral changes on the dashed line marks in the Figure 3.2.18(a) exhibit opposite changes as the ones during O_2 exposure (Figure 3.2.15). Thus, each of the phenomena of "removing" and "donating" electrons from and to the molecule has its own "fingerprint" in the optical spectrum. Additionally, two extra features arise during the K_1[MnPc] phase formation: at 1.0 eV and around 2.4 eV. The latter one boosts up to an intensity twice as large as any previous feature. It also presents a red-shift and a shoulder just under the 2.72 eV mark.

By further K intercalation the spectra evolves towards the K_2[MnPc] phase presented in Figure 3.2.18(b). The important changes are highlighted by black arrows. The completion of the first doped phase is demonstrated by the decrease of the feature at 1.38 eV and the imposing peak around 2.3 eV. The latter one has a continuous red-shift. On the other hand, the feature just under the 2.08 eV mark increases further.

The third and last step in the spectral evolution of the doping procedure is the transition from the K_2[MnPc] towards the K_4[MnPc] phase (Figure 3.2.18(c)). The significant changes are marked by green arrows. The saturation of phase K_2[MnPc] was achieved once the feature at 1.38 eV started to increase again in intensity. Similarly, the peak just above 1 eV starts to increase. The strong feature around 2.2 eV, however, slightly decreases in intensity and shifts further towards lower energies. By further K intercalation the shape of the spectrum assigned as K_4[MnPc] (blue line) shows no further significant evolution due to saturation.

Additionally, all the previous K intercalation steps (phases) should be reversible in a similar manner to the "oxidation" process from section 3.2.3. In this instance,
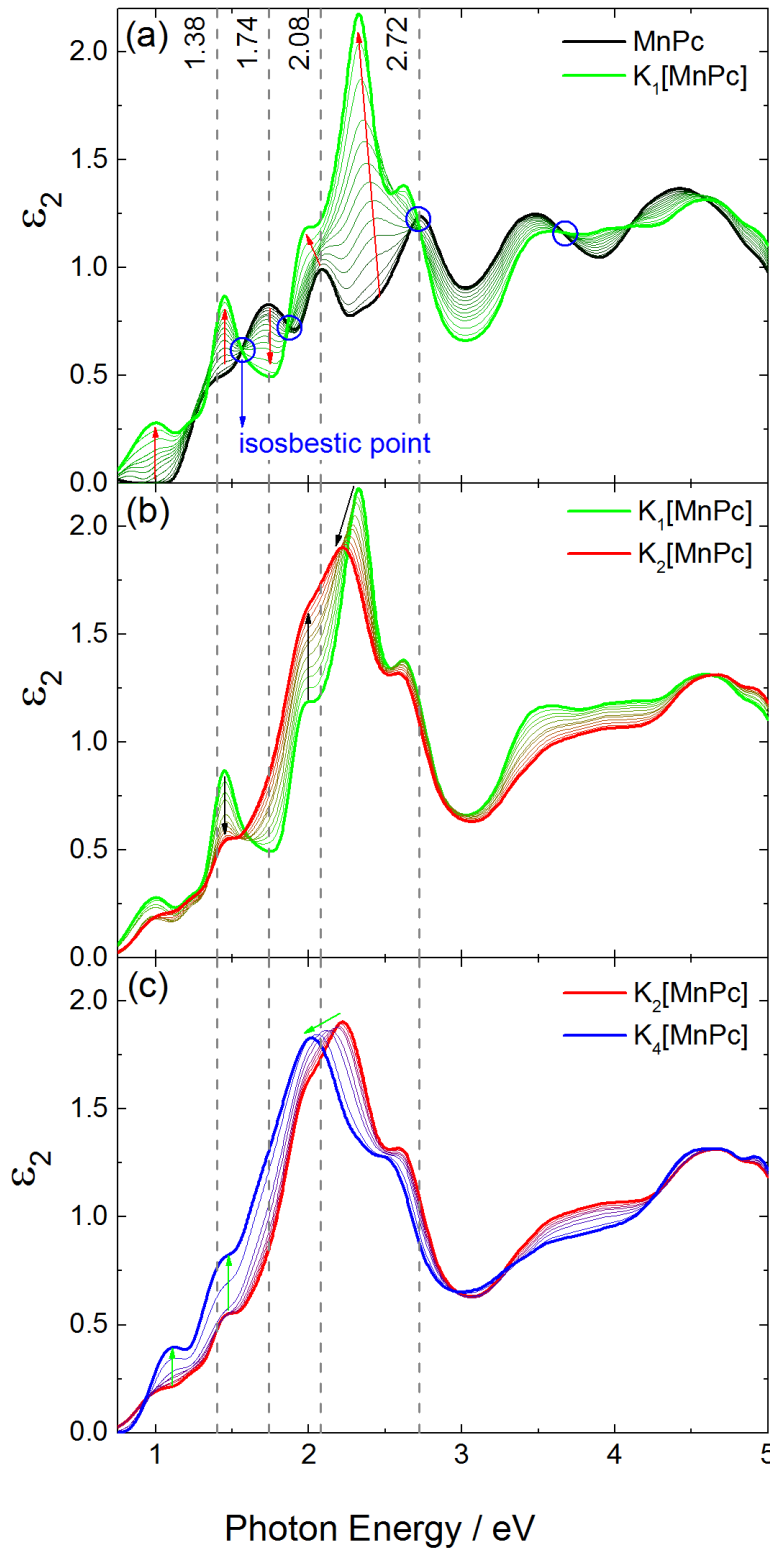
Figure 3.2.18. Detailed plot of the evolution presented in Figure 3.2.17 by highlighting the changes which occur within each doped phase transitions: (a) pristine MnPc → K$_1$[MnPc], (b) K$_1$[MnPc] → K$_2$[MnPc], and (c) K$_2$[MnPc] → K$_4$[MnPc]. The vertical grey dashed lines mark the peak positions according to Figure 3.2.14. Blue circles mark the isosbestic points. The peak evolutions are marked by red (a), black (b), and green (c) arrows for the three transitions individually.

however, the reversing process occurs through O$_2$ exposure instead of heat treatment. The changes in ε_2 of K$_4$MnPc by means of O$_2$ and air exposure are presented in Figure 3.2.19(a). Please note that the energy scale is reduced to (1 - 4) eV as the focus is set onto this particular range. The blue line (onset of evolution) represents the fully doped MnPc film (alike K$_4$[MnPc] in Figure 3.2.18(c)). By increasing the O$_2$ partial

pressure in the chamber the spectra evolve from $K_4[MnPc]$ to $K_2[MnPc]$ (red line) then to $K_1[MnPc]$ (green line) then to MnPc (black line) and finally to $O_2[MnPc]$ (grey line). Each step is marked by arrows as well. The colour code for the markers is set by the colour of the spectrum whichever they evolve into.

Thus, by tracking the changes of the features at 1.38 eV, 1.74 eV, and the large one just above 2 eV (see *e.g.* Figure 3.2.19(a)) the reversed evolution pattern of the doping process is evident up to the black line. Further, up to the grey line the characteristics via oxidation are detected. One may argue that the line shapes are not exactly the same as in Figure 3.2.18 and in Figure 3.2.15. The reason for that is the influence of many factors through the manipulation procedures. However, the important fingerprints of each phase are clearly distinguishable and the reversed procedure can be effectively traced.

In Figure 3.2.19(b) a picture of the sample presented in section 3.2.2.4 (Figure 3.2.13(a, c)) is shown. It consists of 10 nm MnPc deposited onto Au foil and subsequently doped by an amount of 1.5 K / MnPc. The sample before doping had a golden colour as the relatively thin layer of pristine MnPc does not absorb high amount of light. However, after the doping procedure, the colour changed to reddish as seen in Figure 3.2.19(b). This can be explained by the rise of the high absorption feature
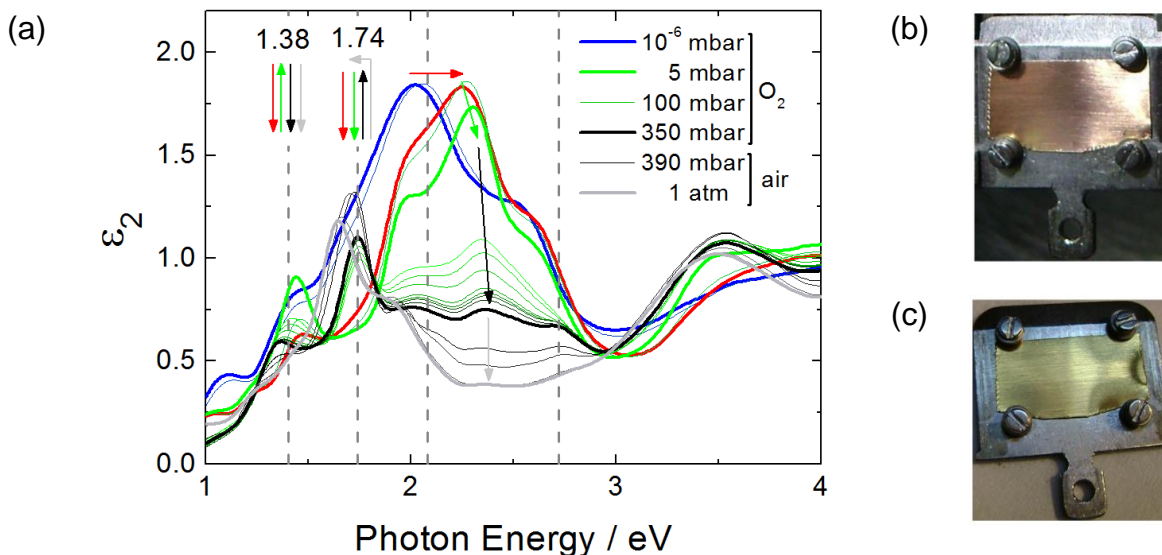
Figure 3.2.19. (a) Evolution of the imaginary part of the dielectric function of a fully doped MnPc film (K_4MnPc) via O_2 and air exposure. Vertical grey dashed lines mark the peak positions according to Figure 3.2.14. The arrows indicate the evolution of the peaks. Example: visible change in colour of $K_{1.5}[MnPc]$(10 nm)/Au (b) by means of air exposure (c).

above 2 eV and the decrease of the feature beneath 2 eV for this particular K dose (1.5 K / MnPc, see *e.g.* Figure 3.2.17). Therefore the absorption of the yellow and green light colours increases while the absorption of red light decreases. The reversibility of the process was proven by air exposure which induced the previous golden colour of the sample (see *e.g.* Figure 3.2.19(c)).

While other TMPcs have only two stable phases with x = 2 and x = 4 (*e.g.* ZnPc [Giov07], CuPc [Flat07], and FePc [Roth08]), MnPc also presents a stable phase with x = 1. The configuration holding 3 electrons per molecule is unfavourable and was not observed to be formed for any TMPc. It should be noted that the K intercalation process is continuous and the charged phases are formed consecutively, *i.e.* each later phase starts after the previous one is saturated.

Finally, some remarks about the saturation region should be made. Although SE spectra yield saturation of each phase via doping (Figure 3.2.18) it cannot be certainly said whether K diffuses through the whole layer, this being much thicker (70 nm) as for the PES experiments (10 nm). Moreover, considering the ε_2 of each doped phase (coloured lines in Figure 3.2.18) their linear combination should provide the ε_2 line shapes in between [Mahn11]. This linear component analysis, however, was not successful probably due to polarisation effects caused by the coexistence of several doped phases [Haid14]. This could indicate that the MnPc film is not fully penetrated by the K atoms and the consecutive phases form in clusters and cannot be regarded as a homogeneous medium. Probably a Maxwell-Garnett or Bruggeman effective medium approximation model [Aspn82, Haid12] could be employed, however this would only complicate the model too much. The scope here was to provide a simple way to determine ε_2 and provide relevant information on the observed changes. Although, as it will be shown in section 3.3.2 and in the reference [Haid14], the linear component analysis was successfully applied for the doped Alq$_3$ film.

3.2.5. Conclusions

In this final section the findings on MnPc thin films studied by PES related techniques and by *in situ* SE measurements are summarised. The results in the pristine state are presented first, followed by the changes upon O$_2$ exposure as well as K intercalation.

Combined VB-PES and IPES study of MnPc/Co provides information on the transport gap which amounts to (1.2 ± 0.3) eV, in agreement with DFT calculations [Grob11], and thus is smaller compared to *e.g.* CuPc ((2.2 ± 0.3) eV) due to the presence of metallic 3d SOMO states in the vicinity of the HOMO and LUMO bands. The transport gap decreases by 0.3 eV for the 1 nm MnPc film upon the influence of the image charge potential built up in the Co substrate. Finally, an interface dipole Δ = (-0.7 ± 0.1) eV was formed at the M-O interface having a constant value for all film thicknesses as a result of charge transfer at the MnPc/Co interface.

In situ SE measurements provided the dielectric function of MnPc films in the 0.7 – 5.0 eV spectral range. This is in good agreement with previous absorption measurements in a more restricted spectral range by Kraus *et al.* [Krau09] suggesting an optical band gap value of 0.5 eV. From the difference $E_t - E_{opt}$ the exciton binding energy of (0.7 ± 0.3) eV was determined, which is in the same range as for other TMPcs [Hill00A, Zahn06].

Both techniques, *i.e.* combined VB-PES and IPES and *in situ* SE measurements, confirmed previous suggestion that upon air exposure, mainly the metallic 3d hybrid electronic states are affected [Frie12]. Due to the disappearance of these states the HOMO is taken over by the HOMO-1, *i.e.* the π aromatic states, with the consequence of an increased E_t by 0.2 eV. Consecutively, the interface dipole decreases by 0.2 eV implying a shift of the Fermi edge by the same amount towards higher BEs. As a result all the modifications sustain the picture where the attached O_2 molecule removes charge from the metal centre of MnPc, thus inducing a *p-type* doping. The reversibility of the oxidation process was achieved by heating up the molecular film and was proven by both techniques.

The third part of this section deals with the electronic and optical properties of MnPc upon K intercalation. The VB-PES and IPES results show a rigid shift of the band, as expected [Ding09], with slight differences between the total shift of the occupied (0.8 eV) and unoccupied (1.2 eV) electronic states. Moreover, the core level shift is even less (0.5 eV), implying a more complicated scenario as that of a simple Fermi level shift. The influence of the photo-induced core hole on the valence states is different than on the stronger bound deeper levels. The presence of the intercalated K^+ ion has a large impact on the spectral shape of the C and N core level evolution upon doping. The crystallite structure of the pristine MnPc film provides a stacking of the molecule with consecutive pyrrole N atoms above the Mn central atoms [Liao05,

Tagu06]. In the doped film it was previously reported that at first K^+ ions prefer the location near the asa-bridging nitrogen (*i.e.* N_P) [Tagu06, Aris10] and after the saturation (4 K atoms), the benzene carbon atoms should be influenced. However, according to the core level spectra evolution it appears to be a mixture. The Mn $2p_{3/2}$ spectrum is not affected by the K^+ ions.

CL-PES provides information on the possible positioning of the K^+ ions while NEXAFS offers evidence where their donated electrons reside. The change in the X-ray absorption spectra of the C *K edge* is constant upon K intercalation. The Mn *L edge* on the other hand has a sudden jump between K_1[MnPc] and K_2[MnPc] which implies that the second electron already occupies antibonding states of the Mn centre. Moreover, the N *K edge* spectrum changes dramatically between K_2[MnPc] and K_4[MnPc] excluding the possibility of a state in between. This denotes the N antibonding states implication in accepting the third and fourth donated electrons. The sudden spectral changes observed for the Mn *L edge* and the N *K edge* evolution implies a strong hybridisation of the Mn 3d levels with the N 2p states [Petr12]. The angular dependences of N and C *K edges* upon doping denote a modification of the symmetry of the unoccupied electronic states. The branching ratio of the Mn *L edge* indicates a modification of the total spin of the molecule from $S = 3/2$ to a higher one.

Finally, the K doping process was monitored by *in situ* SE and the dielectric function evolution was deduced. Indeed, the optical response follows the changes through the 3 doped stable phases, *i.e.* K_1[MnPc], K_2[MnPc], and K_4[MnPc], which were previously reported by Mahns *et al.* [Mahn11]. It is the first time that the modification of the optical properties via alkali metal intercalation was monitored by *in situ* SE and combined VB-PES and IPES measurements. Moreover, MnPc shows huge changes in the absorption spectra already at $x = 1$ K atoms per molecule. Both the oxidation (O_2) and reduction (K) processes are reversible. The oxygen can be extracted by giving energy to the system in the form of heat (annealing). By exposing the fully doped MnPc film to O_2 a strong reaction with K is produced. This reverses the doped film stepwise through the pristine material towards the final product of MnPc-O_2.

3.3. Alq$_3$

Nowadays increasing effort is invested in novel organic semiconducting materials with the scope of implementing them into hybrid- or all-organic devices [Chau13]. Great success was achieved within the fields of organic light emission [Tang87, Feng01, Tagu10, Hwan09], organic photovoltaics [Gebe02, Aran00, Akai10], and flexible electronics [Forr04, Sun07, Schm13].

Tris(8-hydroxy-quinolinato) aluminium(III) (Alq$_3$) is the most studied and successfully implemented electron transport organic semiconductor in Organic Light Emitting Diode (OLED) devices. Since Tang and VanSlyke introduced the first organic electroluminescent diode in 1987 [Tang87] lots of improvements have been done [Feng01, Tagu10, Hwan09]. However, the device structure remained basically the same as it is reproduced in Figure 3.3.1. An active layer (AL) is sandwiched between the electron conductive layer (*e.g.* Alq$_3$) and the hole conductive layer (*e.g.* α-NPD, emphasised in subchapter 3.4) which are as well sandwiched between the cathode and the transparent conductive oxide (*e.g.* indium tin oxide, ITO) anode [Feng01, Hwan09]. Amongst other parameters the colour of the electro luminescence (EL) can be determined by the AL and the thickness of the Alq$_3$ layer [Feng01, Hwan09]. However, simple EL can be achieved also without the AL, *i.e.* at the Alq$_3$/α-NPD interface with Alq$_3$ as the emissive layer material [Tang87, Tagu10].

The electronic and optical properties of Alq$_3$ were previously investigated by combined VB-PES and IPES [Hill00A, Hill00B] and by SE measurements [Himc05], respectively. The occupied and unoccupied electronic states were studied by theoretical DFT calculations [Joha99, Lee12] and by using the semi-empirical Hartree-Fock (H-F) intermediate neglect of differential overlap (INDO) method [Hill00B]. The optical absorption spectrum was calculated employing the time-dependent density functional theory (TD-DFT) method [Choy08].

A successful way to improve device performance is by *n-type* doping of the Alq$_3$ film via alkali metal intercalation [Kim12, Lee12]. This method, to manipulate the electronic properties of Alq$_3$, was implemented long time ago [Joha99]. As electron donors for Alq$_3$ the following alkali metals were used: Li [Joha99], Na [Kim12], K [Saku02, Saku04, Joha99, Knup01, Lee12], Cs [Fung04, Ding05]; or even alkali earth metal like Mg [Pi04]. Sakurai *et al.* studied the impact of doping on the vibrational properties of Alq$_3$ [Saku02, Saku04]. However, most studies concentrate on the
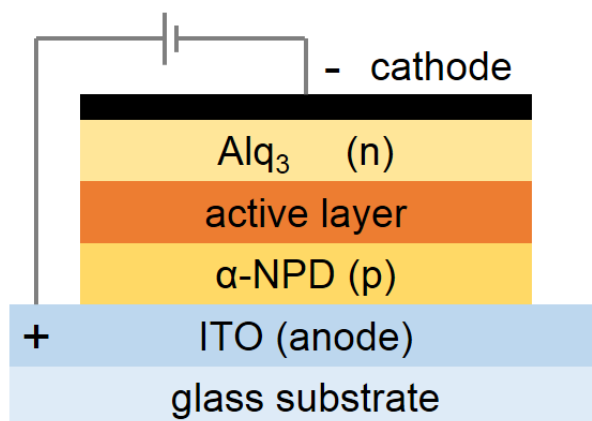
Figure 3.3.1. Side view of an OLED structure assembled with Alq_3 and α-NPD films as electron- and hole-transporting layers. Image reproduced according to references [Tang87, Feng01].

evolution of the electronic properties determined by VB-PES and CL-PES measurements [Joha99, Knup01, Fung04, Pi04, Ding05, Kim12, Lee12].

In the first part of this subchapter the modification upon K intercalation of the occupied and unoccupied electronic states were monitored by combined VB-PES and IPES measurements. Although plenty of VB-PES measurements on doped Alq_3 were previously performed, only one work on the inverse photoemission spectra evolution could be found in literature [Ding09], which is rather vague. Moreover, no literature could be found for the results in the second section, where *in situ* SE monitoring was employed to analyse the change in the optical response of an Alq_3 layer upon K intercalation.

3.3.1. Influence of K Intercalation on the Electronic Properties

The effect of potassium doping on the occupied and unoccupied electronic states of Alq_3 was studied by VB-PES and IPES measurements. First, a 10 nm film was deposited onto a clean, Ar^+ sputtered Co foil. Afterwards consecutive K intercalation and spectra acquisition steps were performed. The data is plotted in Figure 3.3.2 with emphasis in each panel on a specific part of the spectra. Panel (a) shows the secondary electron cut-off region while panel (b) presents the valence band region of the spectra. Panels (c) and (d) focus on the HOMO and LUMO regions, respectively. For clarity the spectra are shifted against each other starting from the bottom with the clean Co substrate followed by the pristine Alq_3 film and the stepwise
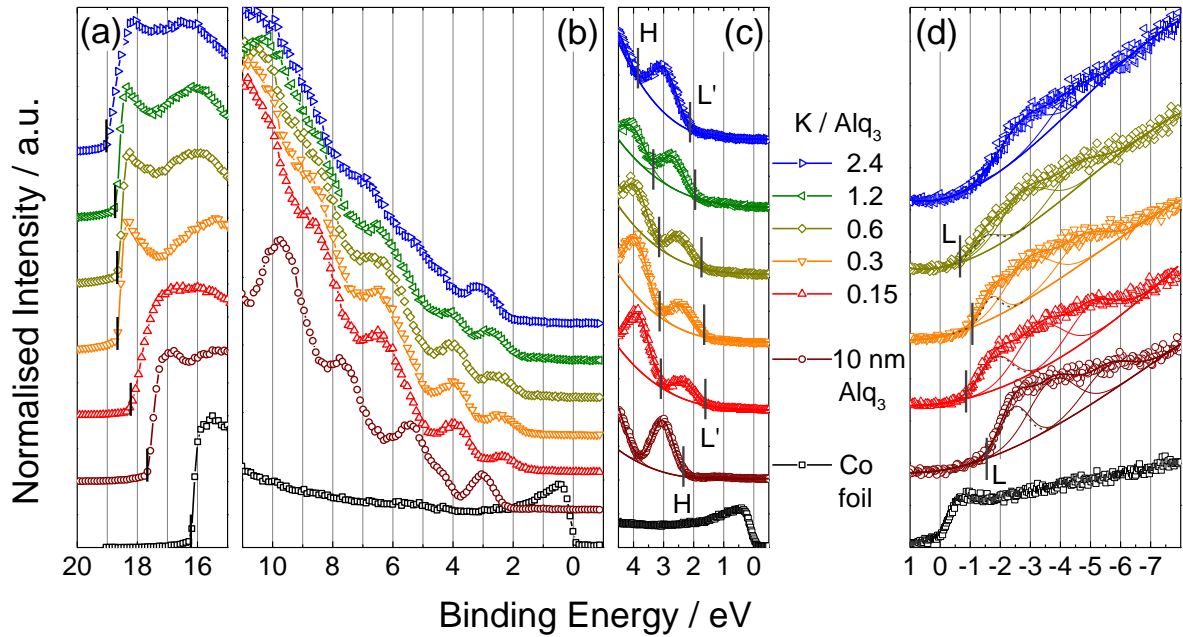
Figure 3.3.2. Evolution of the valence band (a, b, c) and inverse (d) photoemission spectra of K intercalated Alq$_3$ deposited on Co foil. The valence band photoemission spectra are divided into three regions: secondary electron cut-off (a), overview of the valence band (b), and the HOMO region (c). Vertical bars mark the secondary electron cut-off positions and the onset positions of the HOMO (H), filled LUMO state (L'), and LUMO (L).

doped films.

For data evaluation the fitting procedure presented in section 2.2.2 was employed. The outcome is presented in Figure 3.3.2(c) and (d) for pristine and doped molecular films. While in the HOMO region the onset of the features was strait forward to determine, in the LUMO region the features had to be deconvoluted according to equation (15). The resulting LUMO peaks are marked by grey dashed lines in the panel (d). The onset of the features are marked by vertical bars.

Upon doping the LUMO feature decreases in intensity and shifts towards the Fermi level. Simultaneously an extra feature (L') develops in the HOMO region composed of former unoccupied electronic levels filled with electrons. This L' feature is also referred to as a gap state [Knup01, Fung04, Ding05, Lee12] provided by the Coulomb repulsion around the Fermi energy [Joha99]. Moreover, the features in the valence band photoemission spectra also shift towards higher BEs via doping. The secondary electron cut-off positions and the onset positions of the HOMO, L', and LUMO are marked by vertical bars and summarised as data points in Figure 3.3.3(a). The amount of K / Alq$_3$ was determined by employing the calibration procedure presented in section 2.2.5.
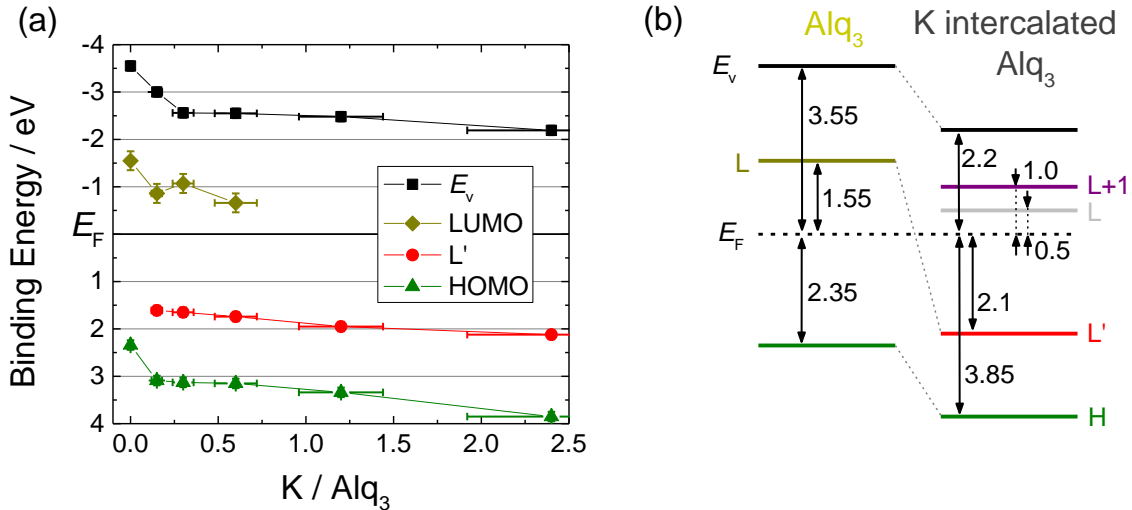
Figure 3.3.3. (a) The onset positions of the quantities determined in Figure 3.3.2 as a function of K amount. Instead of the cut-off position the vacuum level (E_v) is plotted. (b) Energy level diagram of the occupied and unoccupied electronic states of Alq3 before and after K intercalation.

In Figure 3.3.3(a) the evolution of the LUMO, L', HOMO, and E_v is plotted against the amount of intercalated K with regard to the Fermi level ($E_F = 0$ eV). The energetic positions of E_v (according to the conventions in this work: $E_v = -\Phi$) was determined considering the secondary electron cut-off positions. Not shown in the plot is the vacuum level for the Co substrate: $E_v^{Co} = -5$ eV. Hence, an interface dipole is formed between the Alq3 film and the Co substrate with a relatively large value of $\Delta = E_v^{Alq_3} - E_v^{Co} = (1.45 \pm 0.10)$ eV. As expected, all the levels shift collectively towards higher BEs upon K intercalation. At a minimal amount of K / Alq3 = 0.15 the shift is large (~0.7 eV) while by further doping up to an amount of K / Alq3 = 2.4 it gradually reaches to a total shift of ~1.5 eV.

From these results, the energy level diagram of the pristine and highly doped Alq3 is schematically shown in Figure 3.3.3(b). The *n-type* behaviour of the pristine Alq3 is provided by the closer positioning of E_F to the LUMO as compared to the HOMO level (1.55 eV vs. 2.35 eV). This behaviour is maintained even after doping since L' arises further away under E_F even at low doping amounts and the gap increases by further K intercalation. Thus, when fully doped L' is located 2.1 eV below E_F whereas the remaining LUMO (or possibly part of LUMO+1) approaches E_F not less than 0.5 eV. As a result no metallic behaviour was observed.

One of the reasons that the LUMO could be easily shifted below E_F, hence forming the L' state, is the *n-type* behaviour of Alq3 (unoccupied electronic states close

to E_F). This is not the case for the *p-type* organic semiconductors α-NPD (see *e.g.* subchapter 3.4). Such a shift in the electronic levels influences the optical properties presented in the subsequent section 3.3.2.

The other reason for the easy transition into the doped state can be found in the geometry and position of the occupied and unoccupied electronic states. According to literature the HOMO, HOMO-1, and HOMO-2 states are mostly localised on one of each of the phenoxide moiety of the three ligands while the LUMO, LUMO+1, and LUMO+2 wave functions are localised on the pyridyl moiety of each ligand [Hill00B, Choy08, Joha99]. CL-PES measurements provide the precise position of the donated electron to be localised on the N atoms [Joha99, Lee12]. The Al core of the molecule plays a minor role in transport and optical processes before [Hill00B] and after doping, unlike it was the case of MnPc in subchapter 3.2.

3.3.2. Influence of K Intercalation on the Optical Properties

The dielectric function of Alq$_3$ was determined by *in situ* SE measurements performed on a 70 nm thick layer deposited on Si with native oxide. The film growth was monitored both with QCM and SE measurements running in parallel. Data was modelled by a Cauchy layer (see *e.g.* section 2.3.3) which provided precise film thickness during the material deposition process. Hence, the growth process could be stopped at the required film thickness. The film thickness evolution is presented in the inset of Figure 2.3.4.

The evolution of the dielectric function of Alq$_3$ upon K intercalation was monitored by *in situ* SE and the imaginary part is shown in Figure 3.3.4(a). In the panels (b) and (c) emphasis is set on the features at lower and higher energies, respectively. The legend on the right hand side applies to the whole figure and represents the gradual change of ε_2 from pristine (min 1 – black line) to fully doped (min 160 – green line) phase. Note that the amount of K / Alq$_3$ molecule could not be assigned for the same reason as for MnPc in section 3.2.4, *i.e.* the calibration was made only for the 10 nm films. Hence, the amount of doping was quantified with time.

The data was evaluated in two steps. First, a Cauchy model was built to determine the exact film thickness at each K intercalation step. The transparent region up to 2.5 eV was fitted leaving the film thickness, A, and B (Cauchy parameters)

parameters free. Through the doping process the film thickness increases by 5 %. Due to strong correlation simultaneously the parameters A and B change as well, however, only within their fourth digit (see inset of Figure 3.3.4(a)). As the values of all parameters increase the film thickness increases and due to small changes of A and B the film thickness is determined precisely. The second step consists of fitting the data with a KK consistent B-Spline layer. The film thicknesses were fixed from the previously determined values. The resulting ε_2 are plotted in Figure 3.3.4.
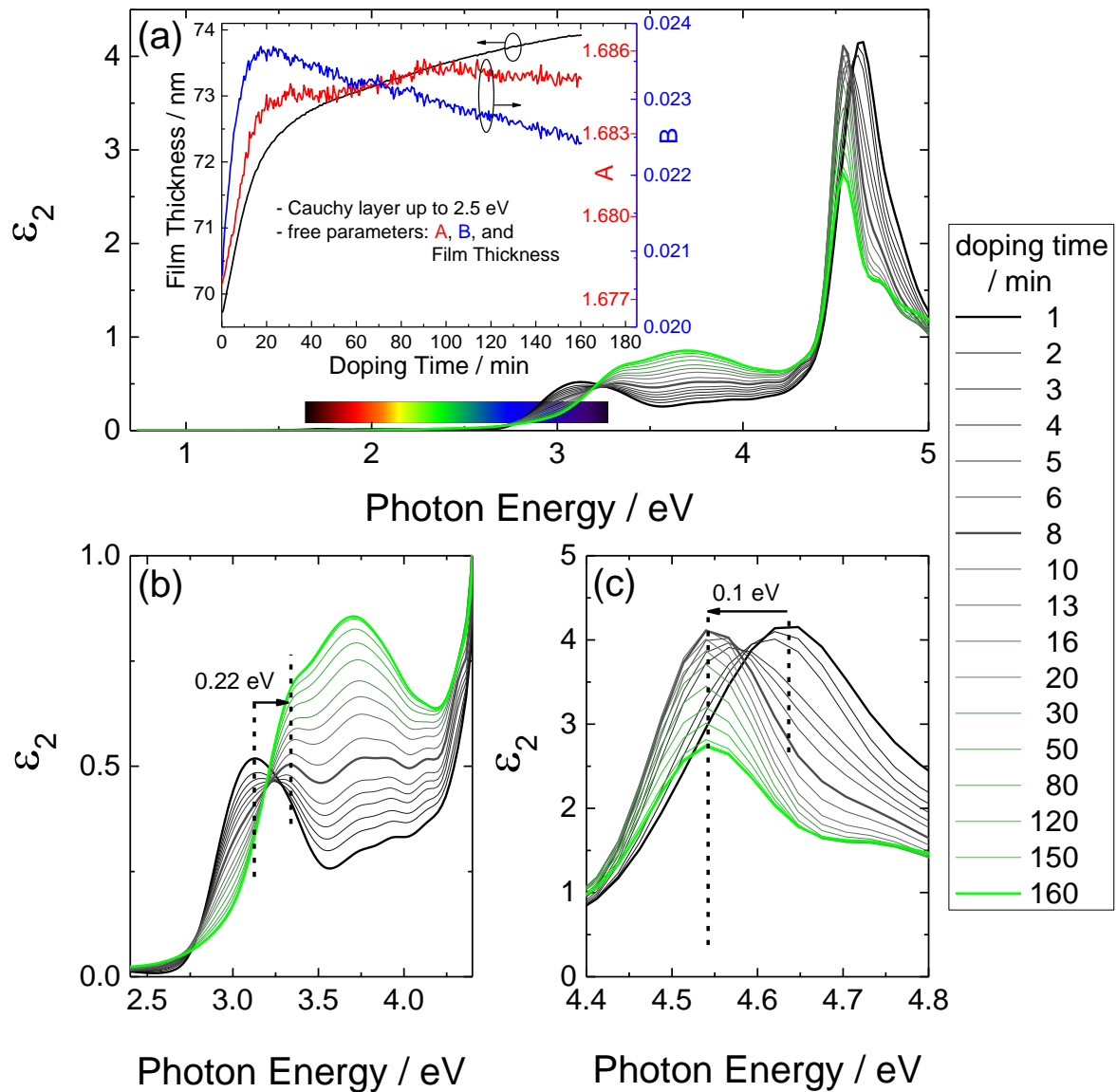
Figure 3.3.4. (a) Evolution of the imaginary part of the dielectric function of Alq$_3$ upon K intercalation. Closer view of the absorption features at lower (b) and higher (c) energies. The dashes vertical lines in (b) and (c) mark the peak positions and the arrows mark their evolution. The colour bar in panel (a) represents the colour of light at the specified energy. The inset in panel (a) depicts the change in film thickness and Cauchy parameters (A and B) as a function of the doping time.

The colour bar on the bottom of Figure 3.3.4(a) represents the colour of light at the specific energy. It emphasises the spectral region where the pristine Alq$_3$ and its doped phase starts to absorb light. Unlike for MnPc it only starts in the blue region and by doping it shift even more to higher energies. Thus the optical band gap, *i.e.* the position of the first feature, shifts by 0.22 eV towards higher energy (Figure 3.3.4(b)). The strong absorption feature at high energy has a red-shift from 4.64 eV to 4.54 eV in the first 8 minutes of doping (Figure 3.3.4(c)). With further doping up to minute 160 the feature does not shift anymore, it only reduces in intensity.

The spectra evolve between the pristine Alq$_3$ and the doped phase which, unlike MnPc, has only one visible stage. The reason for that is the possibility for the molecule to accommodate 3 K atoms on the 3 equivalent ligands [Joha99]. No distinction can be made between phases with 1, 2, and 3 K atoms per molecule. At minute 160 (Figure 3.3.4) saturation is reached, thus more than 3 K atoms per molecule will not modify its optical spectra.

The presence of the isosbestic point at 3.24 eV indicates that the optical response of the partially doped material is a linear superposition of the pristine Alq$_3$ spectrum and the K$_3$[Alq$_3$] spectrum. Thus no additional phases are involved. To test this hypothesis the spectral evolution was fitted by a linear combination of the pristine Alq$_3$ spectrum and the highly doped Alq$_3$ spectrum (Figure 3.3.5). The spectral region above 4.4 eV was excluded since it could not be simulated accordingly.

Therefore, the extinction coefficient (k) of pristine and K doped (160 min) molecule together with all the simulated spectra between are plotted in Figure 3.3.5. The residuals, *i.e.* the difference between measured and simulated spectra, are given in the inset. As the highest deviation is less than 10 % the linear component analysis proves that the mixture consists of only two components [Haid14].

The theoretical study (TD-DFT) of Choy and Fong [Choy08] on the optical transition within the Alq$_3$ molecule provides valuable information for the optical spectra analysis. The source of the absorption feature in the pristine state just above 3.0 eV (Figure 3.3.4) belongs to combined transitions from HOMO, HOMO-1, and HOMO-2 into the LUMO, LUMO+1, and LUMO+2 levels [Choy08]. These first 3 occupied and unoccupied electronic states could not be resolved in the VB-PES and IPES study and provide the same difficulty (or property) within the optical response. Moreover, the plateau between 3.5 eV and 4.0 eV is provided by HOMO $\rightarrow$ LUMO+4 transitions, or even higher order combinations [Choy08].
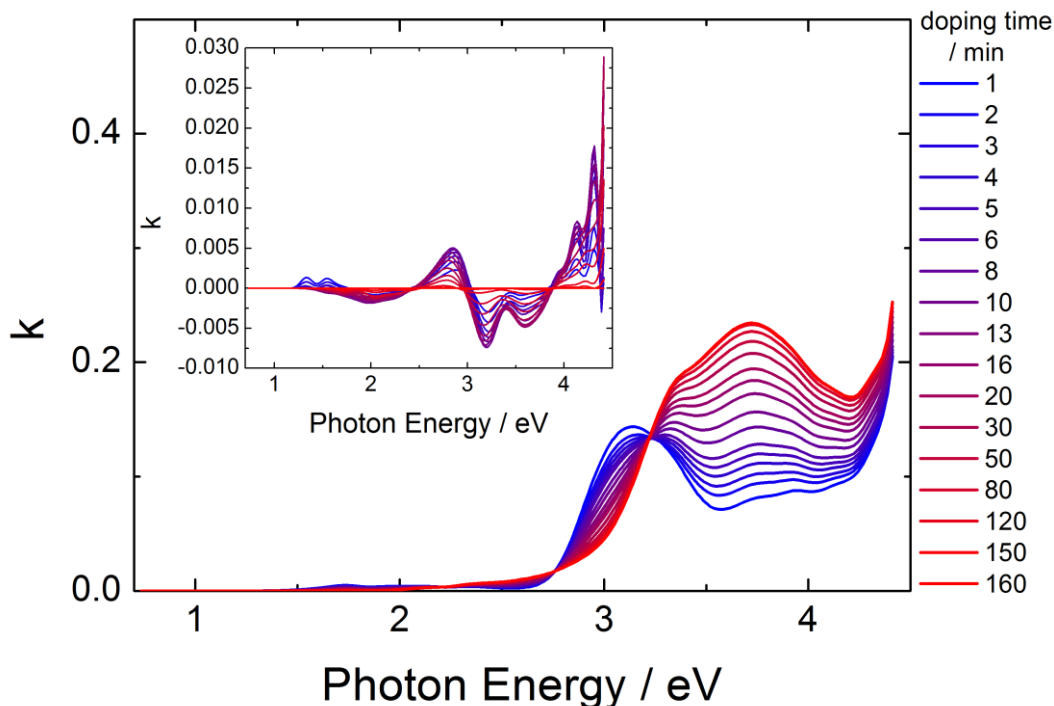
Figure 3.3.5. The simulated extinction coefficient (k) spectra of Alq$_3$ during K intercalation using a linear combination of pristine Alq$_3$ (min 1 – blue line) and highly doped Alq$_3$ (min 160 – red line). In the inset the residuals between simulated and experimental spectra are shown.

Therefore, according to the absorption spectrum evolution upon K doping the low order transitions gradually disappear as the LUMO states fill up with electrons, while the probability of higher order transitions increases. Except of slight increase in the absorption tail no lower energy feature could be detected, which means that no optical transitions from the L' state are possible (see *e.g.* Figure 3.3.3(b)).

3.3.3. Conclusions

Within this subchapter the electronic and optical properties of the organic semiconductor Alq$_3$ were analysed both in the pristine state as well as in *n-doped* configuration upon K intercalation.

From the valence band and inverse photoemission spectra the electronic properties in the pristine form were determined as: $\Delta = (1.45 \pm 0.10)$ eV, $EA = (2.0 \pm 0.2)$ eV, and $IE = (5.9 \pm 0.1)$ eV. The resulting transport band gap $E_t = (3.9 \pm 0.3)$ eV is well in between the literature values of (4.6 ± 0.4) eV [Hill00A] and (3.6 ± 0.3) eV [Krau10].

Additionally, the electronic properties of the highly doped K$_{2.4}$[Alq$_3$] film were determined: $EA^K = (1.2 \pm 0.2)\,eV$ and $IE^K = (4.3 \pm 0.1)\,eV$. Please note that these new EA^K and IE^K are defined by the L+1 and L' levels, respectively (see Figure 3.3.3). The resulting $E_t^K = (3.1 \pm 0.3)\,eV$ seems to have a relatively small value.

Furthermore, the dielectric function of pristine Alq$_3$ determined in section 3.3.2 is in very good agreement with the literature [Himc05]. The optical band gap $E_{opt} = 3.13\,eV$ was determined from the position of the first absorption feature. Upon K doping the line shape gradually evolves into the spectrum of K$_3$[Alq$_3$] with the consequence of an increased $E_{opt}^K = 3.35\,eV$. Since the inequality $E_t > E_{opt}$ does not hold anymore for the K intercalated Alq$_3$, either the L' gap state cannot be used to define E_t^K, or more probably, the transition from L' to LUMO+1 is optically not active [Haid14] and the second possible transition is between the HOMO and the LUMO+1 (see e.g. Figure 3.3.3(b)) which would increases the E_{opt}^K. Moreover, the exciton binding energy is also modified upon doping further complicating the picture.

The linear component analysis of the extinction coefficient evolution upon doping prove the existence of a single *n-doped* phase. The weight of the ε_2 spectrum gradually evolves into the one of K$_3$[Alq$_3$] and saturates. Thus, the molecule cannot be further doped. It was also shown that each of the 3 ligands provide the same optical response upon K intercalation.

Finally, the increase in the optical band gap upon doping provides a larger transparent region of the spectrum. This property is highly beneficial for light emission in the blue-UV region since the reabsorption of light can be omitted. The current density and EL are increased as well via doping, however, above the saturation threshold a decrease was noticed [Kim12, Lee12]. This can be well understood within the picture of filling up the LUMO states in two steps. First, a partial filling reduces the distance between the LUMO and E_F, thus increases the charge injection. Second, at fully occupied LUMO states (saturated K intercalation) no more charge injection is possible through this energy level, only through the states positioned at higher energies (*e.g.* LUMO+1).

In conclusion, a well-established study of alkali metal intercalated Alq$_3$ is necessary to optimise the device functionality parameters. Through this work a significant contribution has been made to this more than a decade long study which will still continue for the better understanding of the relationship between electrical and optical properties of the materials upon doping.

3.4. α-NPD: Influence of K Doping on the Optical Properties

While Alq$_3$ is the most commonly utilised electron-transport material, N,N'-diphenyl-N,N'-bis(1-naphthyl)-1,1'-biphenyl-4,4'-diamine (α-NPD) is one of the best suited hole-transporting layer in OLED devices [Tang87, Feng01, Tagu10] (see *e.g.* Figure 3.3.1). In literature it is also found abbreviated as NPB [Feng01, Lu03]. The optical properties of α-NPD were previously determined by SE measurements [Himc05]. The electronic properties are known from combined VB-PES and IPES measurements [Hill00A, Hill00B, Schw03]. Here, the change in the optical response upon K intercalation was analysed by *in situ* SE.

According to literature reports the positions of HOMO (H), LUMO (L), vacuum level (E_v), and K induced filled LUMO state (L') are specified with regard to the Fermi level (E_F) in the energy level diagram from Figure 3.4.1. The position of E_F has an offset of 0.4 eV between literature values [Hill00A, Schw03, Gao03A], thus the average quantities are given in the figure. Schwieger *et al.* [Schw03] determined the evolution of the electronic levels via K intercalation up to the concentration of 1.2 K atoms per α-NPD molecule. The resulting shifts of the bands are presented in the right hand part of the figure.

The doping of α-NPD can be either *p-* or *n-type*. For device fabrication the aim is to improve the hole conductive properties which could be obtained by a *p-type* doping. The materials, or molecules, best suitable for the application should have the EA close to or even larger than the IE of α-NPD. Two of such molecules were successfully implemented as molecular acceptors: tetrafluoro-tetracyanoquino-dimethane (F$_4$-TCNQ) [Gao03A] and Molybdenum tris-[1,2-bis(trifluoromethyl)ethane-1,2-dithiolene] (Mo(tfd)$_3$) [Qi10]. Even, the essentially intrinsic organic semiconductor ZnPc was successfully *p-doped* by the intercalation with F$_4$-TCNQ which led to an increase in the transport mechanism by seven orders of magnitude [Gao02]. The effect of such *p-type* doping is the shift of the Fermi level towards the HOMO and an enhanced hole injection and conductivity in the devices [Gao03A, Qi10]. The effect of *n-type* doping is exactly the opposite. Thus, by tuning the type and amount of the dopant the electrical properties of an organic transistor were manipulated [Lüss13].

The doping process can be achieved by diffusion of the dopant into the investigated material, by subsequent evaporation, or by co-evaporation of the two materials. The latter technique was used for both F$_4$-TCNQ and Mo(tfd)$_3$, however, the
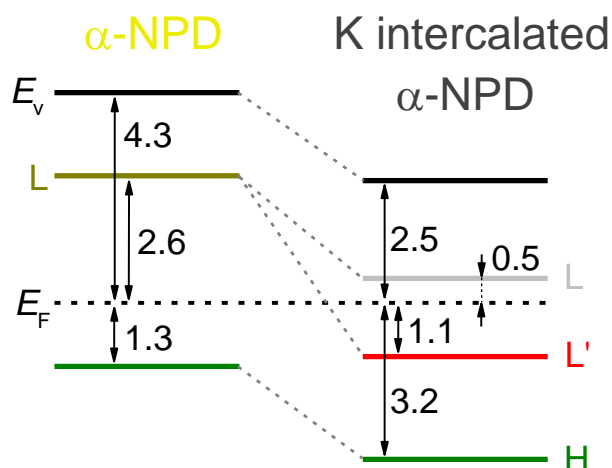
Figure 3.4.1. Energy level diagram for pristine and K intercalated α-NPD. The following levels are shown in the figure: vacuum level (E_v), Fermi level (E_F), HOMO (H), LUMO (L), and the filled LUMO state (L'). The energy positions of the different levels were selected from the references [Hill00A, Schw03, Gao03A]. Please note that due to inconsistencies in literature data, the average values are implemented in this work.

latter molecule provides better performance due to improved stability against diffusion into α-NPD [Qi10]. Nevertheless, diffusion is a very important fact for this work, as K intercalation was achieved by evaporating K onto the readily prepared organic film.

The motivation for employing the *n-type* doping procedure in this work is twofold. First, the evolution of the optical properties via doping can only be monitored *in situ* on samples for which the dopant materials diffuse into the investigated layer. Thus, *p-type* doping could not be employed. Moreover, there are no ellipsometry measurements in literature on alkali metal intercalated (*n-type* doped) α-NPD. The second more important reason is to compare the evolution of the electronic levels with the optical response to better understand the fundamentals behind the doping process.

The *in situ* SE monitoring of the doping procedure of α-NPD was performed in a similar manner as for MnPc (section 3.2.4) and Alq3 (section 3.3.2). Thus, a 70 nm thick α-NPD film was first deposited onto a Si substrate with native oxide and afterwards K was evaporated on top of it. The data obtained was analysed first with a Cauchy layer and afterwards by the KK consistent B-Spline layer just alike for Alq3 (section 3.3.2). The evolution of ε_2 is plotted in Figure 3.4.2 with the legend on the right hand side of the figure. Hence, the graded colour from black to green represents the evolution from pristine α-NPD (min 0) to the fully doped one (min 170) until saturation was reached. The amount of K per molecule could not be determined, as it
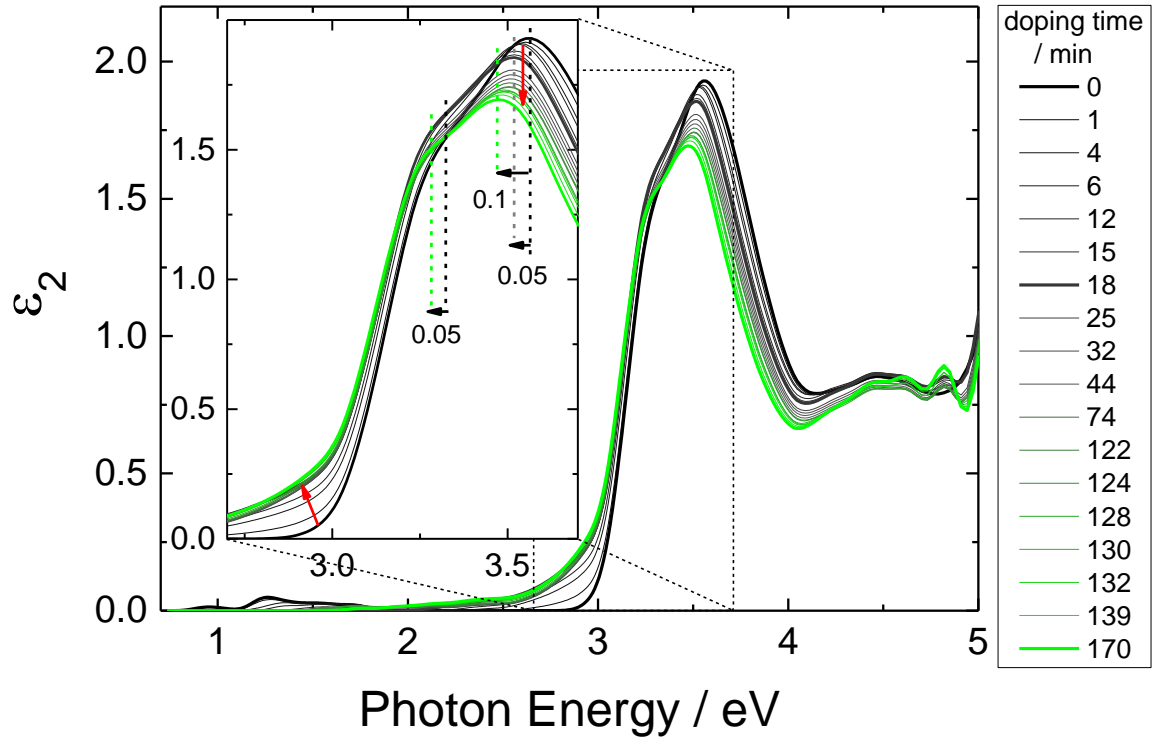
Figure 3.4.2. Evolution of the imaginary part of the dielectric function of α-NPD upon K intercalation. The inset represents a zoom of the selected region. The vertical dashed lines represent the peak positions at 0 min (black), 18 min (grey), and 170 min (green). The red arrows show the feature evolutions and the black arrows show the peak shifts with the written amounts.

was also the case for the previous two molecules, hence the doping time was ascribed to each spectrum. The spectrum of pristine α-NPD is in very good agreement with literature [Himc05]. The absorption onset is just above 3.0 eV and up to 5.0 eV the spectrum presents no more transparent region. Moreover, the broad absorption feature has a maximum centred at 3.55 eV and a shoulder at lower energy of 3.32 eV.

Upon K intercalation no strong changes of ε_2 could be observed, and the small variations are summarised in the inset of Figure 3.4.2. Up to a doping amount of 18 minutes the features have a red-shift of 0.05 eV and the absorption onset extends towards lower energies. It is striking that, while the rest of the spectrum has a further evolution, this absorption tail is already saturated at min 18. It was argued that it could be an Urbach absorption given by defect states within the gap [Haid14]. Which is very plausible, considering the appearance with low intensity of L' (see *e.g.* Figure 3.4.1) in the VB-PES and IPES experiments performed by Schwieger *et al.* [Schw03]. By further doping up to saturation the larger peak shifts again by an amount of 0.05 eV towards

lower energy and decreases in intensity, while the shoulder slightly decreases in intensity. These changes, however, do not suggest the formation of an extra stable phase, but more likely are influenced by modifications in the surface roughness or due to the formation of a K layer on top of the α-NPD film.

Why does α-NPD have no *n-doped* phase? To answer this question is the aim of this subchapter, *i.e.* to prove how large is the impact of the HOMO and LUMO levels energy position on the optical spectrum. The first challenge in obtaining an *n-doped* α-NPD molecule is the distant position of the LUMO to E_F (2.6 eV, see *e.g.* Figure 3.4.1). Nevertheless, by a small amount of K an energy shift of 1.4 eV of E_F towards the LUMO was achieved [Schw03]. Thus, the energy shift is possible, but still the LUMO does not "fill up" [Schw03] as drastically as in the case of the *n-type* semiconductor Alq₃ (see *e.g.* Figure 3.3.2).

Calculations on the occupied and unoccupied electronic levels were carried out using the semi-empirical H-F INDO method [Hill00B] simulating valence band photoemission spectra and inverse photoemission spectra. The TD-DFT method [Choy08] was employed to simulate the optical absorption spectra of α-NPD. The HOMO level is mainly localised on the N atoms and on the para C atoms of the two benzene rings in the biphenyl core [Hill00B, Choy08], while the LUMO level is more localised on the naphthalene units [Hill00B, Choy08] (see *e.g.* Figure 2.1.1). Due to the large torsion angle (~40°) between the conjugated moieties in the centre of the molecule fully delocalised energy levels (on the whole molecule) are absent [Hill00B]. Please note that in Figure 2.1.1 this torsion of the α-NPD molecule is missing in the plotted molecular structure due to the fast calculation mode, *i.e.* Universal Force Field [Rapp92] optimisation. The inverse photoemission spectrum of α-NPD has a broad feature [Schw03] which is actually composed of 14 individual levels [Hill00B]. Hence, by doping the molecule the donated electrons can "choose" plenty of energetic positions to occupy. Moreover, according to Choy *et al.* [Choy08] the broad absorption feature between 3.0 eV and 4.0 eV is mostly composed of the transitions H → L, H → L+2, and H-1 → L+1. One might also take into consideration the symmetry forbidden transitions for data analysis. Last, the shifts seen in valence band and inverse photoemission spectra [Schw03] do not necessarily mean that the donated electrons fill up the LUMO state, but they might contribute to the final electronic configuration such that the optical transitions remain unaffected.

In conclusion, by *in situ* SE monitoring of the K intercalated α-NPD film was demonstrated that no negatively charged phase is formed. Additionally, the decrease of the optical band gap was observed. The first absorption peak was red-shifted by 0.05 eV and the absorption onset was red-shifted by 0.5 eV. In consequence the *n-type* doping of the *p-type* α-NPD layer is not beneficial for OLED structures as the transparent region decreases.

4. Summary

In this work the electronic and optical properties of planar (CuPc and MnPc) and non-planar (Alq₃ and α-NPD) organic molecules have been studied by combined Valence Band Photoemission Spectroscopy (VB-PES) and Inverse Photoemission Spectroscopy (IPES), by Core Level Photoemission Spectroscopy (CL-PES), Near Edge X-ray Absorption Fine Structure (NEXAFS) spectroscopy, and by *in situ* Spectroscopic Ellipsometry (SE). For the electronic characterisation the Copper Phthalocyanine (CuPc), Manganese Phthalocyanine (MnPc), and tris(8-hydroxy-quinolinato) aluminium(III) (Alq₃) molecules were sublimed onto metal substrates whereas for the optical characterisation the MnPc, Alq₃, and N,N'-diphenyl-N,N'-bis(1-naphthyl)-1,1'-biphenyl-4,4'-diamine (α-NPD) molecules were sublimed onto Si(111) with native oxide substrate by OMBD. The first part of the work concentrates at the metal-organic semiconductor interface formation. The second and third parts study the electronic and optical properties, respectively, of the pristine, air exposed, and potassium intercalated molecules.

The interface formation between CuPc and two representative metal substrates, *i.e.* Au and Co, was investigated by the combination of VB-PES and IPES as well as by CL-PES thickness dependent measurements. These techniques are very surface sensitive, hence the properties of the uppermost molecular layer are investigated. The occupied and unoccupied molecular orbitals and thus the transport band gap of CuPc are extremely influenced by film thickness, *i.e.* molecule to substrate distance. Due to the image charge potential [Knup05, Flor09, Tsip02] induced in the metallic substrates the transport band gap of CuPc "opens" from (1.4 ± 0.2) eV for 1 nm film thickness to (2.2 ± 0.2) eV above 10 nm CuPc thickness and it saturates at this value. The thick film value of E_t is in good agreement with the literature [Hill00A, Gorg05, Zahn06]. The interface dipoles of (1.0 ± 0.1) eV and (1.2 ± 0.1) eV for CuPc on Co and Au substrates, respectively, depend on the metal work functions.

It was determined that the HOMO onset and the core level positions at the CuPc/Co interface have a 0.2 eV offset towards lower binding energy in comparison to the CuPc/Au interface. Although, there is a charge transfer from the Au (or Co) substrate to the Cu metal centre and reduces it from Cu(II) to Cu(I) [Schm11, Aris09A] it is only substantial at sub-monolayer thicknesses [Lach12]. In this study, however, a net charge transfer for films in the nm range was observed from the molecules to the

Co substrate due to chemisorption. This could be exploited to manipulate the molecular spin state [Bhan13]. Thereby, the Fermi level shifts in the same direction as if the molecule would be *p-type* doped [Lüss13]. This is a competing phenomenon with the band gap opening in the HOMO region. Consequently, tailoring the interface chemical environment highly influences not only the spin injection capabilities [Lach12] but also the energy level alignment at the hybrid M-O interface, which is a crucial element for both, electronic and spintronic devises.

Similar thickness dependent VB-PES and IPES study of the MnPc/Co interface provides information on the transport gap which amounts to (1.2 ± 0.3) eV. It is smaller compared to the one of CuPc due to the presence of the metallic 3d SOMO states close to the Fermi level. Nevertheless, the same band gap "opening" phenomenon was observed for the MnPc/Co interface which decreases by 0.3 eV for the 1 nm MnPc thin film. Furthermore, valence band and inverse photoemission spectra of oxidised (by O_2 exposure) and reduced (by K intercalation) MnPc films were analysed and the resulting electronic properties were determined. The K intercalation process was applied for the Alq$_3$ molecular film as well and the electronic properties of the pristine and doped phases were determined.

All the previously introduced quantities are summarised in Table 4.1 for thick and thin CuPc films on Co and Au foils, for thick and thin MnPc film on Co foil, for the oxidised and reduced states of MnPc, and finally for the Alq$_3$ film and its reduced form. Please note that EA and IE of the K intercalated films are defined as the difference between the vacuum level and the L+1 and L' states, respectively. While for MnPc the doping process induces an increase of the E_t, for Alq$_3$ it decreases dramatically.

The second most important experimental technique of this work was *in situ* SE. Three molecules were investigated in their pristine and K intercalated forms: MnPc, Alq$_3$, and α-NPD. The optical band gaps determined from the first absorption peak position are summarised in Table 4.2. Both the transport band gap and the optical band gap of MnPc are smaller compared to other phthalocyanines due to metallic Mn 3d states close to the Fermi level. On the other hand the exciton binding energy of (0.7 ± 0.3) eV is in the same range as for the other TMPcs [Hill00A, Zahn06]. Upon doping the low absorption features of MnPc disappear starting with the K$_1$[MnPc] phase and no additional low energy feature arises upon further doping [Mahn11]. Hence, E_{opt} of the K intercalated MnPc film could be clearly determined from the *in situ* SE data.

molecular film / substrate	Φ / eV (± 0.1)	Δ / eV (± 0.1)	IE / eV (± 0.1)	EA / eV (± 0.2)	E_t / eV (± 0.3)
CuPc / Co	4.0	1.0	5.1	2.9	2.2
CuPc(1 nm) / Co	4.3	0.7	5.2	3.9	1.3
CuPc / Au	4.0	1.2	5.1	2.9	2.2
CuPc(1 nm) / Au	4.2	1.0	5.1	3.6	1.5
MnPc / Co	4.3	0.7	4.75	3.55	1.20
MnPc(1 nm) / Co	4.3	0.7	4.55	3.70	0.85
O_2[MnPc]	4.5	0.5*	5.25	3.80	1.45
K_4[MnPc]	3.0	2.0*	3.40**	1.80**	1.60**
Alq_3 / Co	3.55	1.45	5.90	2.0	3.9
K_3[Alq_3]	2.20	2.80*	4.30**	1.2**	3.1**

Table 4.1. Work function (Φ), interface dipole (Δ), ionization energy (IE), electron affinity (EA), and transport gap (E_t) of CuPc, MnPc, and Alq_3 films (bulk-like or thin) on different substrates (Co or Au) and under O_2 and/or K influence, selectively. Notes: (*) due to the external stimulus (O_2 or K) on the molecular film the values do not represent anymore the "classical" interface dipole, (**) the values of IE, EA, and E_t were determined as the energetic distances between E_v - L', E_v - L+1, and L+1 - L', respectively.

Furthermore, the dielectric function of pristine Alq_3 is in very good agreement with the literature [Himc05]. Upon K doping the line shape gradually evolves into the spectrum of K_3[Alq_3] with the consequence of increasing the optical band gap from 3.13 eV up to 3.35 eV. Since the inequality $E_t > E_{opt}$ does not hold anymore for the K intercalated Alq_3 either the L' gap state cannot be used to define E_t^K or the direct comparison between E_t and E_{opt} cannot be made as the optical transitions from L' to L+1 are forbidden. For α-NPD on the other hand a decrease of the optical band gap by 0.05 eV was observed (see *e.g.* Table 4.2).

By *in situ* SE and combined VB-PES and IPES measurements the reversibility of the oxidation process of MnPc was proven. The detachment of O_2 from the MnPc molecules was achieved by heating up the molecular film. Similarly, *in situ* SE monitoring showed the reversibility of the reducing process by O_2 exposure. By the fast oxidation of potassium its impact on the MnPc molecules was neutralised.

molecular film	MnPc	K$_1$[MnPc]	K$_4$[MnPc]	Alq$_3$	K$_3$[Alq$_3$]	α-NPD	K$_x$[α-NPD]
E_{opt} / eV (± 0.05)	0.50*	1.00**	1.12**	3.13	3.35	3.32	3.27

Table 4.2. The optical band gap (E_{opt}) of selected molecules in pristine and K intercalated states. Notes: (*) value determined according to ref. [Haid13A, Krau09, Grob10], (**) values determined by matching data from ref. [Mahn11], in correlation with *in situ* SE results of this work.

The electronic properties of MnPc upon K intercalation were intensely studied by CL-PES and NEXAFS techniques. The presence of the intercalated K$^+$ ion has a large impact on the spectral shape of the C and N core level evolution upon doping, while the Mn 2p$_{3/2}$ spectrum is not affected. In consequence the K$^+$ ions prefer to position near the asa-bridging nitrogen (*i.e.* N$_P$) and on the benzene rings. NEXAFS offers evidence where the K donated electrons reside. The Mn *L edge* evolution implies that the second donated electron per MnPc molecule occupies the hybridised antibonding states of the Mn ion. The N *K edge* spectrum evolution suggests the N antibonding states implication in accepting the third and fourth donated electrons. The sudden spectral changes observed for the Mn *L edge* and the N *K edge* evolution implies a strong hybridisation of the Mn 3d levels with the N 2p states [Petr12]. The angular dependences of N and C *K edges* upon doping denote a modification of the symmetry of the unoccupied electronic states. Moreover, the branching ratio of the Mn *L edge* indicates a modification of the total molecular spin from S = 3/2 to a higher state. Finally, it is worth mentioning that XAS studies on molecular films upon doping are scarce in literature and should be more intensely performed in the future.

This is the first *in situ* SE study on the modification of the optical properties via alkali metal intercalation. MnPc presents plenty of features throughout the absorption spectrum and shows huge changes already at 1 K atoms per molecule. Smaller spectral modification were observed for Alq$_3$, whereas α-NPD presents the smallest changes. By the linear component analysis of pristine and doped Alq$_3$ it was proven the existence of a single *n-doped* phase.

Finally, the doping induced properties of organic molecules provide a lot of potential not only to increase device performance but also in basic research to understand the dynamics at the electronic level.

References

[Akai10] K. Akaike, K. Kanai, Y. Ouchi, and K. Seki, Adv. Funct. Mater. **20**, 715 (2010)

[Ange11] M. Angelucci, P. Gargiani, C. Mariani, M. G. Betti, J. Nanopart. Res. **13**, 5967 (2011)

[Aran00] A. C. Arango, L. R. Johnson, V. N. Bliznyuk, Z. Schlesinger, S. A. Carter, and H.-H. Hörhold, Adv. Mater. **12**, 1689 (2000)

[Aris09A] V. Yu. Aristov, O. V. Molodtsova, Yu. A. Ossipyan, B. P. Doyle, S. Nannarone, and M. Knupfer, Org. Electron. **10**, 8 (2009)

[Aris09B] V. Yu. Aristov, O. V. Molodtsova, Yu. A. Ossipyan, B. P. Doyle, S. Nannarone, and M. Knupfer, Phys. Status Solidi A **206**, 2763 (2009)

[Aris10] V. Yu. Aristov, O. V. Molodtsova, V. V. Maslyuk, D. V. Vyalikh, T. Bredow, I. Mertig, A. B. Preobrajenski, M. Knupfer, Org. Electron. **11**, 1461 (2010)

[Aris11] V. Yu. Aristov, O. V. Molodtsova, M. Knupfer, Org. Electron. **12**, 372 (2011)

[Arsh02] A. Arshak, S. Zleetni, and K. Arshak, Sensors **2**, 174 (2002)

[Aspn82] D. E. Aspnes, Thin Solid Films **89**, 249 (1982)

[Atod10] N. Atodiresei, J. Brede, P. Lazic, V. Caciuc, G. Hoffmann, R. Wiesendanger, and S. Blügel, Phys. Rev. Lett. **105**, 066601 (2010)

[AVOG] http://avogadro.openmolecules.net/ (19.02.2014)

[Azza87] R. M. A. Azzam and N. M. Bashara, Ellipsometry and Polarised Light, Elsevier, Amsterdam (1987)

[Barr70] C. G. Barraclough, R. L. Martin, and S. Mitra, J. Chem. Phys. **53**, 1638 (1970)

[Barr10] C. Barraud, P. Seneor, R. Mattana, S. Fusil, K. Bouzehouane, C. Deranlot, P. Graziosi, L. Hueso, I. Bergenti, V. Dediu, F. Petroff, and A. Fert, Nature Phys. **6**, 615 (2010)

[BESS] http://www.helmholtz-berlin.de/quellen/bessy/index_en.html (19.02.2014)

[Bhan13] S. Bhandary, B. Brena, P. M. Panchmatia, I. Brumboiu, M. Bernien, C. Weis, B. Krumme, C. Etz, W. Kuch, H. Wende, O. Eriksson, and B. Sanyal, Phys. Rev. B **88**, 024401 (2013)

[Bies11] M. C. Biesinger, B. P. Payne, A. P. Grosvenor, L. W. M. Lau, A. R. Gerson, and R. St. C. Smart, Appl. Surf. Sci. **257**, 2717 (2011)

[Bloo07] F. L. Bloom, W. Wagemans, M. Kemerink, and B. Koopmans, Phys. Rev. Lett. **99**, 257201 (2007)

[Bohr07] F. I. Bohrer, A. Sharoni, C. Colesniuc, J. Park, I. K. Schuller, A. C. Kummel, and W. C. Trogler, J. Am. Chem. Soc. **129**, 5640 (2007)

[Bonz95] H. P. Bonzel and Ch. Kleint, Prog. Surf. Sci. **49**, 107 (1995)

[Bren04] B. Brena, Y. Luo, M. Nyberg, S. Carniato, K. Nilson, Y. Alfredsson, J. Ahlund, N. Martensson, H. Siegbahn, and C. Puglia, Phys. Rev. B **70**, 195214 (2004)

[Brum14] I. E. Brumboiu, R. Totani, M. de Simone, M. Coreno, C. Grazioli, L. Lozzi, H. C. Herper, B. Sanyal, O. Eriksson, C. Puglia, and B. Brena, J. Phys. Chem. A **118**, 927 (2014)

[Caru05] A. N. Caruso, D. L. Schulz, and P. A. Dowben, Chem. Phys. Lett. **413**, 321 (2005)

[Chau13] D. Chaudhuri, E. Sigmund, A. Meyer, L. Röck, P. Klemm, S. Lautenschlager, A. Schmid, S. R. Yost, T. Van Voorhis, S. Bange, S. Höger, and J. M. Lupton, Angew. Chem. Int. Ed. **52**, 13449 (2013)

[Choy08] W. C. H. Choy and H. H. Fong, J. Phys. D: Appl. Phys. **41**, 155109 (2008)

[Cinc09] M. Cinchetti, K. Heimer, J.-P. Wüstenberg, O. Andreyev, M. Bauer, S. Lach, C. Ziegler, Y. Gao, and M. Aeschlimann, Nature Mater. **8**, 115 (2009)

[Cook09] P. L. Cook, X. Liu, W. Yang, and F. J. Himpsel, J. Chem. Phys. **131**, 194701 (2009)

[Crac05] M. F. Craciun, S. Rogge, and A. F. Mopurgo, J. Am. Chem. Soc. **127**, 12210 (2005)

[Crac06] M. F. Craciun, S. Rogge, M.-J. L. den Boer, S. Margadonna, K. Prassides, Y. Iwasa, and A. F. Morpurgo, Adv. Mater. **18**, 320 (2006)

[Dedi08] V. Dediu, L. E. Hueso, I. Bergenti, A. Riminucci, F. Borgatti, P. Graziosi, C. Newby, F. Casoli, M. P. De Jong, C. Taliani, and Y. Zhan, Phys. Rev. B **78**, 115203 (2008)

[Dien10] T. Dienel, A. Krause, R. Alle, R. Forker, K. Meerholz, and T. Fritz, Adv. Mater. **22**, 4064 (2010)

[Ding05] H. Ding and Y. Gao, Appl. Phys. Lett. **86**, 213508 (2005)

[Ding08] H. Ding, K. Park, K. Green, and Y. Gao, Chem. Phys. Lett. **454**, 229 (2008)

[Ding09] H. Ding, K. Park, and Y. Gao, J. Electron Spectrosc. Relat. Phenom. **174**, 45 (2009)

[Ding10] H. Ding and Y. Gao, Org. Electron. **11**, 1786 (2010)

[Djeg13] F. Djeghloul, F. Ibrahim, M. Cantoni, M. Bowen, L. Joly, S. Boukari, P. Ohresser, F. Bertran, P. Le Fevre, P. Thakur, F. Scheurer, T. Miyamachi,

R. Mattana, P. Seneor, A. Jaafar, C. Rinaldi, S. Javaid, J. Arabski, J.-P Kappler, W. Wulfhekel, N. B. Brookes, R. Bertacco, A. Taleb-Ibrahimi, M. Alouani, E. Beaurepaire, and W. Weber, Scientific Reports **3**, 1272 (2013)

[Elvi59] J. A. Elvidge and A. B. P. Lever, Proc. Chem. Soc., London, 195 (1959)

[Evan09] F. Evangelista, A. Ruocco, R. Gotter, A. Cossaro, L. Floreano, A. Morgante, F. Crispoldi, M. G. Betti, and C. Mariani, J. Chem. Phys. **131**,174710 (2009)

[Feng01] J. Feng, F. Li, W. Gao, S. Liu, Y. Liu, and Y. Wang, Appl. Phys. Lett. **78**, 3947 (2001)

[Flat07] K. Flatz, M. Grobosch, and M. Knupfer, J. Chem. Phys. **126**, 214702 (2007)

[Flor09] F. Flores, J. Ortega, and H. Vazquez, Phys. Chem. Chem. Phys. **11**, 8658 (2009)

[Forr04] S. R. Forrest, Nature **428**, 911 (2004)

[Frie12] R. Friedrich, T. Hahn, J. Kortus, M. Fronk, F. Haidu, G. Salvan, D. R. T. Zahn, M. Schlesinger, M. Mehring, F. Roth, B. Mahns, and M. Knupfer, J. Chem. Phys. **136**, 064704 (2012)

[Fu07] Y.-S. Fu, S.-H. Ji, X. Chen, X.-C. Ma, R. Wu, C.-C. Wang, W.-H. Duan, X.-H. Qui, B. Sun, P. Zhang, J.-F. Jia, and Q.-K. Xue, Phys. Rev. Lett. **99**, 256601 (2007)

[Fugg92] J. C. Fuggle and J. E. Inglesfield (eds.), Unoccupied Electronic States, Topics in Applied Physics 69, Springer, Berlin Heidelberg (1992)

[Fuji07] H. Fujiwara, Spectroscopic Ellipsometry: Principles and Applications, Wiley, Tokyo (2007)

[Fung04] M. K. Fung, S. L. Lai, S. W. Tong, S. N. Bao, C. S. Lee, S. T. Lee, Chem. Phys. Lett. **392**, 40 (2004)

[Gao02] W. Gao and A. Kahn, Org. Electron. **3**, 53 (2002)

[Gao03A] W. Gao and A. Kahn, J. Appl. Phys. **94**, 359 (2003)

[Gao03B] Y. Gao and L. Yan, Chem. Phys. Lett. **380**, 451 (2003)

[Gao10] Y. Gao, Mater. Sci. Eng. R **68**, 39 (2010)

[Garg10] P. Gargiani, A. Calabrese, C. Mariani, and M. G. Betti, J. Phys. Chem. C **114**, 12258 (2010)

[Garv94] L. A. J. Garvie and A. J. Craven, Phys. Chem. Minerals **21**, 191 (1994)

[Gavr04] G. N. Gavrila, H. Mendez, T. U. Kampen, D. R. T. Zahn, D. V. Vyalikh, and W. Braun, Appl. Phys. Lett. **85**, 4657 (2004)

[Ge09] Y. Ge, T. Weidner, H. Ahn, J. E. Whitten, and M. Zharnikov, J. Phys. Chem. C **113**, 4575 (2009)

[Gebe02] D. Gebeyehu, C. J. Brabec, N. S. Sariciftci, D. Vangeneugden, R. Kiebooms, D. Vanderzande, F. Kienberger, H. Schindler, Synth. Met. **125**, 279 (2002)

[Gilb03] B. Gilbert, B. H. Frazer, A. Belz, P. G. Conrad, K. H. Nealson, D. Haskel, J. C. Lang, G. Srajer, and G. De Stasio, J. Phys. Chem. A **107**, 2839 (2003)

[Giov07] L. Giovanelli, P. Vilmercati, C. Castellarin-Cudia, J.-M. Themlin, L. Porte, and A. Goldoni, J. Chem. Phys. **126**, 044709 (2007)

[Gord04] O. D. Gordan, M. Friedrich, and D. R. T. Zahn, Org. Electron. **5**, 291 (2004)

[Gord06] O. D. Gordan, C. Himcinschi, C. Cobet, N. Esser, W. Braun, and D. R. T. Zahn, Appl. Phys. Lett. **88**, 141913 (2006)

[Gorg04] M. Gorgoi, W. Michaelis, T. U. Kampen, D. Schlettwein, D. R. T. Zahn, Appl. Surf. Sci. **234**, 138 (2004)

[Gorg05] M. Gorgoi and D. R. T. Zahn, Org. Electron. **6**, 168 (2005)

[Gorg06] M. Gorgoi and D. R. T. Zahn, Appl. Surf. Sci. **252**, 5453 (2006)

[Grob09] M. Grobosch, V. Yu. Aristov, O. V. Molodtsova, C. Schmidt, B. P. Doyle, S. Nannarone, and M. Knupfer, J. Phys. Chem. C **113**, 13219 (2009)

[Grob10] M. Grobosch, C. Schmidt, R. Kraus, and M. Knupfer, Org. Electron. **11**, 1483 (2010)

[Grob11] M. Grobosch, B.Mahns, C. Loose, R. Friedrich, C. Schmidt, J. Kortus, and M. Knupfer, Chem. Phys. Lett. **505**, 122 (2011)

[Güns11] A. Günsel, M. Kandaz, F. Yakuphanoglu, and W. A. Farooq, Synth. Met. **161**, 1477 (2011)

[Haid12] F. Haidu, O. D. Gordan, and D. R. T. Zahn, Thin Solid Films **520**, 4410 (2012)

[Haid13A] F. Haidu, A. Fechner, G. Salvan, O. D. Gordan, M. Fronk, D. Lehmann, B. Mahns, M. Knupfer, and D. R. T. Zahn, AIP Advances **3**, 062124 (2013)

[Haid14] F. Haidu, M. Ludemann, P. Schäfer, O. D. Gordan, and D. R. T. Zahn, Thin Solid Films **571**, 426 (2014)

[Häbe01] P. Häberle, W. Ibanez, R. Esparza, and P. Vargas, Phys. Rev. B **63**, 235412 (2001)

[Hess03] R. Hesse, T. Chasse, and R. Szargan, Anal. Bioanal. Chem. **375**, 856 (2003)

[Hess07] R. Hesse, P. Streubel, and R. Szargan, Surf. Interface Anal. **39**, 381 (2007)

[Heut07] S. Heutz, C. Mitra, W. Wu, A. J. Fisher, A. Kerridge, M. Stoneham, T. H. Harker, J. Gardener, H.-H. Tseng, T. S. Jones, C. Renner, and G. Aeppli, Adv. Mater. **19**, 3618 (2007)

[Hill00A] I. G. Hill, A. Kahn, Z. G. Soos, and R. A. Pascal, Jr., Chem. Phys. Lett. **327**, 181 (2000)

[Hill00B] I.G. Hill, A. Kahn, J. Cornil, D. A. dos Santos, and J. L. Bredas, Chem. Phys. Lett. **317**, 444 (2000)

[Himc05] C. Himcinschi, N. Meyer, S. Hartmann, M. Gersdorff, M. Friedrich, H.-H. Johannes, W. Kowalsky, M. Schwambera, G. Strauch, M. Heuken, and D. R. T. Zahn, Appl. Phys. A **80**, 551 (2005)

[Hutc92] D. C. Hutchings, M. Sheik-Bahae, D. J. Hagan, and E. W. van Stryland, Optical and Quantum Electronics **24**, 1 (1992)

[Hüfn03] S. Hüfner, Photoelectron Spectroscopy: Principles and Applications, Springer, Berlin Heidelberg (2003)

[Hwan09] J. Hwang, A. Wan, A. Kahn, Mater. Sci. Eng. R **64**, 1 (2009)

[Ishi99] H. Ishii, K. Sugiyama, E. Ito, and K. Seki, Adv. Mater. **11**, 605 (1999)

[Ishi10] N. Ishikawa, Struct. Bond. **135**, 211 (2010)

[Java10] S. Javaid, M. Bowen, S. Boukari, L. Joly, J.-B. Beaufrand, Xi Chen, Y. J. Dappe, F. Scheurer, J.-P. Kappler, J. Arabski, W. Wulfhekel, M. Alouani, and E. Beaurepaire, Phys. Rev. Lett. **105**, 077201 (2010)

[Joha99] N. Johansson, T. Osada, S. Stafström, W. R. Salaneck, V. Parente, D. A. dos Santos, X. Crispin, and J. L. Bredas, J. Chem. Phys. **111**, 2157 (1999)

[Johs08] B. Johs and J. S. Hale, Phys. Stat. Sol. A **205**, 715 (2008)

[Kata10] T. Kataoka, Y. Yamazaki, Y. Sakamoto, A. Fujimori, F.-H. Chang, H.-J. Lin, D. J. Huang, C. T. Chen, A. Tanaka, S. K. Mandal, T. K. Nath, D. Karmakar, and I. Dasgupta, Appl. Phys. Lett. **96**, 252502 (2010)

[Kato12] K. Katoh, H. Isshiki, T. Komeda, and M. Yamashita, Chem. Asian J. **7**, 1154 (2012)

[Kim12] K. Kim, K. Hong, S. Kim, and J.-L. Lee, J. Phys. Chem. C **116**, 9158 (2012)

[Knup01] M. Knupfer, H. Peisert, and T. Schwieger, Phys. Rev. B **65**, 033204 (2001)

[Knup05] M. Knupfer and G. Paasch, J. Vac. Sci. Technol. A **23**, 1072 (2005)

[Koch85] E. E. Koch, Y. Jugnet, and F. J. Himpsel, Chem. Phys. Lett. **116**, 7 (1985)

[Kosh00] M. Koshino, H. Kurata, S. Isoda, T. Kobayashi, Micron **31**, 373 (2000)

[Kozl12] M. Kozlik, S. Paulke, M. Gruenewald, R. Forker, and T. Fritz, Org. Electron. **13**, 3291 (2012)

[Kram27] H. A. Kramers, Atti Congr. Int. Fis. Como **2**, 545 (1927)

[Krau09] R. Kraus, M. Grobosch, and M. Knupfer, Chem. Phys. Lett. **469**, 121 (2009)

[Krau10] S. Krause, M. B. Casu, A. Schöll, and E. Umbach, New J. Phys. **10**, 085001 (2008)

[Krol12] T. Kroll, R. Kraus, R. Schönfelder, V. Yu. Aristov, O. V. Molodtsova, P. Hoffmann, and M. Knupfer, J. Chem. Phys. **137**, 054306 (2012)

[Krön26] R. de L. Krönig, J. Opt. Soc. Am. Rev. Scient. Instrum. **12**, 547 (1926)

[Krul13] C. Krull, R. Robles, A. Mugarza, and P. Gambardella, Nature Mat. **12**, 337 (2013)

[Lach12] S. Lach, A. Altenhof, K. Tarafder, F. Schmitt, Md. E. Ali, M. Vogel, J. Sauther, P. M. Oppeneer, and C. Ziegler, Adv. Funct. Mater. **22**, 989 (2012)

[Lee12] H. Lee, S. W. Cho, J. Lee, P. E. Jeon, K. Jeong, J. W. Lee, and Y. Yi, J. Appl. Phys. **111**, 043712 (2012)

[Leve81] A. B. P. Lever, J. P. Wilshire, and S. K. Quan, Inorg. Chem. **20**, 761 (1981)

[Liao05] M.-S. Liao, J. D. Watts, and M.-J. Huang, Inorg. Chem. **44**, 1941 (2005)

[Lind12] S. Lindner, M. Knupfer, R. Friedrich, T. Hahn, and J. Kortus, Phys. Rev. Lett. **109**, 027601 (2012)

[Lind13] S. Lindner, B. Mahns, A. König, F. Roth, M. Knupfer, R. Friedrich, T. Hahn, and J. Kortus, J. Chem. Phys. **138**, 024707 (2013)

[Lu03] B. Lu, H. J. Zhang, H. Y. Li, S. N. Bao, P. He, and T. L. Hao, Phys. Rev. B **68**, 125410 (2003)

[Lüss13] B. Lüssem, M. L. Tietze, H. Kleemann, C. Hoßbach, J. W. Bartha, A. Zakhidov, and K. Leo, Nature Communications **4**:2775, 1 (2013)

[Lüth10] H. Lüth, Solid Surfaces, Interfaces and Thin Films, Springer, Berlin Heidelberg (2010)

[Mago97] S. N. Magonov, V. Elings, and M.-H. Whangbo, Surf. Sci. **375**, L385 (1997)

[Mahn11] B. Mahns, F. Roth, M. Grobosch, D. R. T. Zahn, and M. Knupfer, J. Chem. Phys. **134**, 194504 (2011)

[Mich77] H. B. Michaelson, J. Appl. Phys. **48**, 4729 (1977)

[Mitr03] C. Mitra, Z. Hu, P. Raychaudhuri, S. Wirth, S. I. Csiszar, H. H. Hsieh, H.-J. Lin, C. T. Chen, and L. H. Tjeng, Phys. Rev. B **67**, 092404 (2003)

[Molo05] O. V. Molodtsova, V. M. Zhilin, D. V. Vyalikh, V. Yu. Aristov, and M. Knupfer, J. Appl. Phys. **98**, 093702 (2005)

[Molo08A] O. V. Molodtsova, M. Knupfer, V. Yu. Aristov, D. V. Vyalikh, V. M. Zhilin, and Yu. A. Ossipyan, J. Appl. Phys. **103**, 053711 (2008)

[Molo08B] O. V. Molodtsova, M. Knupfer, V. V. Maslyuk, D. V. Vyalikh, V. M. Zhilin, Y. A. Ossipyan, T. Bredow, I. Mertig, and V. Yu. Aristov, J. Chem. Phys. **129**, 154705 (2008)

[Mori97] K. Morishige, S. Tomoyasu, and G. Iwano, Langmuir **13**, 5184 (1997)

[Neat06] J. B. Neaton, M. S. Hybersten, and S. G. Louie, Phys. Rev. Lett. **97**, 216405 (2006)

[Nesb98] H. W. Nesbitt and D. Banerjee, Am. Mineral. **83**, 305 (1998)

[Nils12] K. Nilson, J. Åhlund, M.-N. Shariati, J. Schiessling, P. Palmgren, B. Brena, E. Göthelid, F. Hennies, Y. Huismans, F. Evangelista, P. Rudolf, M. Göthelid, N. Mårtensson, and C. Puglia, J. Chem. Phys. **137**, 044708 (2012)

[Nguy10] T. Q. Nguyen, M. C. S. Escano, and H. Kasai, J. Phys. Chem. B **114**, 10017 (2010)

[Okud99] K. K. Okudaira, S. Hasegawa, H. Ishii, K. Seki, Y. Harada, and N. Ueno, J. Appl. Phys. **85**, 6453 (1999)

[Peis02] H. Peisert, M. Knupfer, T. Schwieger, J. M. Auerhammer, M. S. Golden, and J. Fink, J. Appl. Phys. **91**, 4872 (2002)

[Petr11] F. Petraki, H. Peisert, F. Latteyer, U. Aygül, A. Vollmer, and T. Chasse, J. Phys. Chem. C **115**, 21334 (2011)

[Petr12] F. Petraki, H. Peisert, P. Hoffmann, J. Uihlein, M. Knupfer, and T. Chasse, J. Phys. Chem. C **116**, 5121 (2012)

[Pi04] T.-W. Pi, C.-P. Ouyang, T. C. Yu, J.-F. Wen, and H. L. Hsu, Phys. Rev. B **70**, 235346 (2004)

[Popi06] M. Popinciuc, H. T. Jonkman, and B. J. van Wees, J. Appl. Phys. **100**, 093714 (2006)

[Prig06] V. N. Prigodin, J. D. Bergeson, D. M. Lincoln, A. J. Epstein, Synth. Met. **156**, 757 (2006)

[Rapp92] A. K. Rappe, C. J. Casewit, K. S. Colwell, W. A. Goddard III, and W. M. Skiff, J. Am. Chem. Soc. **114**, 10024 (1992)

[Qi10] Y. Qi, T. Sajoto, M. Kröger, A. M. Kandabarow, W. Park, S. Barlow, E.-G. Kim, L. Wielunski, L. C. Feldman, R. A. Bartynski, J.-L. Bredas, S. R. Marder, and A. Kahn, Chem. Mater. **22**, 524 (2010)

[Raje01] K. R. Rajesh and C. S. Menon, Mater. Lett. **51**, 266 (2001)

[Raje05] K. R. Rajesh and C. S. Menon, Eur. Phys. J. B **47**, 171 (2005)

[RGBL] http://www.bessy.de/rglab/index.html (19.02.2014)

[Rocc90] M. L. M. Rocco, K.-H. Frank, P. Yannoulis, and E.-E. Koch, J. Chem. Phys. **93**, 6859 (1990)

[Rocc08] M. L. M. Rocco, M. Haeming, D. R. Batchelor, R. Fink, A. Schöll, and E. Umbach, J. Chem. Phys. **129**, 074702 (2008)

[Roth08] F. Roth, A. König, R. Kraus, and M. Knupfer, J. Chem. Phys. **128**, 194711 (2008)

[Ruoc08] A. Ruocco, F. Evangelista, R. Gotter, A. Attili, and G. Stefani, J. Phys. Chem. C **112**, 2016 (2008)

[Saku02] Y. Sakurai, G. Salvan, Y. Hosoi, H. Ishii, Y. Ouchi, K. Seki, T. U. Kampen, D. R. T. Zahn, Appl. Surf. Sci. **190**, 382 (2002)

[Saku04] Y. Sakurai, Y. Hosoi, H. Ishii, Y. Ouchi, G. Salvan, A. Kobitski, T. U. Kampen, D. R. T. Zahn, and K. Seki, J. Appl. Phys. **96**, 5534 (2004)

[Sant07] T. S. Santos, J. S. Lee, P. Migdal, I. C. Lekshmi, B. Satpati, and J. S. Moodera, Phys. Rev. Lett. **98**, 016601 (2007)

[Schm11] F. Schmitt, J. Sauther, S. Lach, and C. Ziegler, Anal. Bioanal. Chem. **400**, 665 (2011)

[Schm13] G. C. Schmidt, D. Höft, M. Bhuie, K. Haase, M. Bellmann, F. Haidu, D. Lehmann, D. R. T. Zahn, and A. C. Hübler, Appl. Phys. Lett. **103**, 113302 (2013)

[Schö03] A. Schöll, Y. Zou, Th. Schmidt, R. Fink, and E. Umbach, J. Electron. Spectrosc. Relat. Phenom. **129**, 1 (2003)

[Schw02] T. Schwieger, H. Peisert, M. S. Golden, M. Knupfer, and J. Fink, Phys. Rev. B **66**, 155207 (2002)

[Schw03] T. Schwieger, M. Knupfer, W. Gao, and A. Kahn, Appl. Phys. Lett. **83**, 500 (2003)

[Schw04] T. Schwieger, H. Peisert, and M. Knupfer, Chem. Phys. Lett. **384**, 197 (2004)

[Scot03] J. C. Scott, J. Vac. Sci. Technol. A **21**, 521 (2003)

[Shen10A] X. Shen, L. Sun, E. Benassi, Z. Shen, X. Zhao, S. Sanvito, and S. Hou, J. Chem. Phys. **132**, 054703 (2010)

[Shen10B] X. Shen, L. Sun, Z. Yi, E. Benassi, R. Zhang, Z. Shen, S. Sanvito, and S. Hou, Phys. Chem. Chem. Phys. **12**, 10805 (2010)

[Shir72] D. A. Shirley, Phys. Rev. B **5**, 4709 (1972)

[Simo13] K. A. Simonov, A. S. Vinogradov, M. M. Brzhezinskaya, A. B. Preobrajenski, A. V. Generalov, A. Yu. Klyushin, Appl. Surf. Sci. **267**, 132 (2013)

[Smit88] N. V. Smith, Rep. Prog. Phys. **51**, 1227 (1988)

[Smit01] D. Y. Smith, M. Inokuti, and W. Karstens, J. Phys.: Condens. Matter **13**, 3883 (2001)

[Stei11] S. Steil, K. Goedel, A. Ruffing, I. Sarkar, M. Cinchetti, M. Aeschlimann, Synth. Met. **161**, 570 (2011)

[Step14] S. Stepanow, A. L. Rizzini, C. Krull, J. Kavich, J. C. Cezar, F. Yakhou-Harris, P. M. Sheverdyaeva, P. Moras, C. Carbone, G. Ceballos, A. Mugarza, and P. Gambardella, J. Am. Chem. Soc. **136**, 5451 (2014)

[Stöh96] J. Stöhr, NEXAFS Spectroscopy, Springer Series in Surface Science 25, Springer, Berlin Heidelberg (1996)

[Stro12] A. Strozecka, M. Soriano, J. I. Pascual, and J. J. Palacios, Phys. Rev. Lett. **109**, 147202 (2012)

[Sun07] Y. Sun and J. A. Rogers, Adv. Mater. **19**, 1897 (2007)

[Tagu06] Y. Taguchi, T. Miyake, S. Margadonna, K. Kato, K. Prassides, and Y. Iwasa, J. Am. Chem. Soc. **128**, 3313 (2006)

[Tagu10] D. Taguchi, S. Inoue, L. Zhang, J. Li, M. Weis, T. Manaka, and M. Iwamoto, J. Phys. Chem. Lett. **1**, 803 (2010)

[Tang87] C. W. Tang and S. A. VanSlyke, Appl. Phys. Lett. **51**, 913 (1987)

[Thol88] B. T. Thole, G. van der Laan, and P. H. Butler, Chem. Phys. Lett. **149**, 295 (1988)

[Toad09] T. Toader, G. Gavrila, W. Braun, J. Ivanco, and D. R. T. Zahn, Phys. Status Solidi B **246**, 1510 (2009)

[Tomp05] H. G. Tompkins and E. A. Irene (eds.), Handbook of Ellipsometry, William Andrew, New York (2005)

[Tsip02] E. V. Tsiper, Z. G. Soos, W. Gao, and A. Kahn, Chem. Phys. Lett. **360**, 47 (2002)

[UNIF] http://unifit-software.de/ (19.02.2014)

[vdBr07] J. van den Brink and A. F. Mopurgo, Nature **450**, 177 (2007)

[vdLa88] G. van der Laan and B. T. Thole, Phys. Rev. Lett. **60**, 1977 (1988)

[vFaa03] E. van Faassen and H. Kerp, Sens. Actuators B **88**, 329 (2003)

[Watt06] B. Watts, L. Thomsen, and P. C. Dastoor, J. Electron. Spectrosc. Relat. Phenom. **151**, 105 (2006)

[Wool10] J. A. Woollam Co., Inc., Guide to Using WVASE32, Lincoln (2010)

[Würt11] F. Würthner, T. E. Kaiser, and C. R. Saha-Möller, Angew. Chem. Int. Ed. **50**, 3376 (2011)

[Yana09] S.-I. Yanagiya, J. Morimoto, N. Goto, and A. S. Helmy, Proc. of SPIE **7413**, 74130O (2009)

[Yeh85] J. J. Yeh and I. Lindau, Atom. Data Nucl. Data **32**, 1 (1985)

[Yosh01] H. Yoshida, K. Tsutsumi, and N. Sato, J. Electron Spectrosc. Relat. Phenom. **121**, 83 (2001)

[Zahn06] D. R. T. Zahn, G. N. Gavrila, and M. Gorgoi, Chem. Phys. **325**, 99 (2006)

[Zhao05] F. Zhao, F. Harnisch, U. Schröder, F. Scholz, P. Bogdanoff, and I. Herrmann, Electrochem. Commun. **7**, 1405 (2005)

[Zuti04] I. Zutic, J. Fabian, and S. Das Sarma, Rev. Mod. Phys. **76**, 323 (2004)

List of Figures

List of Tables

Erklärung

- 125 -

Ich erkläre, dass ich die vorliegende Arbeit selbständig und nur unter Verwendung der angegebenen Literatur und Hilfsmittel angefertigt habe.

Januar 2015

M. Sc. Francisc Haidu

Curriculum Vitae

Francisc Haidu

Date of birth   01 January 1986
Place of birth   Baia Mare, Romania
Nationality   Romanian, Hungarian
Gender   Male
Family status   Married
Foreign languages   English, German, French

Education

2013-2015   Research Associate at Semiconductor Physics Department,
Technische Universität Chemnitz, Germany

2010-2013   PhD studies at Semiconductor Physics Department,
Technische Universität Chemnitz, Germany
Subject: Photoemission and Ellipsometry studies on organic molecules
"Tailoring the Electronic and Optical Properties of Molecular Thin Films by Reducing and Oxidising Agents"

2008-2010   Master studies at "Babeş-Bolyai" University, Cluj-Napoca, Romania, in collaboration with Technische Universität Chemnitz, Germany
Subjects: Solid State Physics, Ellipsometry
Award: *Master Diploma* (mark 10 of 10)
"Ellipsometric Measurements of Thin Metallic Films"

2005-2008   Batchelor studies at "Babeş-Bolyai" University, Cluj-Napoca, Romania
Subject: Physics
Award: *Batchelor Diploma* (mark 9.83 of 10)
"Physical Methods in Thin Film Deposition"

2001-2005   "Gheorghe Şincai" National College, Baia Mare, Romania
Subjects: Mathematics – Informatics
Award: *High-school Diploma* (mark 9.60 of 10)

List of Publications

<ins>Parts of this work are already published:</ins>

15. <ins>F. Haidu</ins>, L. Smykalla, G. Salvan, M. Hietschold, M. Knupfer, and D. R. T. Zahn, *"Transport band gap opening at metal–organic interfaces"*, J. Vac. Sci. Technol. A **32**, 040602 (2014)

14. <ins>F. Haidu</ins>, M. Ludemann, P. Schäfer, O. D. Gordan, and D. R. T. Zahn, *"In Situ Ellipsometry – A Powerful Tool for Monitoring Alkali Doping of Organic Thin Films"*, Thin Solid Films **571**, 426 (2014)

13. <ins>F. Haidu</ins>, A. Fechner, G. Salvan, O. D. Gordan, M. Fronk, D. Lehmann, B. Mahns, M. Knupfer, and D. R. T. Zahn, *"Influence of film thickness and air exposure on the transport gap of manganese phthalocyanine"*, AIP Advances **3**, 062124 (2013)

12. R. Friedrich, T. Hahn, J. Kortus, M. Fronk, <ins>F. Haidu</ins>, G. Salvan, D. R. T. Zahn, M. Schlesinger, M. Mehring, F. Roth, B. Mahns, and M. Knupfer, *"Electronic states and the influence of oxygen addition on the optical absorption behaviour of manganese phthalocyanine"*, J. Chem. Phys. **136**, 064704 (2012)

<ins>Further publications:</ins>

11. G. C. Schmidt, D. Höft, K. Haase, A. C. Hübler, E. Karpov, R. Tkachov, M. Stamm, A. Kiriy, <ins>F. Haidu</ins>, D. R. T. Zahn, H. Yan, and A. Facchetti, *"Naphtalenediimide-based donor–acceptor copolymer prepared by chain-growth catalyst-transfer polycondensation: evaluation of electron-transporting properties and application in printed polymer transistors"*, J. Mater. Chem. C **2**, 5149 (2014)

10. S. Lindner, B. Mahns, U. Treske, O. Vilkov, <ins>F. Haidu</ins>, M. Fronk, D. R. T. Zahn, and M. Knupfer, *"Epitaxial growth and electronic properties of well ordered phthalocyanine heterojunctions $MnPc/F_{16}CoPc$"*, J. Chem. Phys. **141**, 094706 (2014)

9. F. Lungwitz, C. Mende, M. Fronk, <ins>F. Haidu</ins>, H. Lang, G. Salvan, and D. R. T. Zahn, *"Optical and Magneto-Optical Characterisation of Thin Films of Functionalised Tetraphenylporphyrins"*, Thin Solid Films **571**, 377 (2014)

8. G. C. Schmidt, D. Höft, M. Bhuie, K. Haase, M. Bellmann, <ins>F. Haidu</ins>, D. Lehmann, D. R. T. Zahn, and A. C. Hübler, *"Modified poly(3,4-ethylene-dioxythiophene):poly(styrenesulfonate) source/drain electrodes for fully printed organic field-effect transistors consisting of a semiconductor blend"*, Appl. Phys. Lett. **103**, 113302 (2013)

7. A. G. Milekhin, N. A. Yeryukov, L. L. Sveshnikova, T. A. Duda, D. Yu. Protasov, A. K. Gutakovskii, S. A. Batsanov, N. V. Surovtsev, S. V. Adichtchev, C. Himcinschi, V. Dzhagan, F. Haidu, and D. R. T. Zahn, *"CdZnS quantum dots formed by the Langmuir–Blodgett technique"*, J. Vac. Sci. Technol. B **31**, 04D109-1 (2013)

6. I. Zunke, A. Heft, P. Schäfer, F. Haidu, D. Lehmann, B. Grünler, A. Schimanski, and D. R. T. Zahn, *"Conductive zinc oxide thin film coatings by combustion chemical vapour deposition at atmospheric pressure"*, Thin Solid Films **532**, 50 (2013)

5. S. Kaufmann, H. Schletter, D. Lehmann, F. Haidu, D. R. T. Zahn, M. Hietschold, and W. A. Goedel, *"Preparation of mesoscopic gold rings and split rings by selective wetting of the contact points between the spheres within colloidal crystals"*, J. Mater. Sci. **47**, 4530 (2012)

4. M. Fronk, C. Schubert, F. Haidu, C. Scarlat, K. Dörr, M. Albrecht, D. R. T. Zahn, and G. Salvan, *"Characterization of Organic Thin Films on Ferromagnetic Substrates by Spectroscopic Ellipsometry and Magneto-Optical Kerr Effect Spectroscopy"*, IEEE T. Magn. **48**, 2777 (2012)

3. F. Haidu, O. D. Gordan, and D. R. T. Zahn, *"In situ ellipsometric study of copper growth on silicon"*, Thin Solid Films **520**, 4410 (2012)

2. S. Mueller, T. Waechtler, L. Hofmann, A. Tuchscherer, R. Mothes, O. Gordan, D. Lehmann, F. Haidu, M. Ogiewa, L. Gerlich, S.-F. Ding, S. E. Schulz, T. Gessner, H. Lang, D. R.T. Zahn, and X.-P. Qu, *"Thermal ALD of Cu via Reduction of Cu_xO films for the Advanced Metallization in Spintronic and ULSI Interconnect Systems"*, IEEE - 2011 Semiconductor Conference Dresden, art. no. 6068736 (2011), DOI: 10.1109/SCD.2011.6068736

1. F. Haidu, M. Fronk, O. D. Gordan, C. Scarlat, G. Salvan, and D. R. T. Zahn, *"Dielectric function and magneto-optical Voigt constant of Cu_2O: A combined spectroscopic ellipsometry and polar magneto-optical Kerr spectroscopy study"*, Phys. Rev. B **84**, 195203 (2011)

Acknowledgements